CBP Tech Note 196
LCC-0033
November 1999.

RF cavity R&D at LBNL for the NLC Damping Rings, FY1999

R.A. Rimmer, J.N. Corlett, G. Koehler, D. Li,
N. Hartman, J. Rasson, T. Saleh.

LBNL, 1 Cyclotron Rd., Berkeley, CA 94720

Abstract

This report contains a summary of the R&D activities at LBNL on RF cavities for the NLC damping rings during fiscal year 1999. These activities include the optimization of the RF design for both efficiency and damping of higher-order modes (HOMs), by systematic study of the cavity profile, the effect of the beam pipe diameter, nosecone angle and gap, the cross section and position of the HOM damping waveguides and the coupler. The effect of the shape of the HOM waveguides and their intersection with the cavity wall on the local surface heating is also an important factor, since it determines the highest stresses in the cavity body. This was taken into account during the optimization so that the stresses could be reduced at the same time as the HOM damping was improved over previous designs. A new method of calculating the RF heating was employed, using a recently released high frequency electromagnetic element in ANSYS. This greatly facilitates the thermal and stress analysis of the design since a common mesh can be used throughout. The mechanical design and fabrication methods have been developed with the goals of lower stresses, fewer parts and simpler assembly compared to previous designs. This should result in substantial cost savings. Preliminary designs are described for the cavity ancillary components including the RF window, HOM loads, and tuners. A preliminary manufacturing plan is included, with an initial estimate of the resource requirements. Other cavity options are discussed which might be desirable to either lower the R/Q, for reduced transient response, or lower the residual HOM impedance to reduce coupled-bunch growth rates further still.

Contents

Introduction

In order to provide the required short bunch length and stable beam at high currents the cavities for the NLC damping rings must have strong HOM damping, a high gradient and heavy beam loading. Table 1 shows some parameters of the damping ring RF system. The total voltage of 1.5 MV and approximately 600 kW of beam power can be delivered by three copper cavities in each of the damping rings (2 MV, four cavities in the positron pre-damping ring). Superconducting cavity technology is not necessary to meet these requirements (although it might be advantageous for beam loading transients, see section 7). The PEP-II normal-conducting design has been used as the basis for the development of the proposed NLC cavity. The RF frequency of 714 MHz allows the possibility of a future luminosity upgrade by increasing the number of bunches, although the bunch rate is initially proposed to be 357 MHz. This choice keeps the power density and stresses in the NLC cavity high, comparable to the current PEP-II operating conditions (taking the scaled PEP-II design as the baseline). Means of reducing the stress without sacrificing the good HOM damping properties and accelerating mode efficiency have been investigated. Simplifications of the mechanical design and fabrication have also been considered.

The PEP-II RF cavity is among the first designs with strong damping of the higher order modes (HOMs), which are now seeing operation in the high-current e+ e- factories around the world [1, 2]. This design has already proven to be very successful in the reduction of coupled-bunch instability growth rates, contributing to the rapid commissioning of the rings and the early attainment of high luminosity. The technology developed for PEP-II has already been put to further use for the 1.5 GHz ALS third harmonic cavity upgrade [3], and is a natural candidate for future projects such as light sources, storage ring based colliders and linear collider damping rings [4]. Many lessons learned during the design, manufacture and commissioning of these cavities were applied to the new design. The availability of better analysis tools and faster computers also now allows more detailed study of some aspects of the design.

Table 1. Damping ring RF parameters.

Energy	1.98 GeV
Circumference	297m
RF Frequency	714 MHz
Harmonic Number	708
Bunch Spacing	2.8 ns
Beam Current	0.75 A
σ_ε	0.09 %
σ_z	4 mm
α	0.00066
$U_{s.r.}$	750 keV/turn
$U_{HOM's}$	5.6 keV/turn
$U_{parasitic}$	36 keV/turn
V_{RF}	1.5 MV
Number of Cavities	3
Number of Klystrons	1
Cavity Wall Dissipation	42 kW/cavity
Beam Power	593.7 kW
Klystron Power	1 MW
Shunt Impedance	3.0 MΩ/cavity
Unloaded Q	25500
Coupling Factor	5.8
Synchronous Phase Angle	32°
Optimum Detuning at Full Current	106 kHz
Synchrotron Frequency	6.9 kHz
Loaded Q	3777
Energy Acceptance	± 1.8 %

1. Calculation of RF properties and HOMs

One of the most difficult tasks in designing a strongly HOM damped RF cavity is to ensure that all longitudinal and transversely deflecting modes are adequately damped, up to and possibly above the beam pipe cutoff frequency. At the same time the efficiency of the accelerating mode must be kept as high as possible. The method used to optimize the HOM damping involves a simulation in the time domain wherein the structure is excited by a short bunch passing through it, either on axis (for the longitudinal modes) or off axis (for the deflecting modes), and the long range wakefield is computed and recorded for many meters behind the bunch. This time record contains the amplitude of excitation and exponential decay of all of the modes and a Fourier transform of this signal, normalized to the bunch spectrum, reveals the broad-band impedance spectrum of the cavity. The frequency resolution is determined by the length of the wakefield recorded, limited only by computer time and eventually by the onset of numerical instabilities in the simulation. Any mode still ringing with appreciable amplitude at the end of the recorded time will be truncated and artificially broadened in the spectrum, so care must be taken in interpreting the results.

In order to check the validity of these tools the PEP-II cavity geometry was modeled and the results compared with the known cavity properties [5]. There is very good agreement between the simulation and measurement in the distribution, structure and relative amplitudes of the modes. Figure 2.1 shows the calculated longitudinal impedance spectrum using this method for the PEP-II geometry, including coupler, compared with the values estimated from the measurements of the cold-test model. The close correlation of these results between the calculated and measured mode strengths gives confidence in the broadband simulation method as a useful tool for optimizing the overall geometry.

A scaled version of the PEP-II cavity was used as the baseline design for the NLC Zero-order Design Report (ZDR), [6]. For the present more detailed study the impact of various changes to the design were evaluated, with the goals of improving the HOM performance, thermal stresses and ease of manufacture. The options studied for the RF shape included a spherical mid section (the PEP-II body is toroidal), more compact "dumbbell" shaped ridged HOM waveguides, variation of the nosecone angle, HOM port placement and coupler shape and placement.

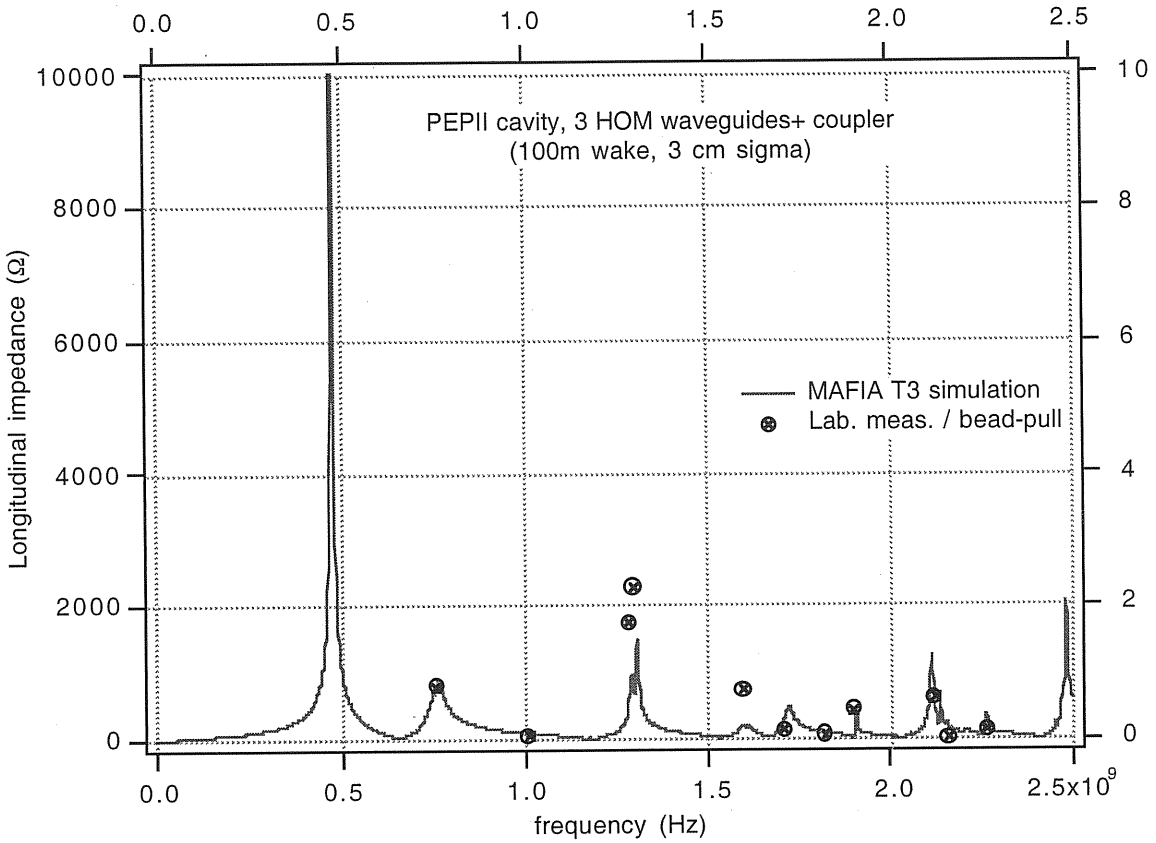

Figure 1. Calculated longitudinal impedance spectrum plus worst case estimate of modes measured in the first PEP-II cavity

1.1 Cavity profile

The PEP-II cavity has a toroidal profile with re-entrant nosecones, figure 2a. This is a very efficient shape with a high shunt impedance and a distribution of HOMs that can be adequately damped by three waveguides on the cavity wall, with a little help from the power coupler which is slightly offset from the cavity center for this reason. It may be advantageous for the center section of the cavity to have a spherical profile, figure 2b, since this greatly simplifies the geometry of any circular ports, which become figures of revolution and may be lathe turned instead of being cut with a milling machine. This may be accomplished without any significant loss in shunt impedance for the fundamental mode since the Q is higher, see table 2, and this compensates the reduction in R/Q. The distribution of HOM fields on the walls is different from the toroid however and the HOM damping scheme must be re-evaluated. The spherical shape was used on the ALS third harmonic cavities and they commissioned quickly with very little multipactoring.

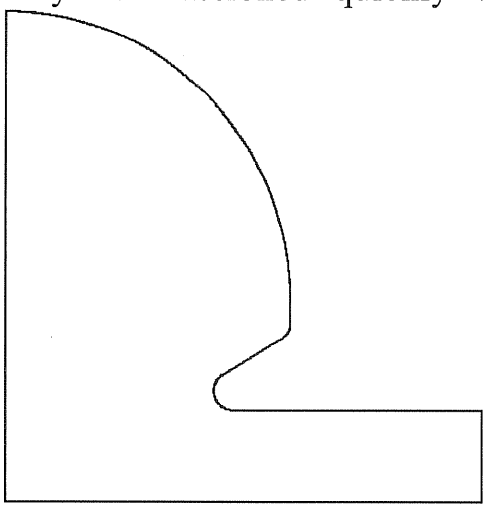

Figure 2a. PEP-II profile (toroid)

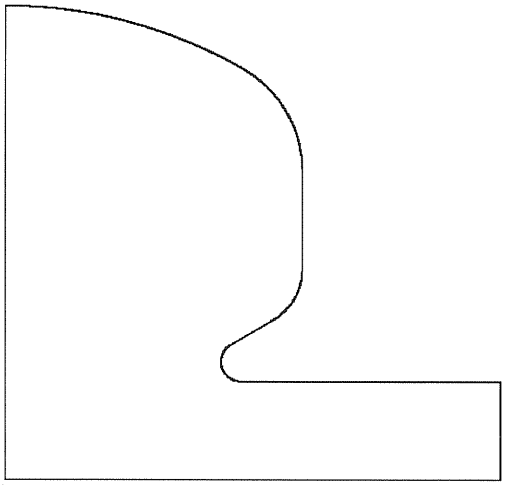

Figure 2b. Spherical mid section

Table 2. Parameters of toroid and hybrid cavity profiles.

Scaled PEP-II profile	**Spherical mid section**
f_o (2d)=714 MHz	f_o (2d)=714 MHz
R/Q (2D)=116.7	R/Q (2D)=118
Q_o (calc)=36984	Q_o (calc)=36182
Q_o (est)=25889 (70%)	Q_o (est)=25327 (70%)
R_s (calc)=4.32 MΩ	R_s (calc)=4.27 MΩ
R_s (est)=3.02 MΩ (70%)	R_s (est)=3.0 MΩ (70%)
V_{op}=500 kV	V_{op}=500 kV
P_{op}(est)=41.3 kW	P_{op} (est)=41.7 kW

1.2 Beam pipe diameter

For the ZDR the cavity beam pipe diameter was simply scaled along with the rest of the dimensions, resulting in a size that is considerably larger than elsewhere in the machine. The cavity shunt impedance could be improved if the bore were reduced, but at the penalty of stronger transverse short-range wakefields. If simple tapers are used upstream and downstream of each cavity however, the benefit of the larger bore is lost and the transverse loss parameter of the tapers may be comparable to that of the cavity itself. Alternatively if very smooth tapers are used and only at the far ends of the RF section, while the larger bore is maintained between cavities, then the total transverse loss parameter should be acceptable. Figure 4 shows the variation of shunt impedance and transverse loss parameter ($k\perp$) with beam pipe radius calculated with ABCI [7]. Also shown is the $k\perp$ for one scaled PEP cavity with two 10% tapers back to a bore of 15 mm (circle symbol - figure 3) two cavities with four tapers (diamond symbol - figure 5), and two cavities with only tapers at the ends (triangle symbol - figure 6). Note that the 31.8 mm bore cavity with two tapers has almost the same $k\perp$ as the 15 mm bore but only 82% of the shunt impedance. Note also that two cells with four tapers have about twice the loss parameter of the single cell with tapers, but that the case with tapers only at the ends is in between. We have chosen to keep the large bore between the cavities and taper only at the ends as a compromise between the shunt impedance and the transverse wakes.

In this case however there is a possibility of trapped modes between the cavities or between the end cavities and the tapers which may not be damped by the cavity loads. These would have to be damped by additional loads in or connected to the beam pipes. Simple 2D models have so far shown no strong modes trapped in this way but more work will be done to study this possibility and also to optimize the tapers to minimize the transverse loss parameter.

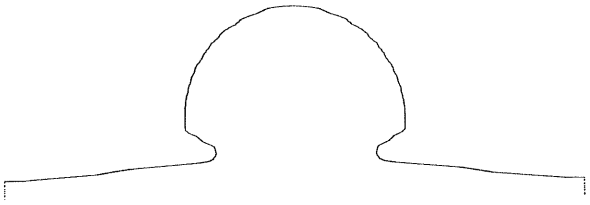

Figure 3. Cavity with tapers to 15 mm (2D geometry input to ABCI).

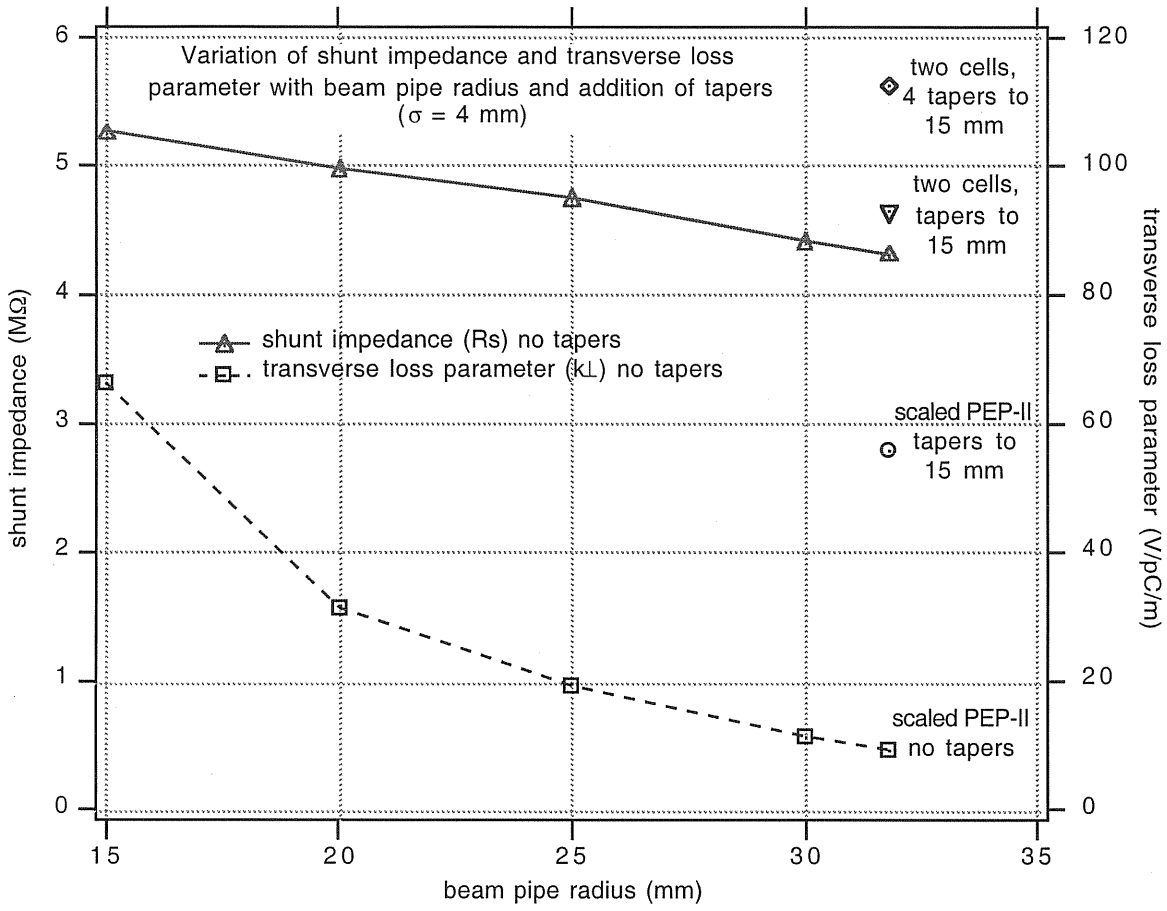

Figure 4. Variation of shunt impedance and transverse loss parameter with beam pipe radius.

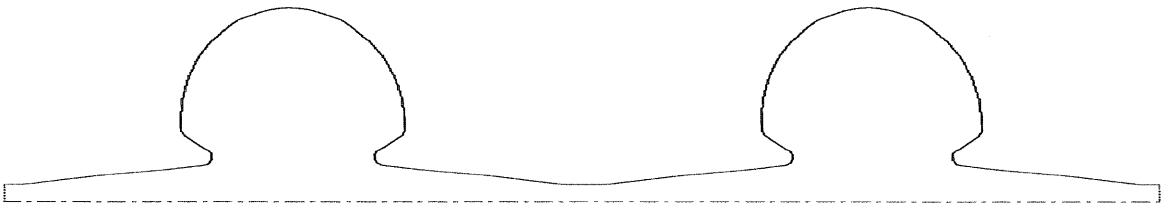

Figure 5. Two cavities with four tapers.

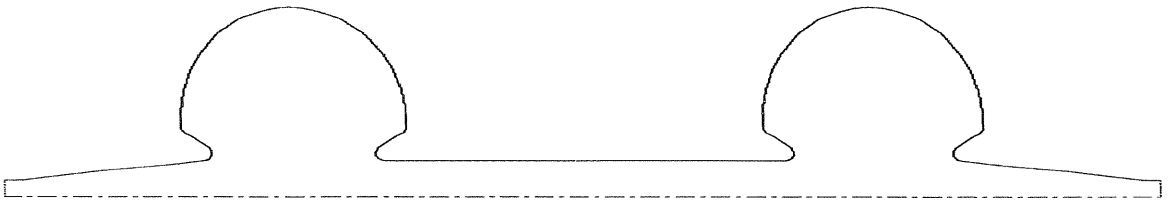

Figure 6. Two cavities with tapers only at ends.

1.3 Nosecone angle and tuning

The angle of the nosecone does not have a strong effect on the fundamental mode within the range of 20° to 45° with respect to the beam pipe. It may however result in a significant change in the HOM distribution. Figure 7 shows the variation in impedance of one longitudinal mode (OM2*) as a function of nosecone angle, calculated with MAFIA for the spherical mid-section cavity and dumbbell shaped HOM ports (see section 1.4). Figure 8 shows the variation of the peak amplitude of all the strong monopole modes below cutoff while figure 9 shows the same for dipole modes.

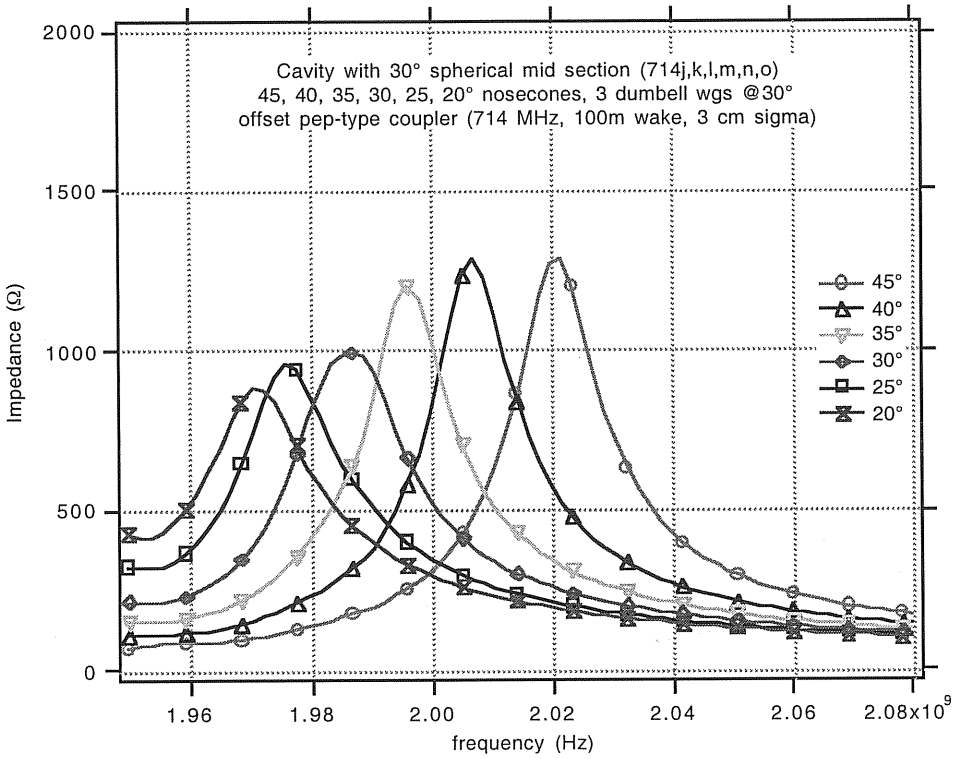

Figure 7. 0M2 mode impedance at various nosecone angles.

This analysis shows that the most favorable nosecone angle for the proposed waveguide damping scheme is around 30° (or less) for monopole modes while the highest remaining dipole mode is about the same for any angle between 20° and 45°, though the next strongest mode is lower at smaller angles. The nosecone angle for the proposed NLC cavity was chosen to be 30° (same as PEP-II).

---

* URMEL notation: 0/1=monopole/dipole, E/M=electric/magnetic boundary in center of cavity, last digit=mode number in order of frequency for each run

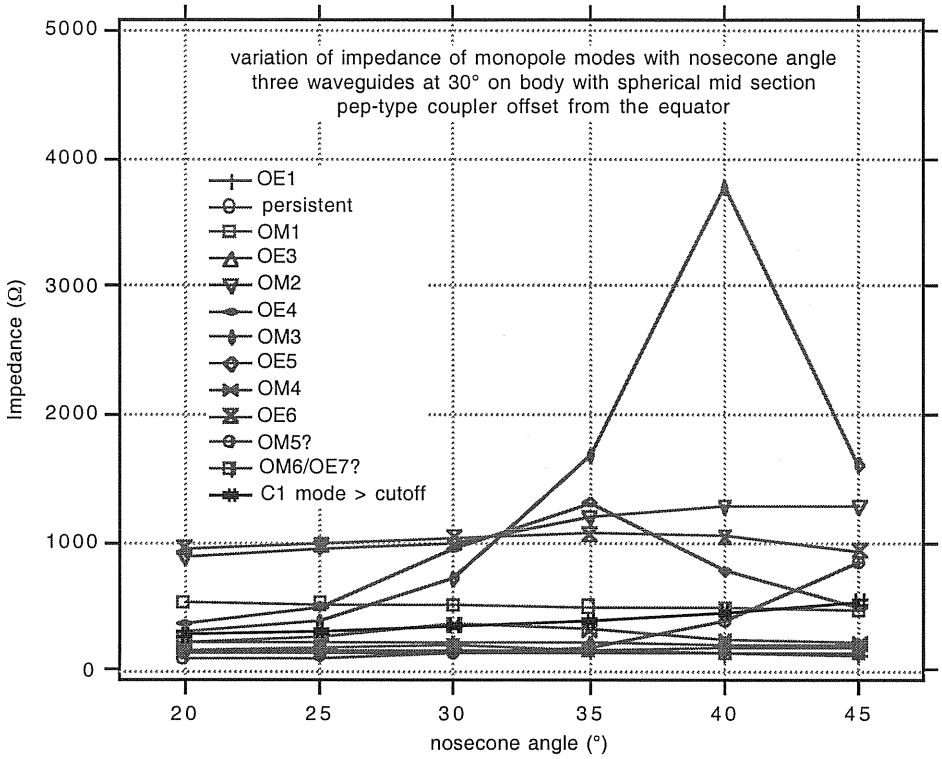

Figure 8. Variation of monopole mode strength with nosecone angle.

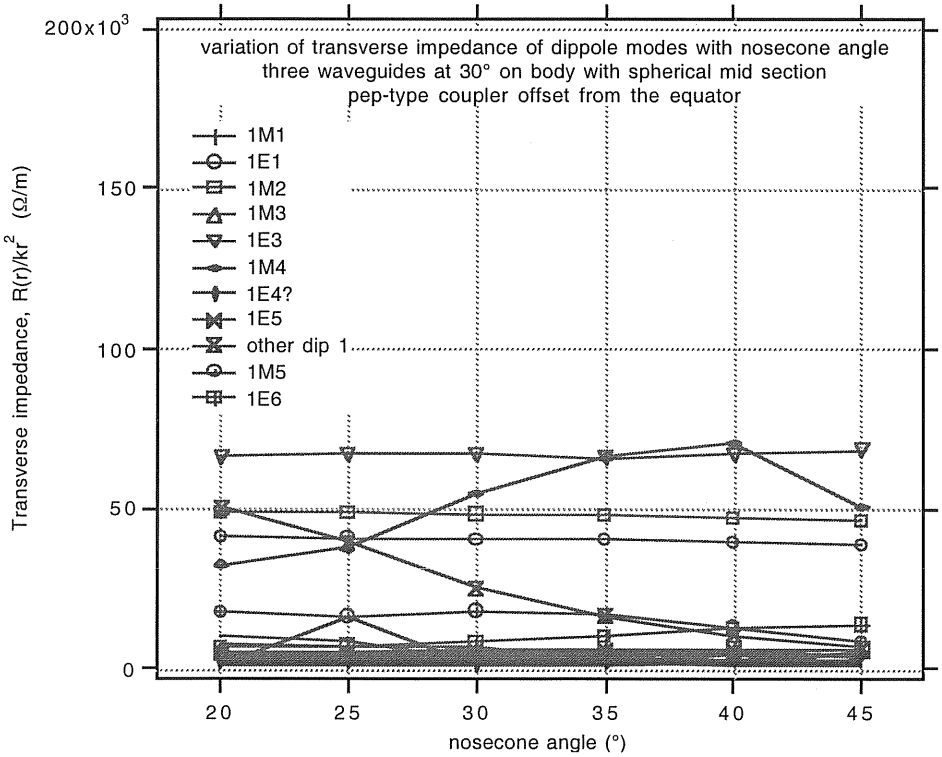

Figure 9. Variation of dipole mode strength with nosecone angle.

During manufacture the frequency of the cavity will be set by tuning the nosecones before final welding. Three simulations were run with the gap between the nosecones reduced 10 mm, nominal separation, and increased 10 mm (corresponding to 5 mm extra material on each nose, nominal dimensions, and 5 mm removed from each nose, far more than is likely to be required in practice). In each case the nosecone angle was kept at 30° and the nose tip radius was kept at 6.66 mm. Figure 10 shows the peaks in the spectrum from the broad-band simulation corresponding to the fundamental mode for three different gaps. Figure 11 shows the tuning sensitivity of the fundamental mode to changes in the gap.

To investigate the effects of small changes to the nosecone spacing on the HOM damping scheme the broadband spectra for the above cases were also examined. Figure 12 shows the variation of the longitudinal HOM strengths for the large changes of ± 5 mm on both noses. For small changes around the nominal gap the HOM spectra should not be significantly worsened. For comparison the range of tuning of the full gap during the PEP-II production run was approx. ± 0.008" (~±0.2 mm). If the gap is made much smaller then some of the trapped modes become significantly stronger and the HOM waveguide placement would need to be re-optimized. Interestingly if the gap is made significantly larger then some of the modes above cut-off begin to become troublesome. This case would also require re-optimization. Figure 13 shows the effect on the dipole modes; there is no significant change for small changes in the gap.

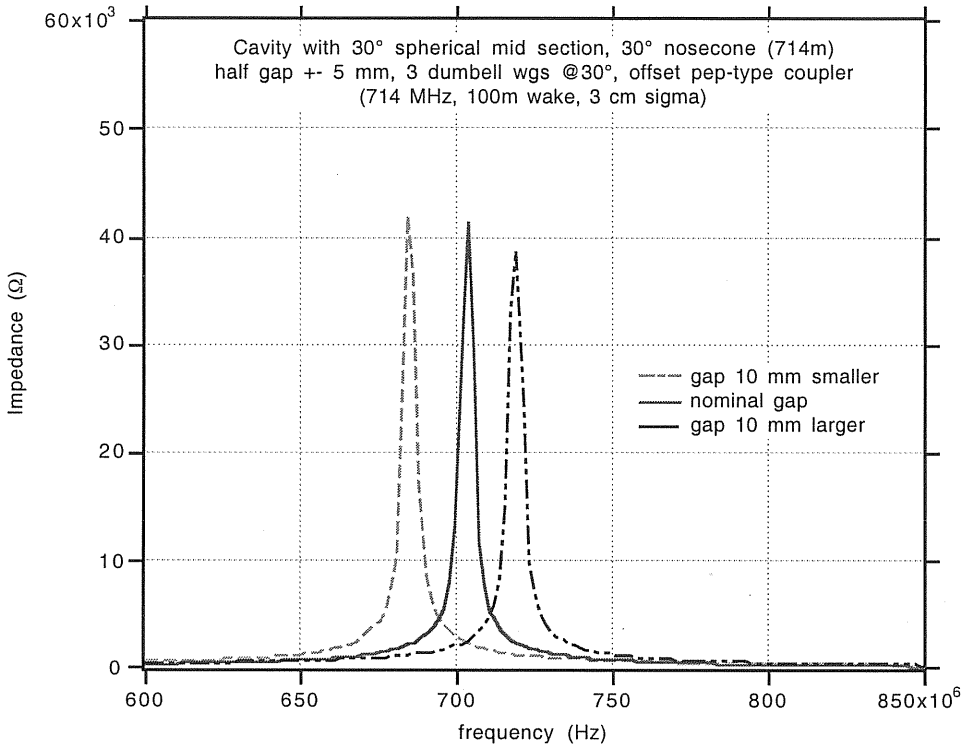

Figure 10. Frequency tuning by adjusting gap between noses.

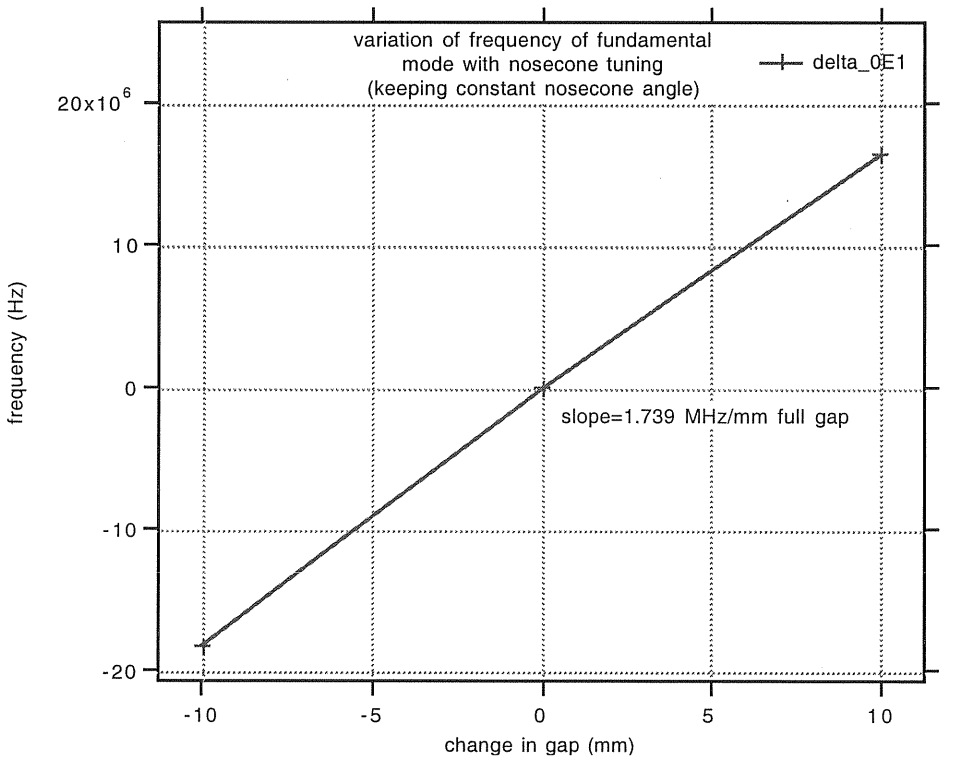

Figure 11. Frequency tuning sensitivity for the fundamental mode.

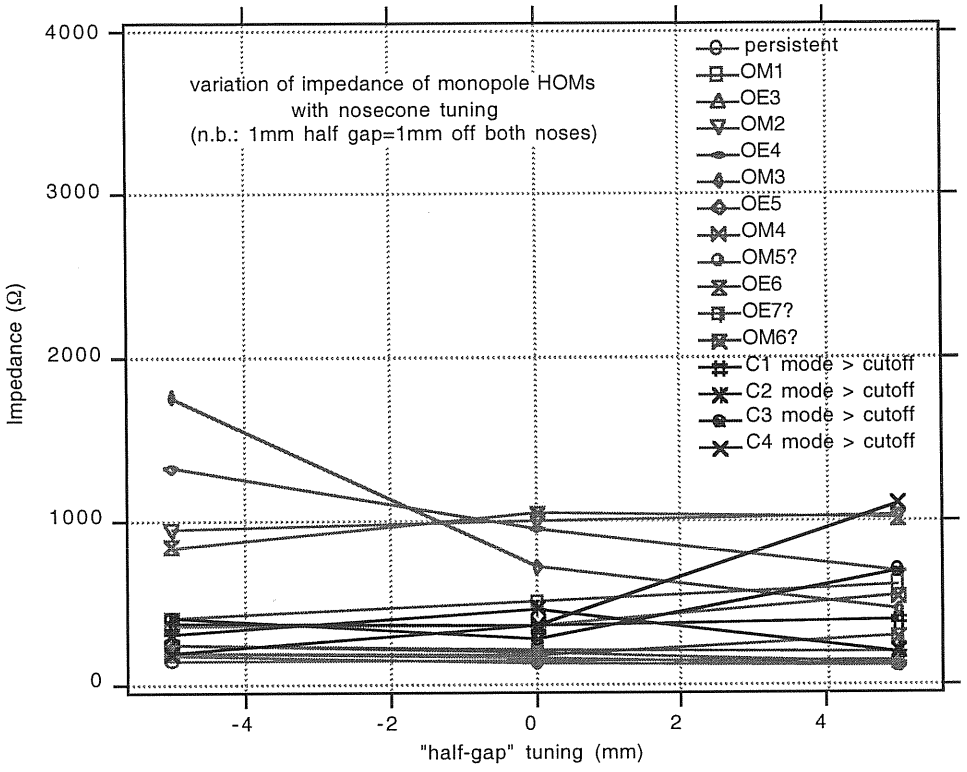

Figure 12. Variation of monopole mode strength with nose tuning.

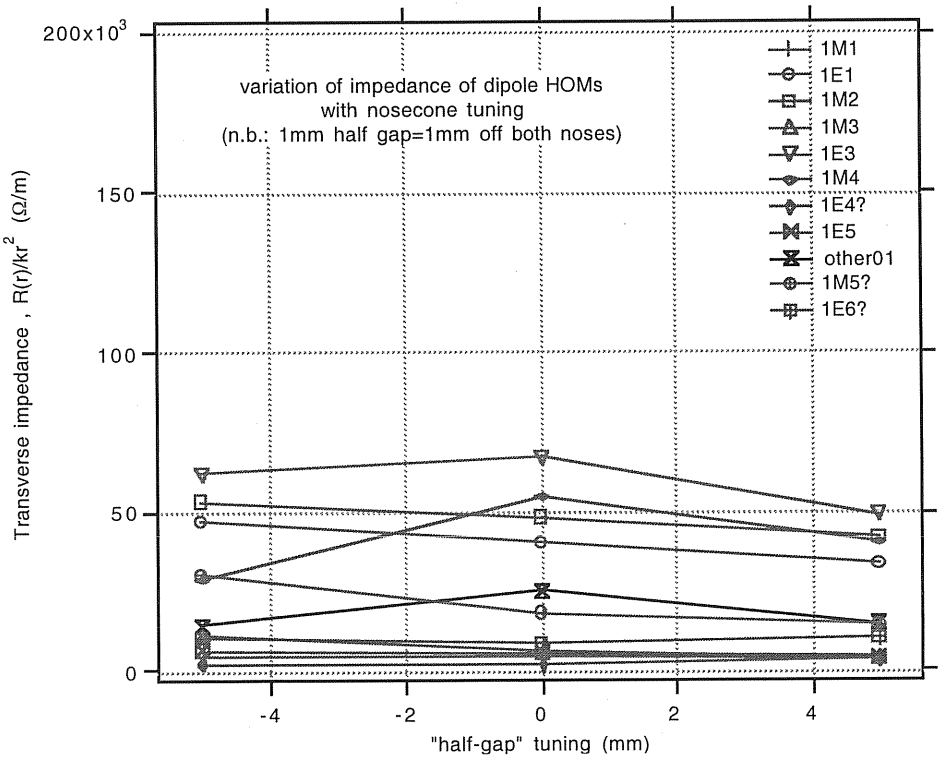

Figure 13. Variation of dipole mode strength with nosecone tuning.

1.4 HOM waveguide shape

The HOM waveguides have a cutoff frequency of 900 MHz which is below the lowest HOM frequency but sufficiently above the fundamental mode to give good rejection. For the PEP-II cavity the cutoff frequency was 600 MHz and the width was considered too great to penetrate the cavity directly (more than half of the wall current would be intercepted). To avoid this a narrower iris was placed between the cavity and the waveguide, see figure 14a. The width of the coupling iris was determined by experimentation on a pillbox model [8]. The height of the waveguide was kept small to minimize loss of cavity wall area. The wide flat profile resulted in a small radius of curvature at the ends of the iris, which, combined with the small blend radius between the waveguide and the cavity body, led to a significant current concentration and "hot spot" on the cavity wall [9], see figure 15. This hot spot dominated the cooling channel requirements and produced the highest stresses in the body. Possible variations on this cross section include a taller slot, figure 14b, or the use of a ridged "dumbbell" profile, figure 14c, which results in a narrower guide for the same cutoff frequency. The increased height at the ends of the slot and dumbbell allows a greater radius of curvature and together with an increased blend radius reduces the peak surface losses, temperature and stresses significantly. Other shapes considered for HOM damping or the fundamental mode coupler included ridged circular ports and coaxial lines. We have chosen the "dumbbell" geometry as our baseline design due to its reduced current density and good HOM properties.

To evaluate the effects of these geometry changes the surface heating due to RF losses was calculated in ANSYS using a new high frequency electromagnetic element (see sec 2). This finite element code gives a much more accurate calculation of the maximum power density and the distribution than can be obtained from the finite difference MAFIA mesh.

As a reference design a 2/3 scale model of the PEP shape was run, resulting in a total cavity dissipation of 41 kW, or 6.8 kW per sixth. In this size, the iris dimensions are 142 mm long by 16.93 mm tall, with an 8.5 mm blend radius into the cavity. The maximum heat flux is 77 W/cm^2, shown in figure 15, and the "hotspot" shows the characteristic shape with two maxima, previously observed for the 476 MHz PEP-II cavity. Note that the contours are not completely smooth since this model was run with a comparatively large mesh size, and the heat flux values were not averaged.

Another HOM port shape investigated for the NLC cavity is the generic "slot" design, which consists of a simple, constant cross-section racetrack, with outside dimensions of 166.7 mm by 33.86 mm. This racetrack shape is blended into the cavity with a 15.88 mm radius (5/8") all the way around. This port is much longer than the PEP iris, but it allows a much larger blend radius, and this radius turns out to be the dominant dimension in heat concentration. As can be seen in figure 16, the maximum heat flux in the slot port is approximately 61 W/cm^2, which is more than 20% lower than the iris design.

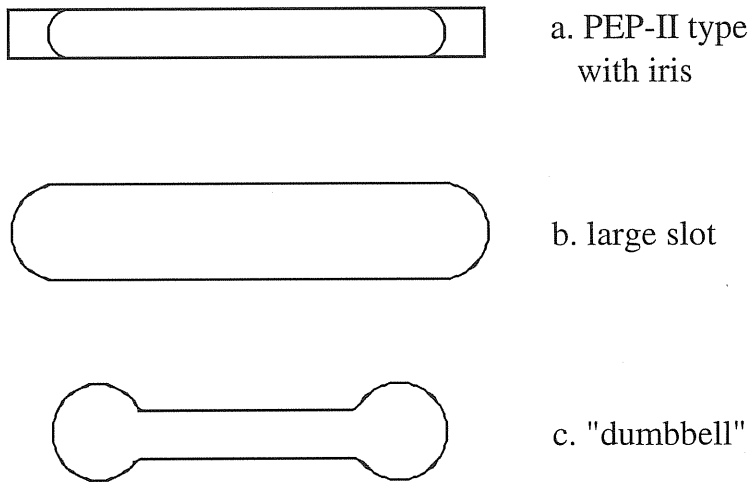

Figure 14. HOM waveguide cross sections with the same cut-off frequency (900 MHz), a: PEP-II type rectangular guide (with iris), b: large slot , c: compact ridged "dumbbell" guide.

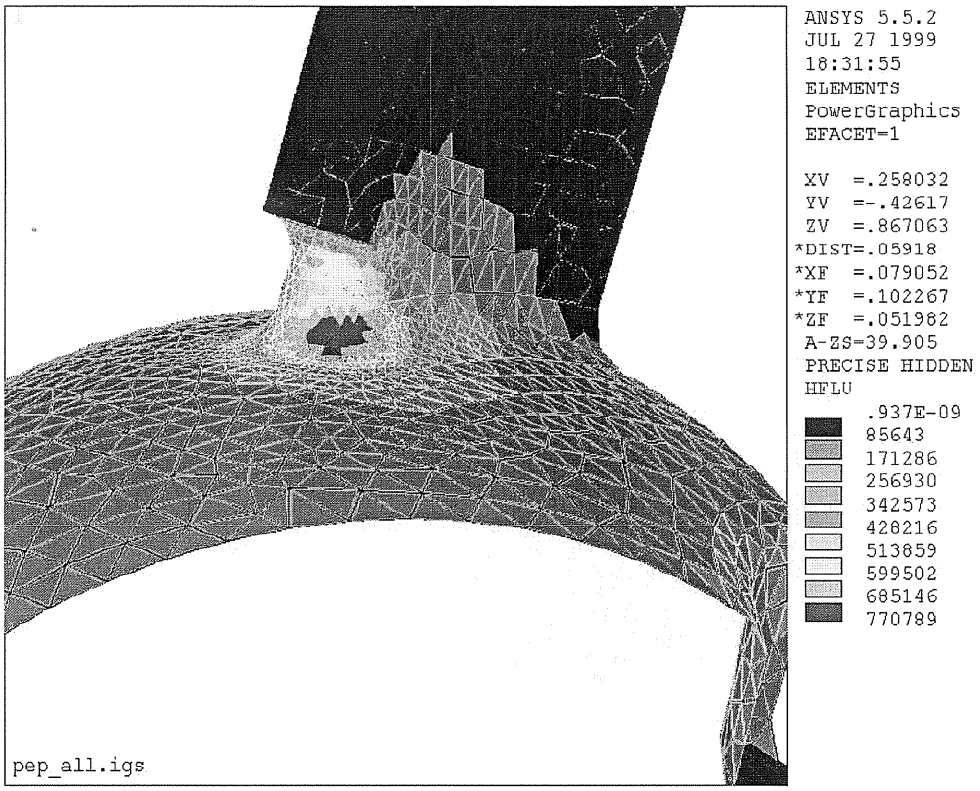

Figure 15. 714 MHz scaled PEP-II iris design, heat flux from ANSYS.

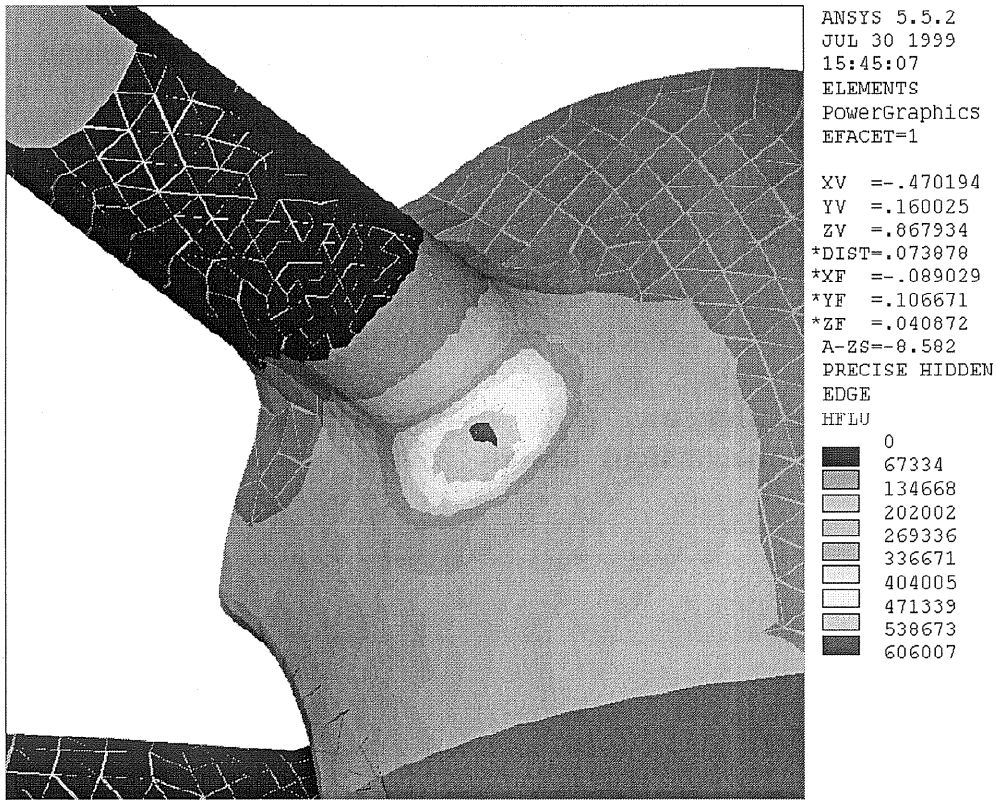

Figure 16. Alternative HOM "Slot" design, heat flux from ANSYS.

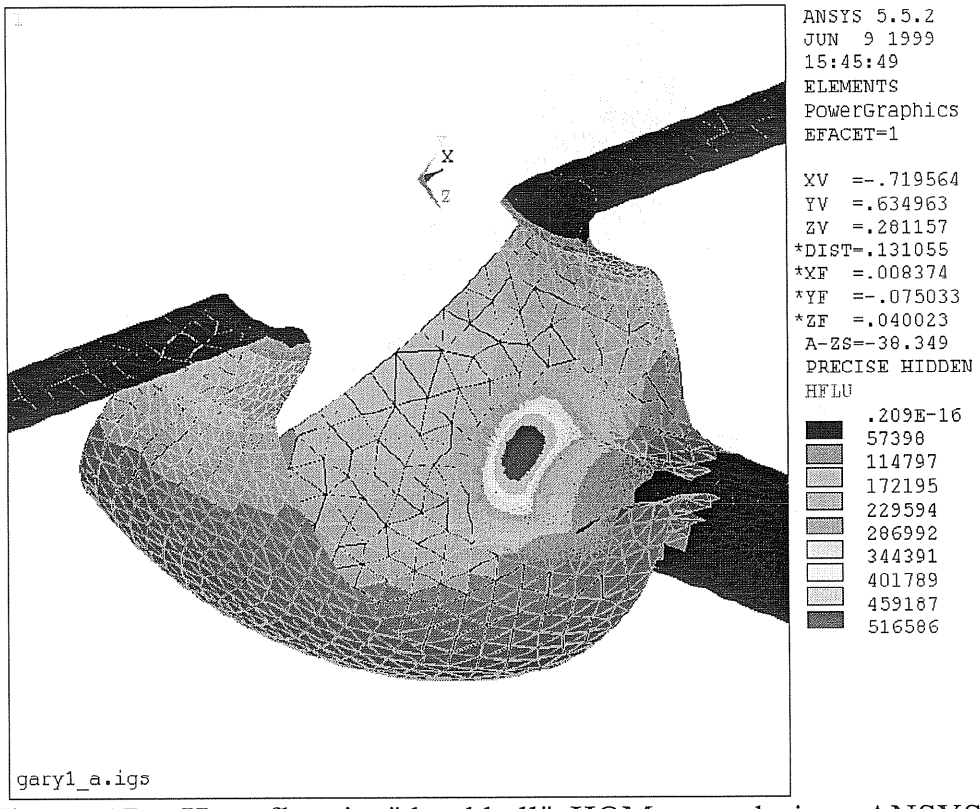

Figure 17. Heat flux in "dumbbell" HOM port design, ANSYS.

The "dumbbell" HOM port design utilizes a wide blend radius, reduced width and a narrower middle section. The overall dimensions of the port in this analysis are 139.7 mm by 33.86 mm, with the same blend radius as the slot design, 15.88 mm. (Note that these dimensions were adjusted slightly for the final design). Studies showed that the slot achieves the best HOM damping but the dumbbell results are similar and both are better than the iris. The dumbbell succeeds in reducing the maximum heat flux to just under 52 W/cm^2, see figure 17, a 15% improvement in heat dissipation compared to the slot and 33% lower than the iris, a significant advantage in the mechanical design.

1.5 HOM waveguide position

The location of the HOM ports on the cavity body is important to ensure that all HOMs are damped so that the residual impedance is within acceptable limits. A useful guide is to study the magnetic field distribution of all of the monopole and dipole modes below the beam pipe cut off and to avoid waveguide locations where any HOM has zero field. With a parameterized MAFIA model it is possible to investigate many cases before making the cold-test model. One of the parameters that was studied was the effect of the HOM port location, defined by the angle between the HOM waveguide axis and the beam axis. The HOM ports are chosen to be normal to the surface of the cavity for simplicity.

The strongest residual longitudinal mode in these models (OE4) is not strongly affected by the waveguide position because it has uniformly weak magnetic field on this part of the cavity wall but it is quite strongly damped through the main power coupler and so is reduced to an acceptable level in the full model. Of the other modes there is a tradeoff between the 0E6 mode which decreases with smaller angle, see figure 18, and the 0M2 mode which increases, see figure 19. Figure 22 shows the variation of longitudinal impedance at angles from 30° to 45° for a model with three HOM waveguides but no coupler. The optimum angle is between 30° and 35°. Most of the longitudinal HOMs are damped to the order of 1 kΩ or below (all of them once the coupler is included, see section 1.7). Two of the remaining modes are above cutoff (3.67 GHz and 4.67 GHz).

The transverse impedance of the dipole modes has a similar variation to the monopole modes, with a tradeoff between the 1E3 mode, see figure 20, and 1M4 mode, see figure 21. Figure 23 shows the variation of transverse impedance at angles from 30° to 45°. The optimum position is close to 30°. Note that the highest two transverse modes are not fully resolved in the 100m wakefield runs so the absolute amplitudes of these modes in figure 22 may be underestimated, but the relative changes with HOM position remain a useful guide. The actual values may be obtained by narrow-band runs on each mode in turn.

The HOM port angle for the NLC cavity conceptual design was chosen to be 30° (same as PEP-II) and MAFIA simulations with the coupler in place and tuner ports at 120° and 240° on the equator showed acceptable damping of all of the modes.

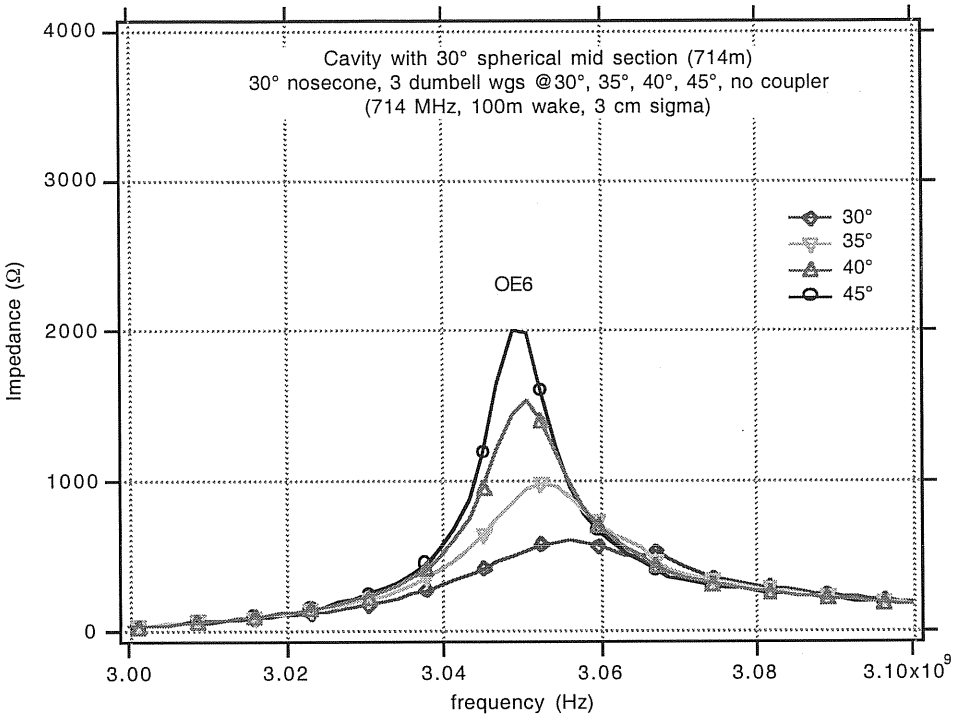

Figure 18. variation of OE6 mode with HOM angle (no coupler).

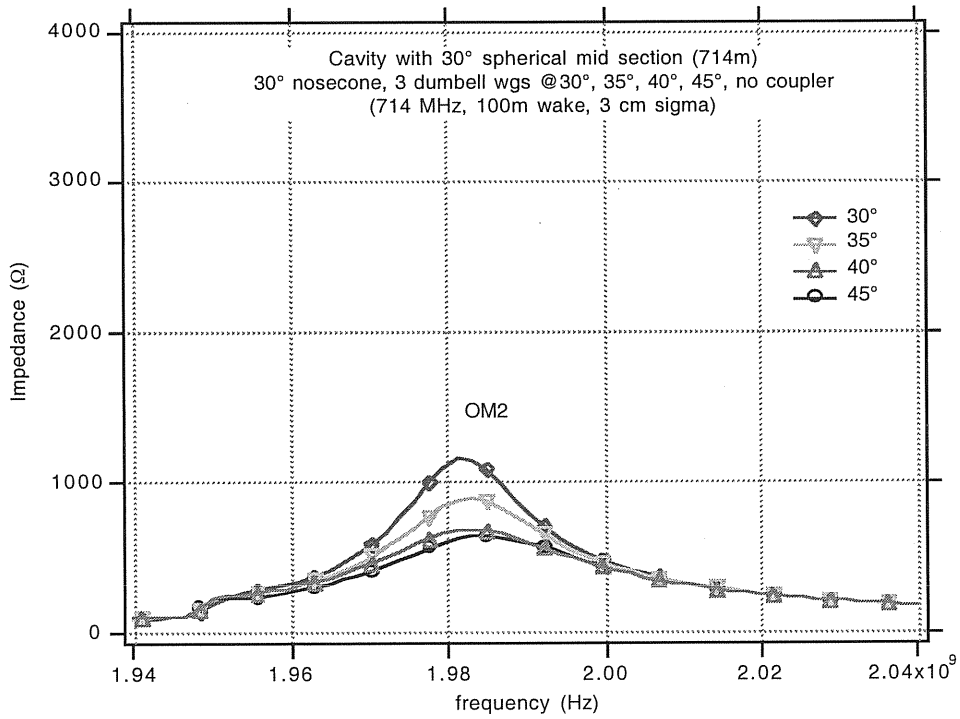

Figure 19. Variation of OM2 mode with HOM angle (no coupler).

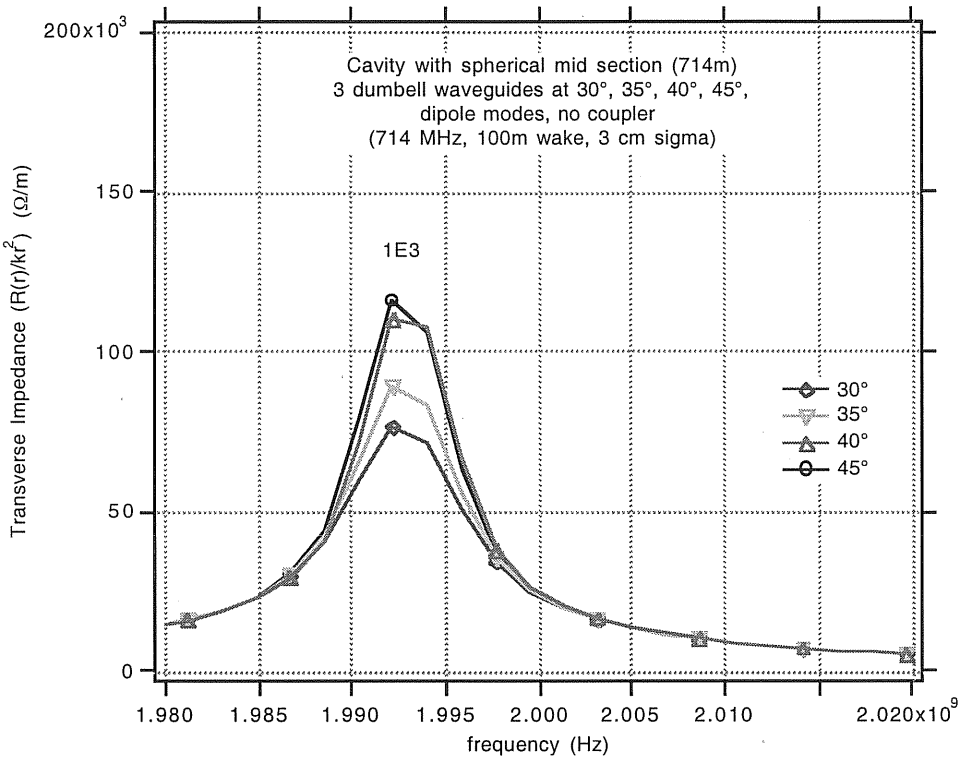

Figure 20. Variation of 1E3 dipole mode with HOM angle (no coupler).

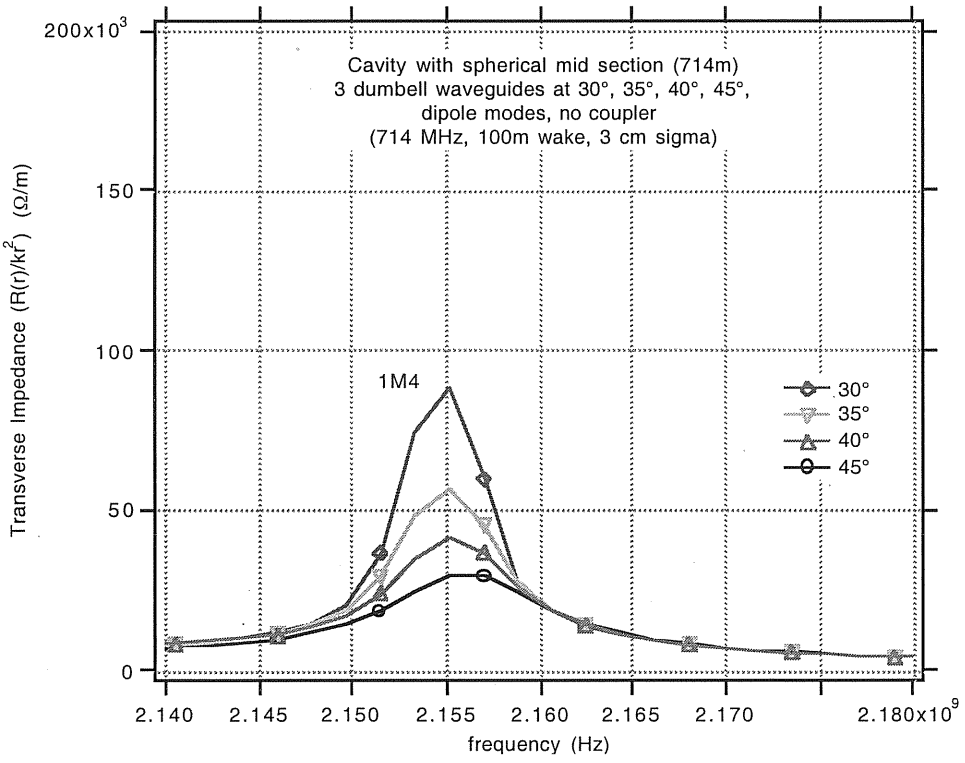

Figure 21. Variation of 1M4 dipole mode with HOM angle (no coupler).

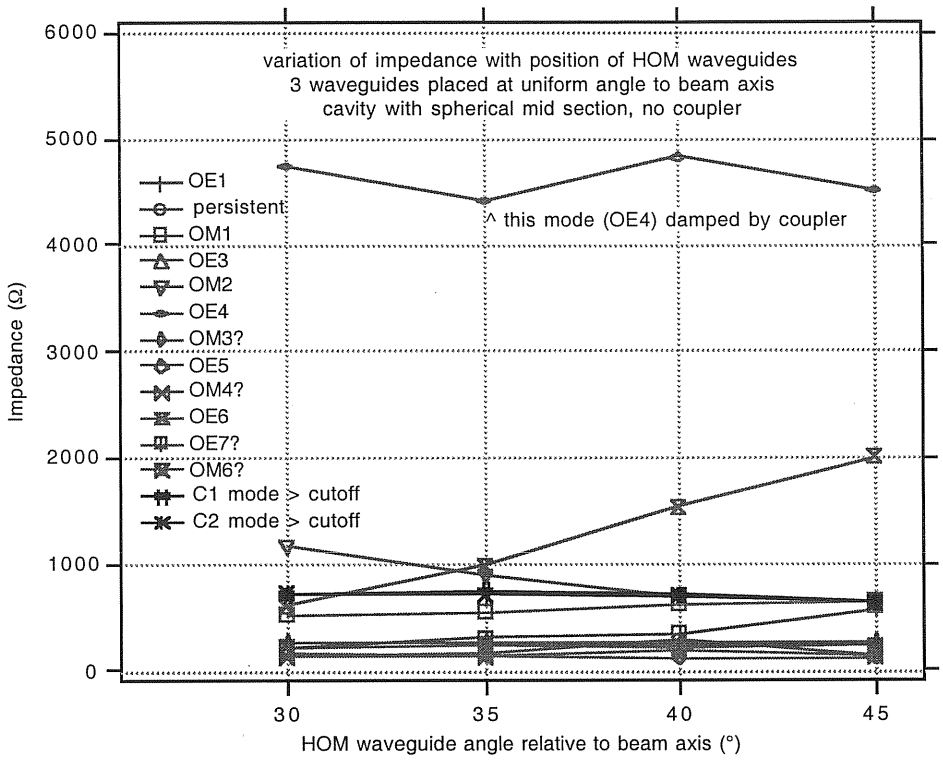

Figure 22. Variation of longitudinal impedance with HOM port angle.

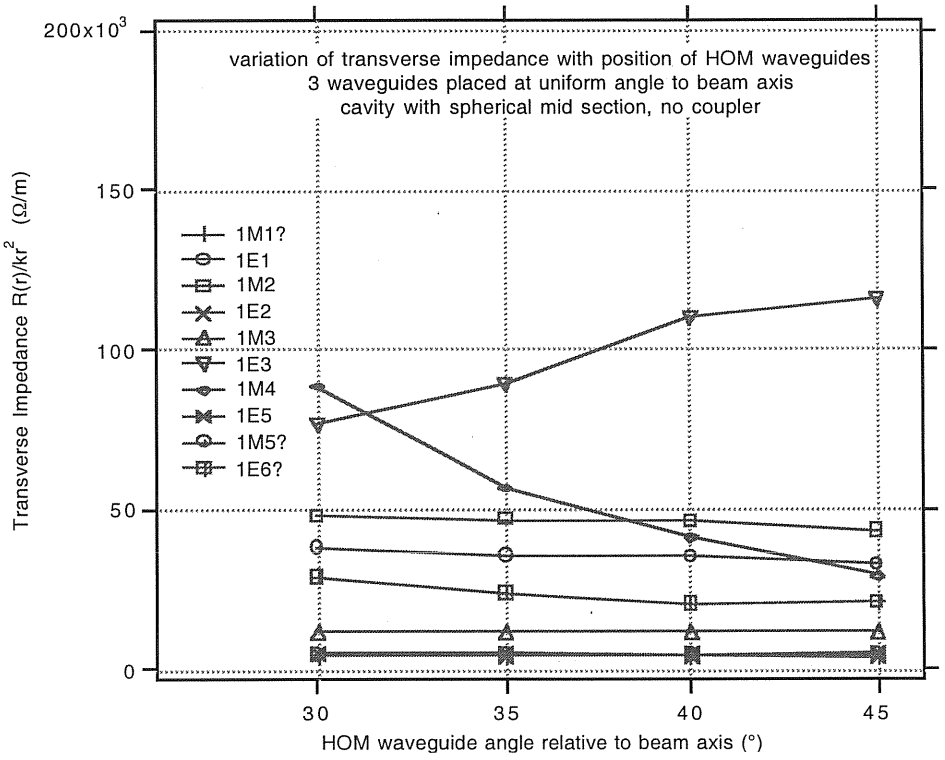

Figure 23. Variation of transverse impedance with HOM port angle.

1.6 Coupling options

It is proposed to use magnetic coupling through an aperture to deliver power into the cavity. This has the advantage of lower surface currents and simpler geometry compared to loop coupling, which would require water cooling in the loop. In PEP-II the aperture coupler was offset from the mid plane of the cavity to assist in damping some modes. For the present NLC design, simulations were performed with the coupler on the mid plane, offset by half of its width (as per PEP-II) and in between (i.e. offset by one quarter of it's width). Figure 24 shows how the strengths of the longitudinal modes vary with coupler offset. For many modes there is little or no effect, but there is an approximately 9% reduction in the strongest residual mode, 0M2, with the largest offset. Any further offset results in the next strongest mode, 0M5, increasing to negate any benefit. Figure 25 shows the behavior of the transverse modes; there is no significant effect due to the coupler offset.

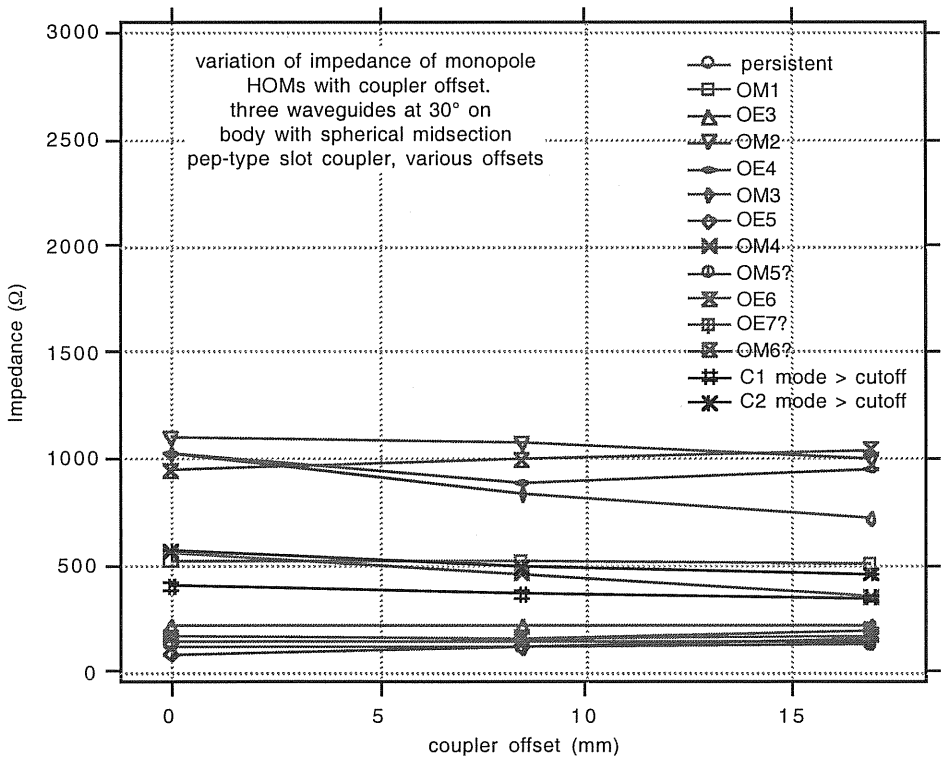

Figure 24. Variation of monopole modes with coupler offset.

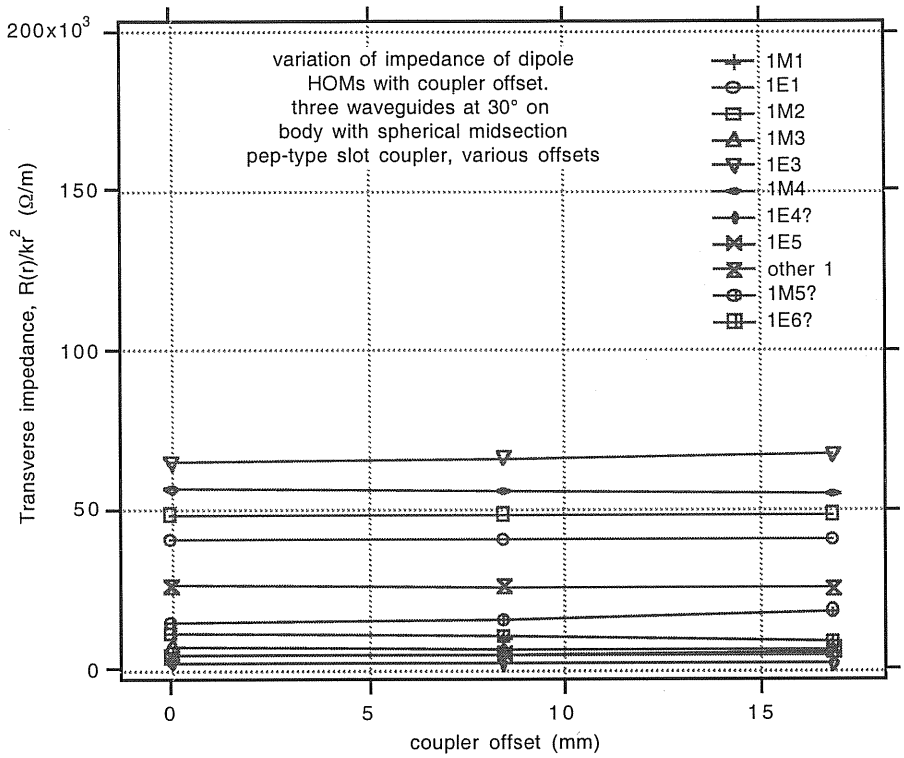

Figure 25. Variation of dipole modes with coupler offset.

The spherical profile of the center part of the cavity was chosen to allow circular ports on the cavity mid plane to be easily manufactured. This benefits the tuner and observation ports but not the slot coupler. It would be advantageous therefore to use a round coupler on the mid-plane if the HOM performance were comparable. Figure 26 shows the monopole mode spectra for an offset slot coupler and a 120 mm circular coupler on the mid-plane. On close inspection there is a 30% increase in the 0E4 mode, see figure 27, but it may be acceptable. Figure 28 shows the dipole mode spectra. There is a large (232%) increase in the 1E1 mode, figure 29, which becomes the strongest deflecting mode in the cavity. This may be acceptable if the transverse feedback system has sufficient headroom to maintain control. The transverse feedback system must be sized to handle the resistive wall driven instabilities, which may be greater than the residual cavity modes. One disadvantage of the circular coupler is that the cut-off frequency is higher than the PEP-type slot, even for the biggest port than can be fitted without interfering with the HOM ports. This reduces the penetration of the fundamental mode so the port must be shorter to maintain the desired coupling. It is not clear that a flange joint can be accommodated in this case, whereas it is hoped to include one with the slot coupler.

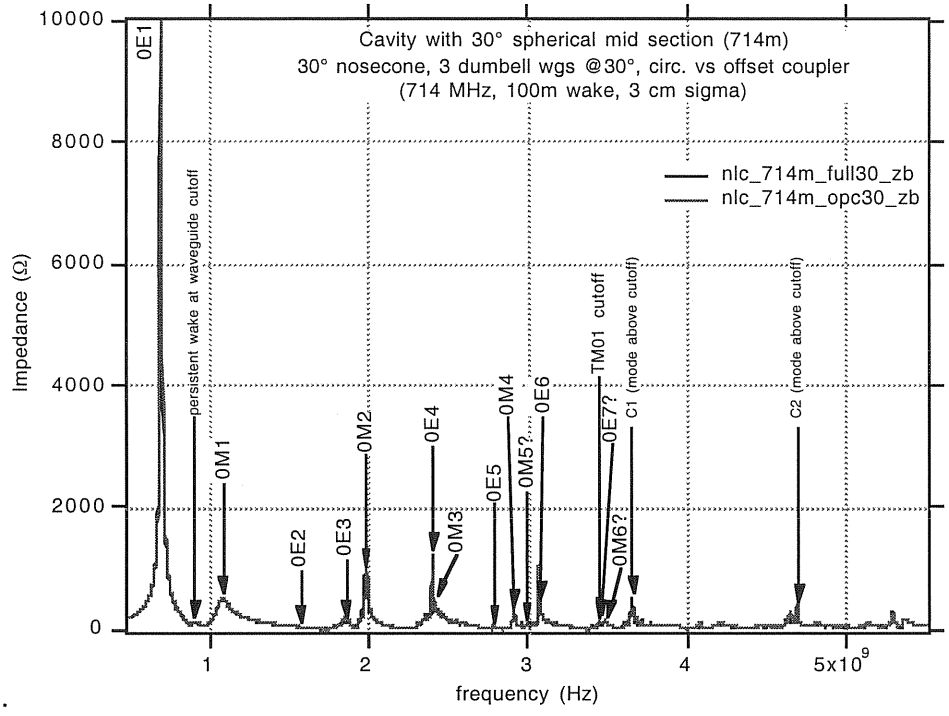

Figure 26. Monopole mode spectra for slot and round couplers.

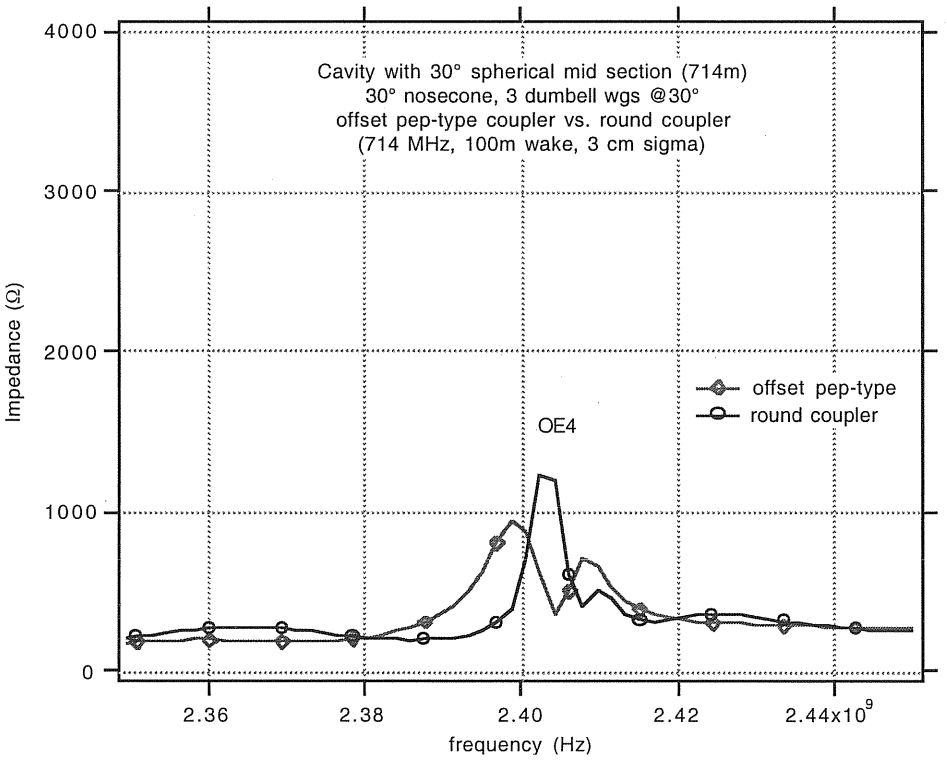

Figure 27. Monopole OE4 mode for slot and round couplers.

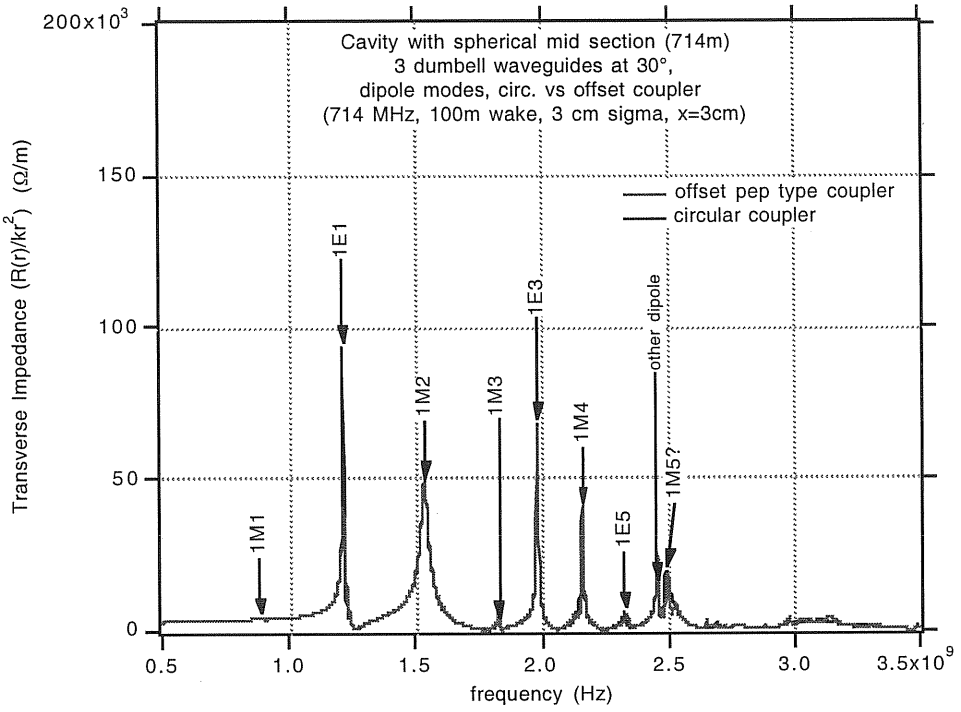

Figure 28. Dipole mode spectra for slot and round couplers.

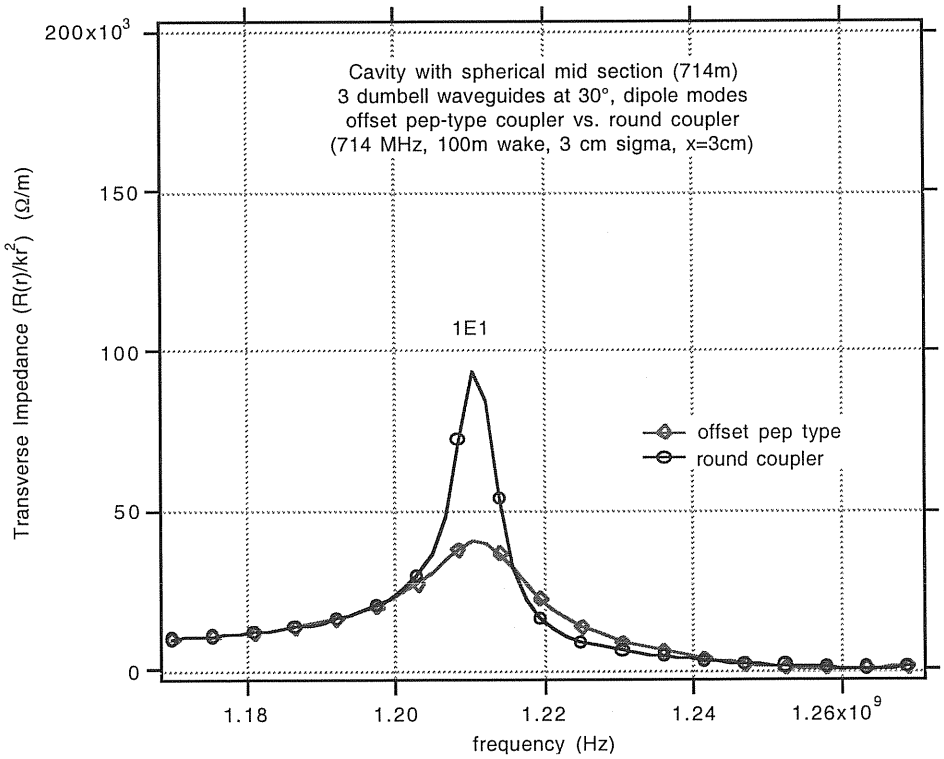

Figure 29. Dipole 1E1 mode for slot and round couplers.

A compromise between the large circular aperture and the slot may be to use a ridged circular port, figure 30, which is more compact than the slot, figure 31, but has the same cut-off frequency. This was simulated in the MAFIA model but, like the circular coupler, did not have quite as good damping as the slot for the transverse modes. This option as well as other possibilities such as a ridged slot or dumbbell shape may be explored further in the future.

Figure 32 shows the MAFIA geometry models used for the offset PEP-type coupler (a) and the circular coupler (b). Note that in the MAFIA models the HOM waveguides are bent parallel to the beam axis to allow the waveguide boundary condition to be used. In reality they will go radially out to the flanges.

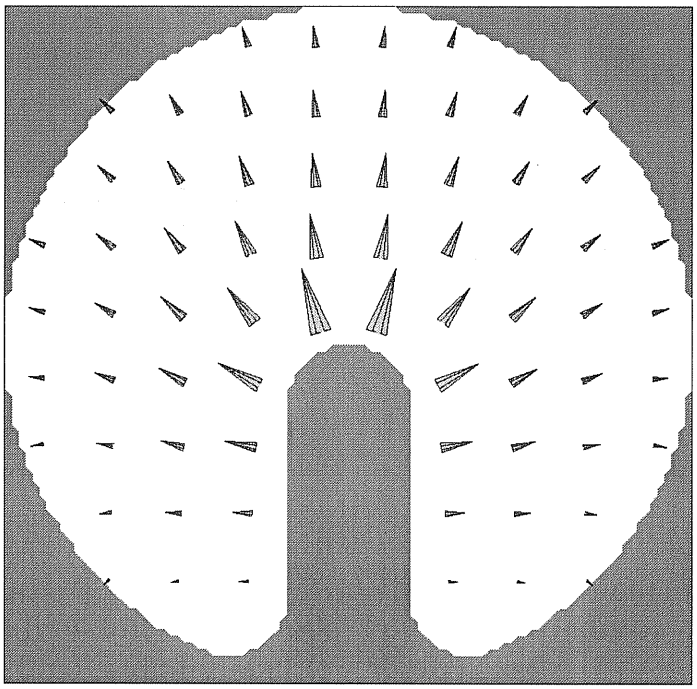

Figure 30. MAFIA 2D solution of E-field in ridged 93mm diameter circular coupler.

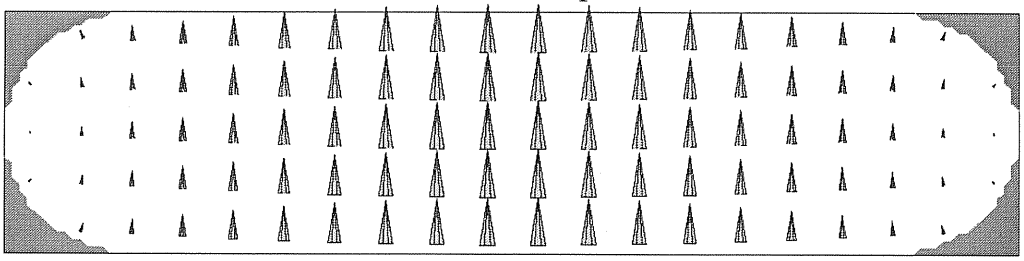

Figure 31. MAFIA 2D solution of E-field in PEP-II type slot coupler (135.5mm wide).

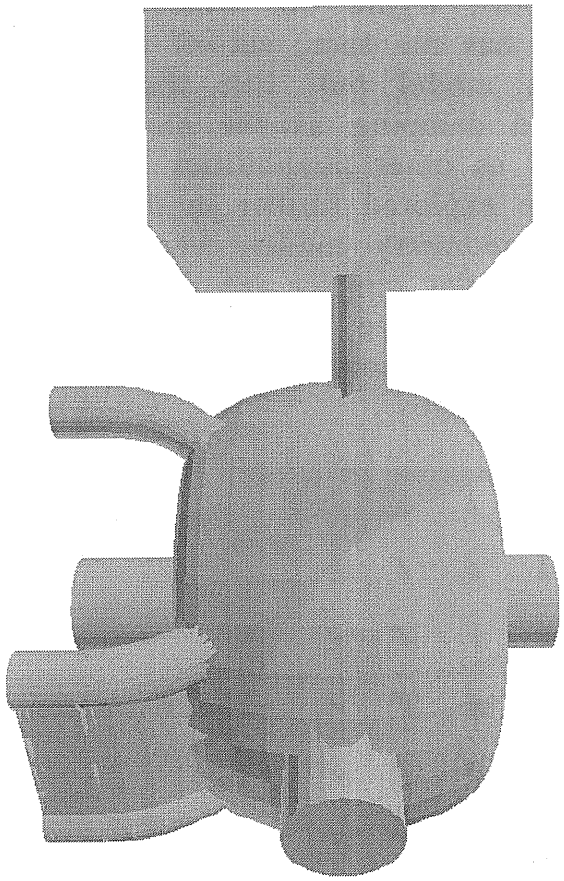

Figure 32a. MAFIA model with offset PEP-type coupler.

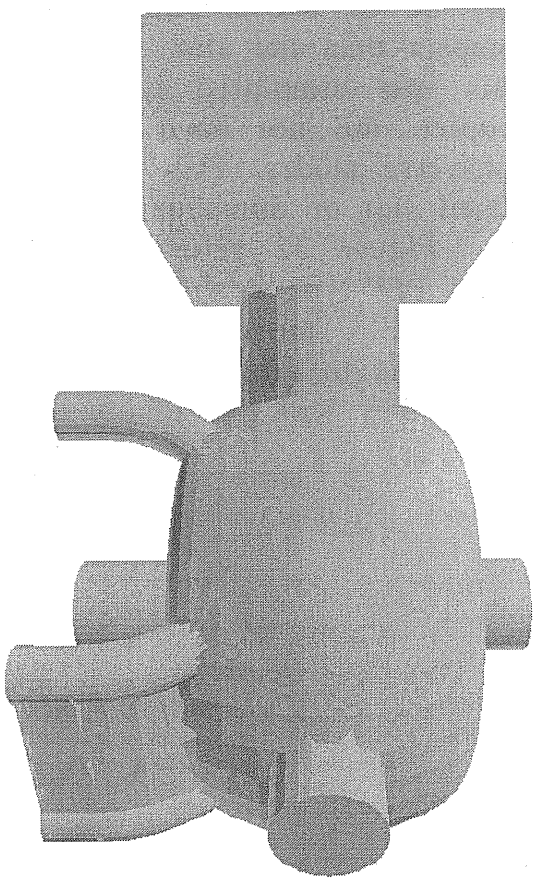

Figure 32b. MAFIA model with round coupler.

1.7 Summary of proposed NLC cavity RF design

The proposed NLC damping ring cavity, see figure 33, bears a strong resemblance to the PEP-II cavity on which it is based. Modifications to the shape have been made to improve the HOM damping, lower the mechanical stresses and simplify the construction. The cavity body has been adapted from the traditional toroid to a shape with a spherical mid section and a generous blend to the end wall. Simulations of many combinations show that a profile with spherical section ±30° from the mid-plane and a blend of 40 mm to the end wall has a good distribution of HOMs, a high shunt impedance and fits well with proposed fabrication methods.

The nosecone angle has been studied with regard to the effect on HOM damping and the 30° angle chosen for PEP-II was found to be about optimum and will be used again. The beam pipe radius at the cavity is chosen to be in approximately the same proportion to the cavity as for PEP-II. Reducing the diameter would increase the shunt impedance but would also increase the transverse loss parameter to an unacceptable degree.

The HOM waveguides have a slightly ridged "dumbbell" profile which gives an optimum width for the desired cutoff frequency and a large radius at the ends of the slots. This, combined with a generous blend into the cavity wall, results in significantly lower peak currents, temperatures and stresses than the PEP-II shape. The position of the HOM ports on the cavity body has been extensively studied and the optimum location has the waveguides exiting at a 30° angle to the beam axis, normal to the surface on the 40 mm blend part of the profile. A PEP-type slot coupler is used to couple to the waveguide and also gives some useful extra damping to some modes. The coupler is offset from the mid-plane to give better coupling to the antisymmetric modes (which have no magnetic field on the mid-plane for the simple cavity, and are given the URMEL "M" notation). A circular coupler could be used but at some penalty to the strongest remaining HOMs.

Figure 34 shows the electric field of the fundamental mode calculated by URMEL and table 3 gives some of the relevant parameters for this profile. For comparison the parameters of the 3D MAFIA model are shown, including the HOM damping waveguides, coupler and tuner ports. The Q is about 14% lower than a MAFIA calculation with no apertures, which is part of the 70% factor applied to the 2D calculation (the factor commonly applied to the MAFIA result is ~80%). We used the more conservative estimate (3.0 MΩ, 41.7 kW), for the thermal and stress analysis. Note also that because

the 3D mesh is coarser and uses bricks instead of triangles the peak electric field on the surface is not as well resolved. The frequency is lower because of the extra volume of the apertures. The tuner ports will of course be filled with tuners but a small correction to the geometry will be required to correct for the remainder. The present parameters for the damping rings and positron pre-damping ring are shown in table 4. Tables 5 and 6 show the modes below cut-off for the simple 2D cavity shape, calculated by URMEL, and the estimates of the strengths of the remaining modes in the 3D damped cavity with coupler, calculated by MAFIA in the time domain (including four longitudinal modes above cut-off).

Figure 35 shows how the longitudinal coupled bunch instability threshold varies with frequency. The cavity impedance is within acceptable limits for the damping rings even without longitudinal feedback. The design is marginal for the present pre-damping ring parameters but could be stabilized with a modest feedback system or by increasing the number of HOM ports on the cavities. The dipole mode spectrum is better then the PEP-II design but still above the threshold for transverse coupled-bunch instabilities, see figure 36. The beam can be stabilized with a modest feedback system which may also be required because of modes driven by the resistive wall.

The cavity will have two tuner ports, one of which will have a motorized tuner to dynamically compensate for beam loading and temperature changes. The other will be a fixed plunger which will be adjusted to fine tune the cavity frequency after fabrication. The proposed design has three small ports, one opposite each tuner and one opposite the coupler. One of these will be used for the RF pickup loop (most likely the one opposite the coupler), while the other two may house an arc detector or a TV camera to allow observation of the tuners during cavity conditioning. This is very useful, especially if spring fingers are incorporated in the tuner design, as the TV camera can be used to monitor them remotely to watch for sparking.

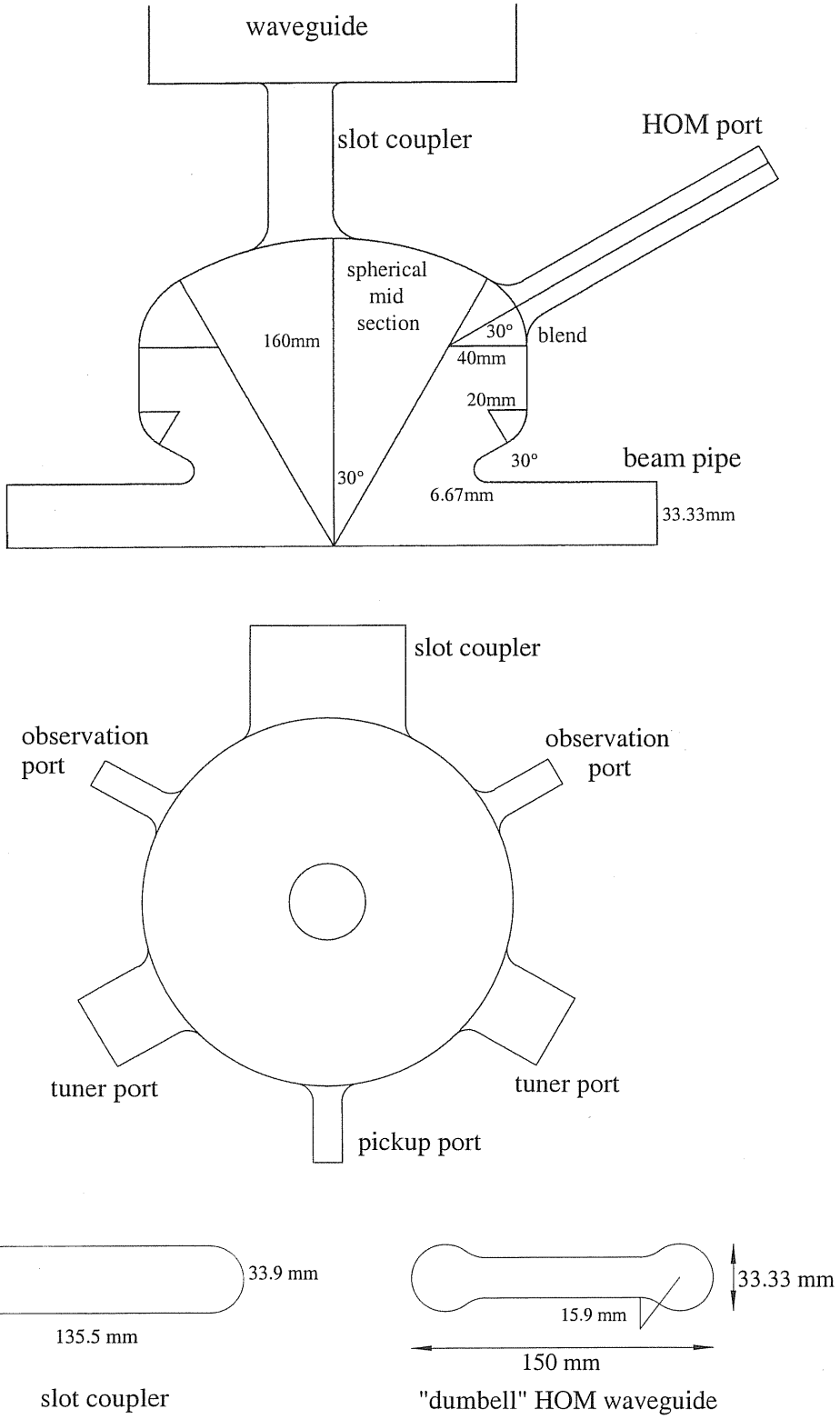

Figure 33. Proposed NLC cavity geometry.

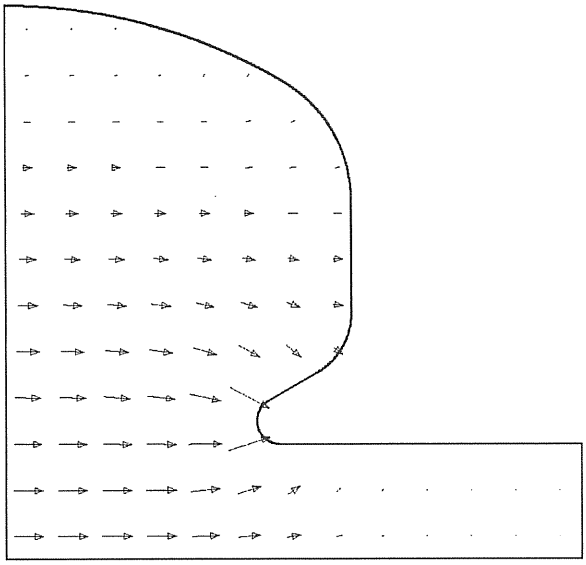

Figure 34. Electric field of accelerating mode (URMEL).

Table 3. Basic parameters for profile 714m.

parameter	2D (URMEL)	3D (MAFIA)
RF frequency, MHz	714	704*
R/Q, Ω	118	117
Qo	36182	34609
Rs ($V^2/2P$), MΩ	4.27	4.064
Est. attainable Rs, MΩ	3.0 (70%)	3.25 (80%)
Voltage, kV	500	500
Power (est), kW	41.7	38.5
Pk surf. E field,MV/m	9.15	7.86
Kilpatric, MV/m	25	25

* no tuners

Table 4. Damping and pre-damping ring parameters

parameter	Damping ring	Pre-damping ring
RF frequency	714 MHz	714 MHz
Current	750 mA	800 mA
Energy	1.98 GeV	1.98 GeV
fo	1 MHz	1.373 MHz
fs	6.97 kHz	22.8 kHz
alpha	6.602e-4	3.39e-3
trans. damp. time	5.2 ms	5.4 ms
energy damp. time	2.5 ms	2.5 ms
threshold Zlong	2e13/f Ω	1e13/f Ω
threshold Ztrans	100 kΩ/m	72 kΩ/m
# cavities	3	4

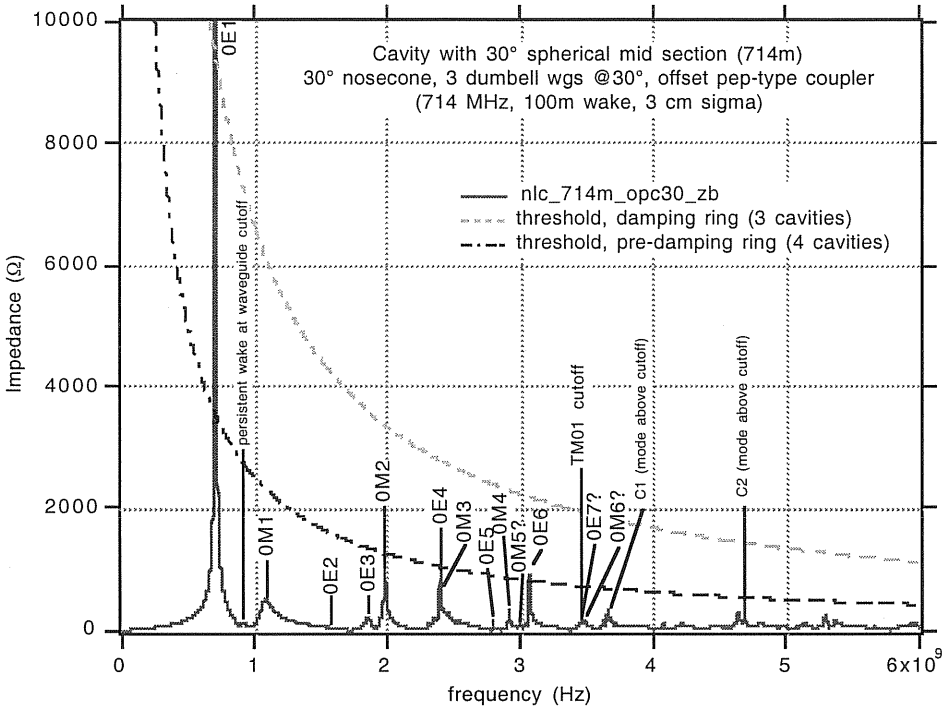

Figure 35. Longitudinal impedance spectrum with thresholds.

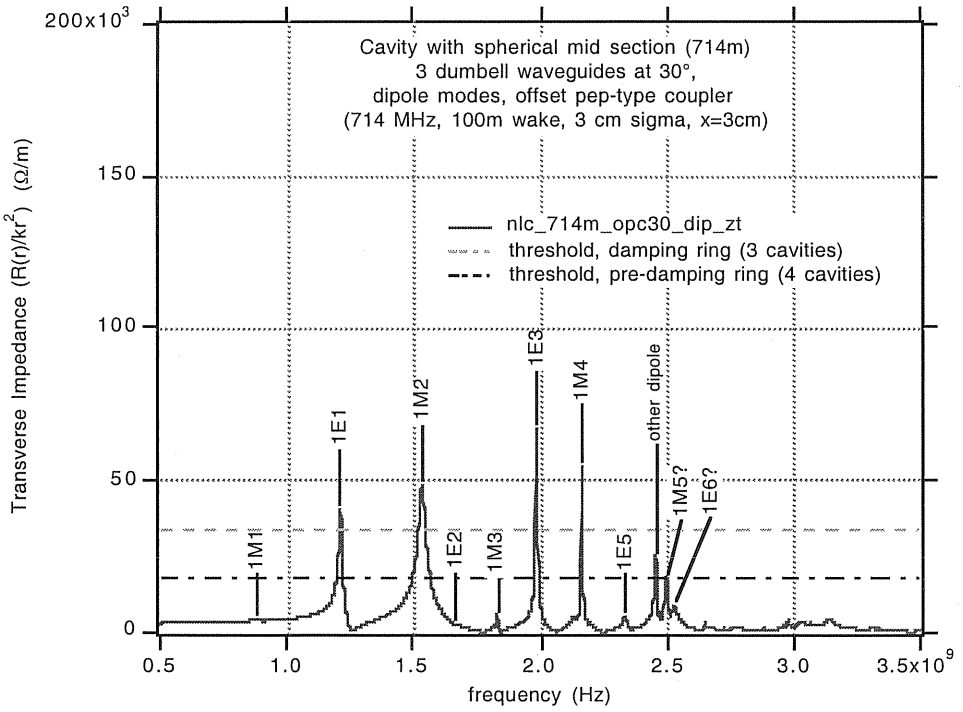

Figure 36. Transverse impedance spectrum with thresholds.

Table 5. Calculated monopole HOMs , 2D and 3D.

mode type	Freq. 2D	R/Q 2D	Qo 2D	Rs† 2D	MAFIA T3*	MAFIA T3
(URMEL)	(MHz)	(Ω)		MΩ	freq.(MHz)	Rs damp(Ω)
0-E-1	714	117.88	36182	4.265	703	3e6‡
pers.	-	-	-	-	906	140
0-M-1	1070	34.47	30720	1.059	1082	503
0-E-2	1572	0.07	34169	0.002	nv	nv
0-E-3	1851	4.60	73373	0.337	1859	212
0-M-2	1964	8.67	33846	0.294	1987	993
0-E-4	2399	6.37	33779	0.215	2399	949
0-M-3	2428	4.36	55666	0.243	2408	715
0-E-5	2739	0.10	104004	0.010	2785	161
0-M-4	2917	2.06	35676	0.074	2911	357
0-E-6	3073	3.79	53147	0.202	3065	1037
0-M-5	3100	0.02	82114	0.002	nv	nv
C1**	-	-	-	-	3657	349
C2**	-	-	-	-	4688	458
C3**	-	-	-	-	5295	273
C4**	-	-	-	-	6040	357

TM_{01} cutoff 3446 MHz, †$Rs=V^2/2P$, *model nlc_714m_opc30, ‡estimate based on frequency domain calculation and realistic loss of Q. ** modes above cut-off.

Table 6. Calculated dipole HOMs , 2D and 3D.

MODE TYPE	Freq. 2D	R/Q 2D	Qo 2D	R⊥† 2D	MAFIA T3*	MAFIA T3 V
	(MHz)	(Ω AT R0)		MΩ/m	freq.(MHz)	R⊥ (Ω/m)
1-M-1	1005	0.27	37180	0.432	881	4146
1-E-1	1211	13.31	51086	24.175	1210	40281
1-M-2	1535	34.65	37928	36.870	1534	48215
1-E-2	1661	0.25	38796	0.247	nv	nv
1-M-3	1828	0.66	73013	1.126	1827	5744
1-E-3	2004	9.42	38438	7.777	1981	67221‡
1-M-4	2154	7.50	31609	4.737	2161	54839‡
1-E-4	2238	0.01	67389	0.006	2208	1977
1-E-5	2333	1.44	55369	1.470	2333	5479
new					2454	25141
1-M-5	2504	0.61	41562	0.434	2498	18146
1-E-6	2541	16.16	33310	9.125	2525	8708

TE_{11} cutoff 2638 MHz, †R⊥=R(r)/kr^2, *nlc_714m_opc30, ‡ not fully resolved.

2. Cavity thermal and stress analysis

The RF losses for the PEP-II cavity were calculated using a purpose written boundary integral code [10] (which is unfortunately no longer available), and transferred to ANSYS [11], for the thermal and stress calculations. It is now possible to calculate the RF losses directly in ANSYS with the addition of a new high frequency electromagnetic element type [12]. To verify the ANSYS RF calculations the PEP-II design was re-analyzed using a completely new finite element mesh [5]. The RF losses were also computed using the Omega3p 3D code at SLAC [13]. Omega3p is a parallel distributed memory finite-element code for solving electromagnetic problems in the frequency domain for large complex three-dimensional geometries.

The calculation of the surface heating using ANSYS shows good agreement with the original boundary integral results and with those from the Omega3p code at SLAC. The analyses show the importance of good mesh refinement at the hot spots, achieved through operator input for the ANSYS mesh and by automatic adaptive refinement for the Omega mesh, with similar success. The wide availability of ANSYS and the rapid turnaround of results on even modest PC based workstations make this a very useful tool for future projects. The ANSYS analysis highlighted a discrepancy between the original numerical model and the as-built design resulting in an approximately 10% higher stress than previously thought. The PEP-II cavities are presently being operated well within their limitations however, and this is not a cause for concern. The stress analyses also showed the importance of the physical constraints at the ports, which must be free to move in response to thermal expansion of the cavity otherwise the stresses in the body may be as much as doubled.

The NLC cavity conceptual design has been analyzed using the same process of RF, thermal and stress calculation all within ANSYS using a common mesh. Figure 37 shows one the parameterized CAD model of one third of the cavity (generated in Pro Engineer [14]), which is used to define the geometry. This can be imported into ANSYS and meshed using the ANSYS pre-processor. One sixth of the geometry is used in ANSYS, including the cooling channels, to minimize the mesh size. Appropriate boundary conditions are applied to imply the rest of the cavity by symmetry. The individual ports can be constrained or free, to study the effect on the stresses. Figure 38 shows the ANSYS mesh. Note the increased density of elements around the HOM port opening in order to fully resolve the local current concentration which gives rise to the hot spot.

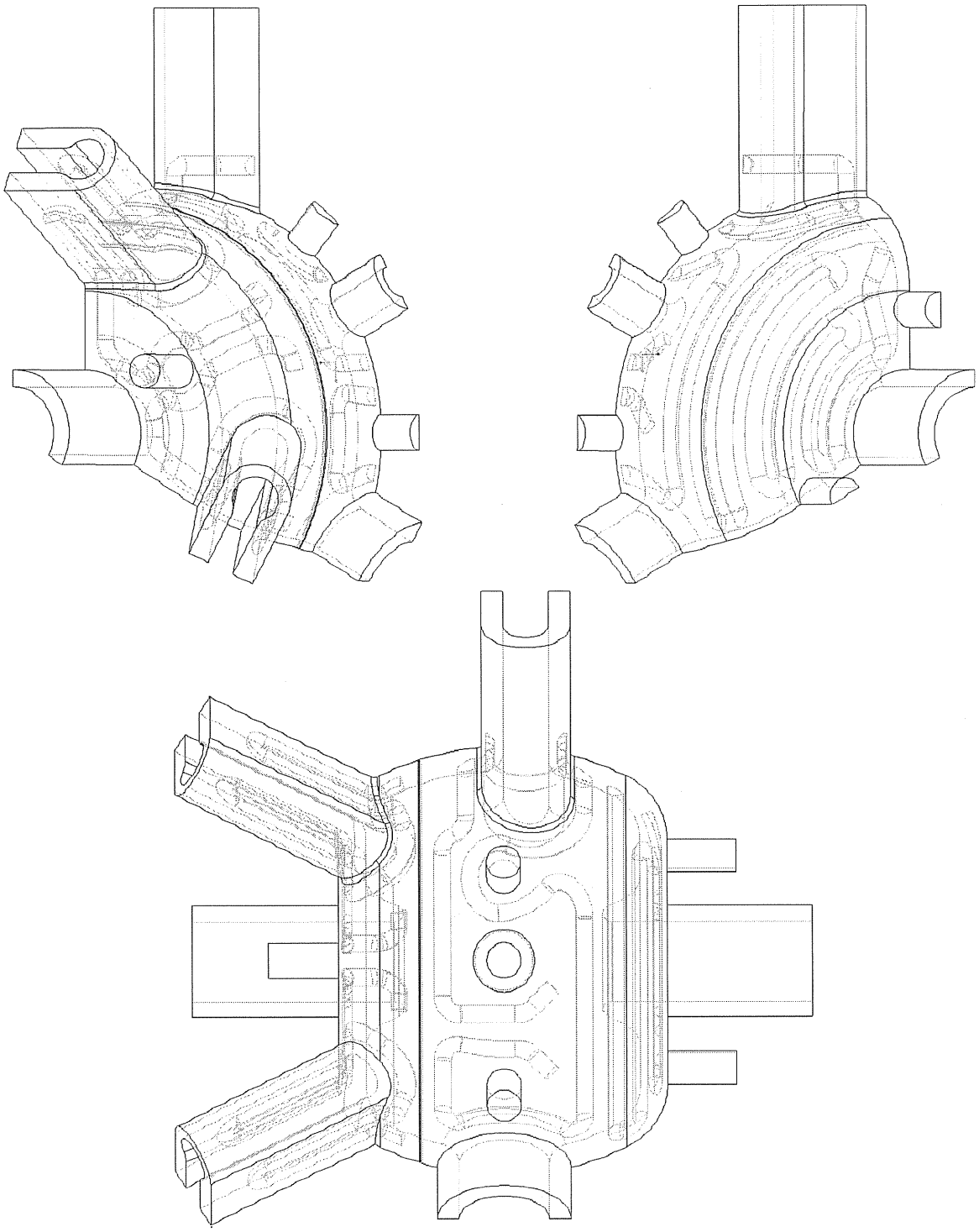

Figure 37. CAD model of one third of the cavity with cooling channels.

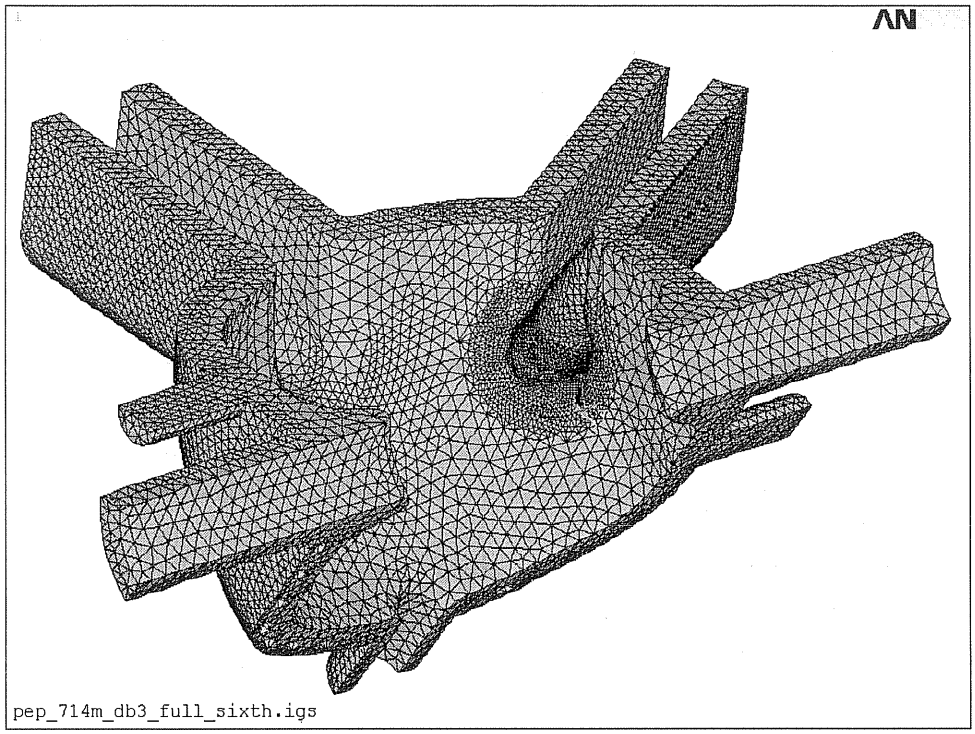

Figure 38. ANSYS mesh of one sixth of the cavity.

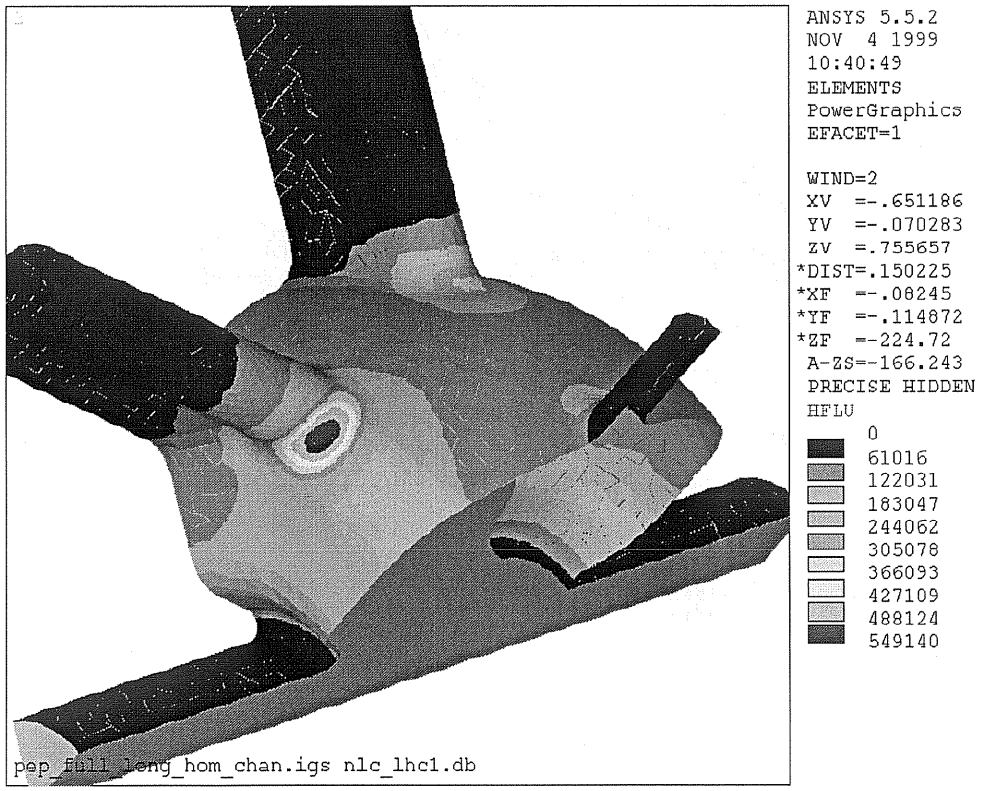

Figure 39. Surface power loss on proposed NLC cavity.

Figure 39. shows the power loss on the surface of the cavity calculated by ANSYS. Note the concentration at the end of the HOM port where it meets the cavity body, and the lesser concentrations around the coupling slot and the observation port. This power dissipation is calculated from the currents induced by the surface magnetic field and is used in subsequent thermal and stress calculations. The integrated heat flux is normalized to give a total body dissipation of 42 kW. The maximum value at the hot spot is about 55 W/cm^2, significantly lower than the scaled PEP-II geometry (77 W/cm^2). Figure 40 shows the temperature rise above the cooling channel temperature for this heat flux. Note the temperature at the HOM port hot spot is less than 30°C above the water temperature. (compare with 64°C rise for the PEP-II cavity at it's maximum design value of 150 kW [15], 42° C at its normal operating power of 103 kW). The water flow rate in the channels is assumed to be 4.1 GPM (15.5 l/min) per channel with a Reynolds number of 34,000 and a heat transfer coefficient of 18000 W/m^2°C. The temperature rise in each channel is estimated to be less than 4°C but this small change was not included in the simulations.

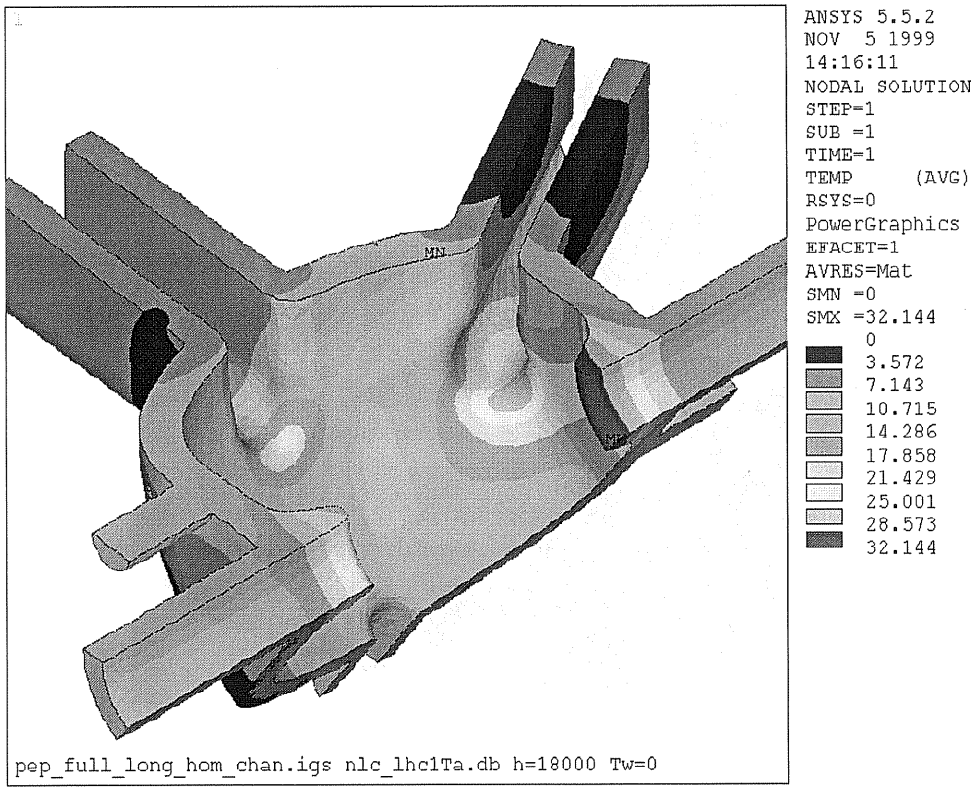

Figure 40. Cavity temperatures calculated by ANSYS.

Figure 41 shows the displacement of the body due to thermal expansion. The body is assumed to be all copper and unconstrained at all of the port boundaries. The model is axially constrained at the cavity mid-plane and radially constrained about the axis by symmetry. Notice that the largest displacement is at the end of the HOM port which is most susceptible to differential thermal stresses in the body. Although all of the displacements are very small (0.1 mm or less) any constraint of the ports may lead to higher stresses in the body, although a physical support which flexes only a small amount under the force of the expanding cavity will relieve a significant part of the extra stress.

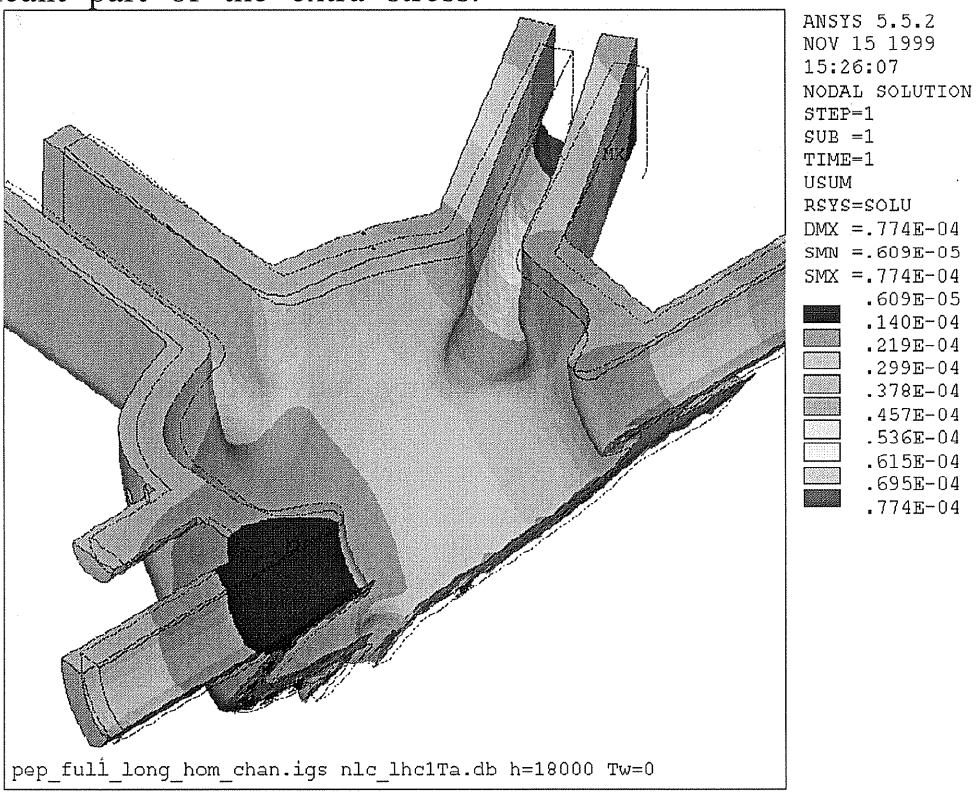

Figure 41. Displacement of the cavity calculated by ANSYS.

Figure 42 shows the Von Mises stress in the body calculated by ANSYS. Note that the stress at the hot spot is about 35 MPa (about 5000 Psi) which is well within the fatigue limit for 10,000 cycles which is about 18,000 Psi [16]. This stress can be compared with approximately 10,900 Psi (75 MPa), estimated for the PEP-II cavities at 150 kW. The model does not include atmospheric pressure but this is a small contribution to the total stress.

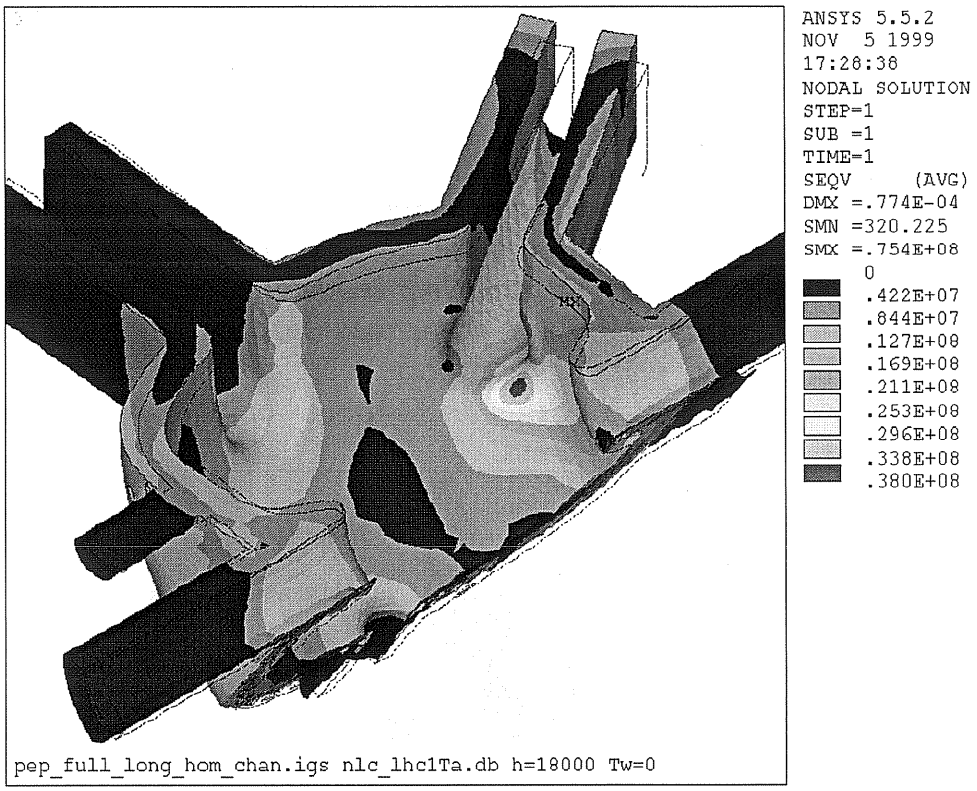

Figure 42. Von Mises stress in the cavity body calculated by ANSYS.

3. Cavity fabrication and assembly

The proposed NLC cavity is closely based on the PEP-II design and it is intended to use many of the same manufacturing methods. While the PEP-II cavity is a very successful design it is rather expensive to make and contains some features and uses some processes that may no longer be necessary or may be improved upon. For example, the use of very pure copper plating on the body (which is more difficult and costly), to allow a subsequent brazing step was eliminated in the NLC design. The modifications in the proposed NLC design reduce the RF current concentration in the HOM waveguide area and therefore lower the temperature and stress without reducing the effectiveness of the HOM damping scheme.

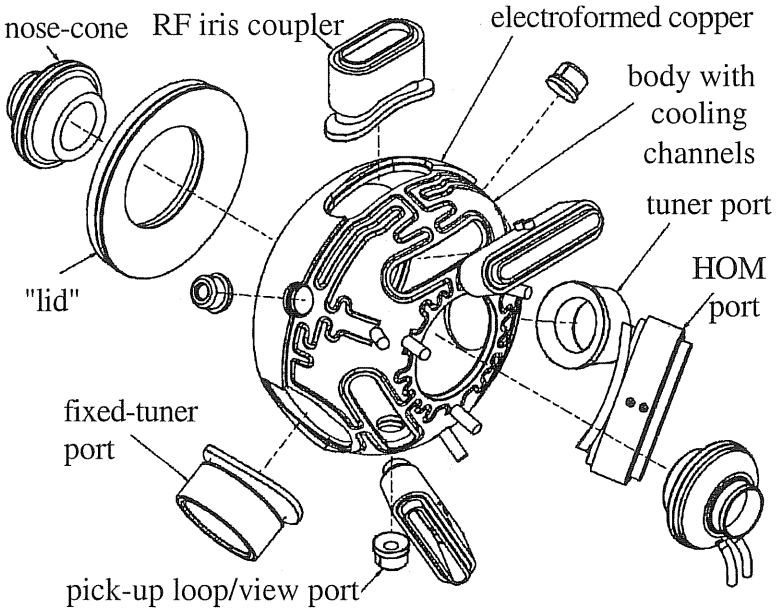

Figure 43. PEP-II cavity major components (minus flanges).

The PEP-II cavity mechanical design, see figure 43, evolved over several years from the original concept of an all-brazed assembly to one utilizing many different fabrication and joining methods, including brazing, e-beam welding, TIG welding, TIG brazing and electroplating. Some of these processes were applied to multiple separate parts, for example the main body section and the lid section were both electroplated to complete the cooling channels but this was done on each part separately before they were joined together by e-beam welding. Similarly each of the six ports and both

nosecones had their own internal cooling channels which were made by brazing on close fitting jackets or inserts before the ports were e-beam welded into the body.

For the much simpler ALS third harmonic cavities, figure 44, this process was considerably simplified. The equatorial ports were made integral to the cavity body, facilitated by the spherical profile, the end caps were welded into the body before plating and all cooling channels were finished and water fittings grown in with one plating operation. (There were no HOM ports but the same process might be applied if there were). This process required some development to get the placement of electrodes right for uniform plating coverage but if more than a few cavities are to be produced then this cost would be more than offset by the savings from the eliminated parts and operations.

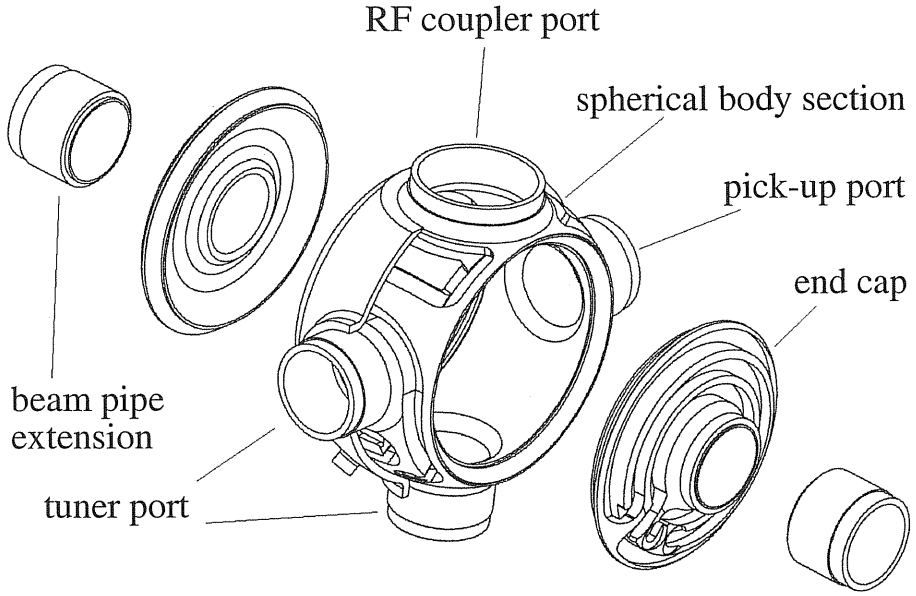

Figure 44 ALS third harmonic cavity assembly.

The proposed construction process for the NLC RF cavities is based on the fabrication of 2 major components, the cavity lid and body, as shown in figure 45. They are made from C10100 alloy copper forgings sized to incorporate the finished surface geometry of each component. When developed by a series of machining processes, both represent monolithic structures with completely developed internal and external features. The 2 components are then joined together by electron beam welding to form a single

cavity unit, and are then ready to accept the port flanging by the same weld process. The forged and cold-worked assembly presents a robust copper structure without any reduction in strength from brazing or annealing.

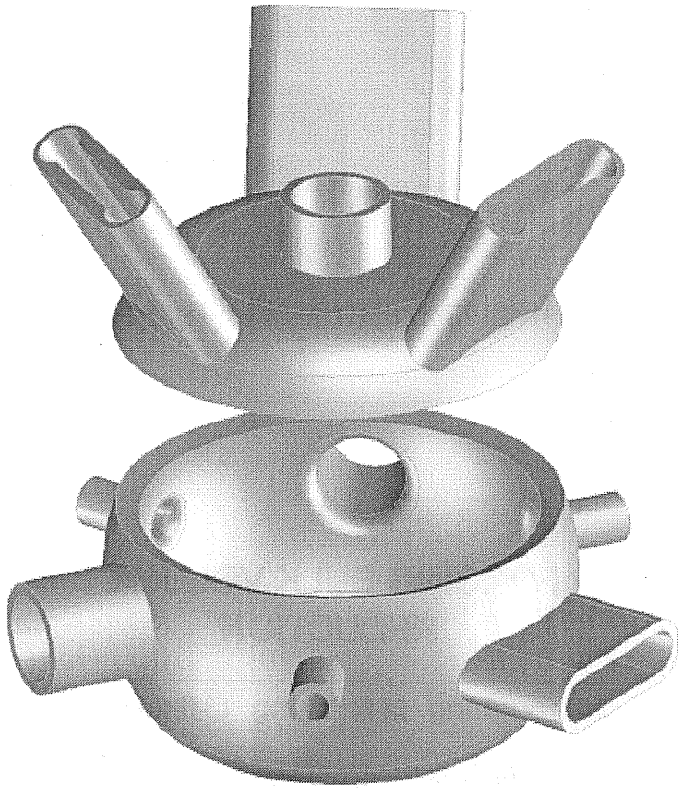

Figure 45. Two main components of proposed NLC cavity.

This construction technique is a departure from the PEP-II fabrication approach. By reducing the number of subassemblies and weld attachments, the construction costs should be greatly reduced in the NLC design. As a point of reference, the number of weld and hydrogen braze processes are reduced from approximately 42 major elements on PEP-II to 24 on the NLC design. Of these 24, 11 are supplied by a commercial flange manufacturer as part of the port flanging procurement.

3.1 General fabrication approach

The monolithic approach using forgings does not come without associated costs, however; raw material costs are greater, and a significant amount of surplus material must be machined away. Figures 46 and 47 represent the rough machined geometry of the forged material prior to finishing

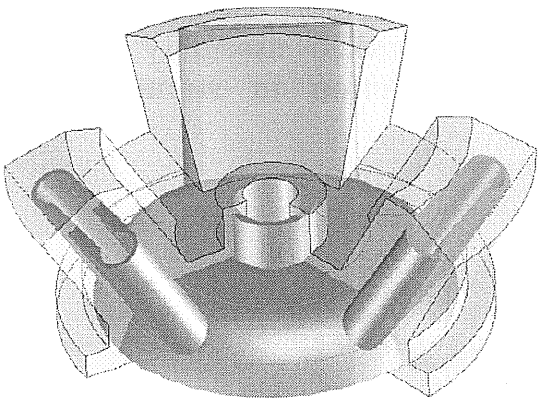

Figure 46. "Lid" forging.

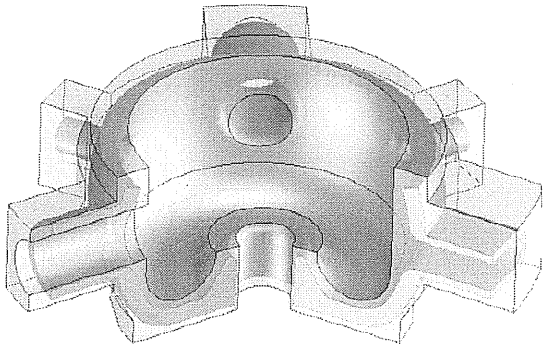

Figure 47. "Body" forging.

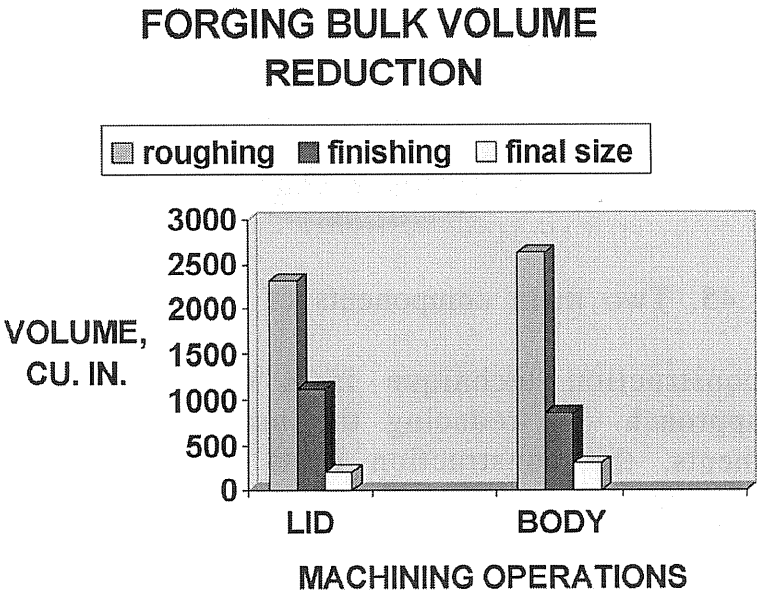

Figure 48. Component volume at various stages of manufacture.

Figure 48 shows the amount of stock removal that can be achieved by rough machining using conventional CNC lathe and milling processes. Rough machining reduces the lid volume by approximately 50% and the body volume is reduced by approximately 65%. The robust geometry of the forged components present rigid shapes that tolerate high cutting rates and stock

removal without the necessity of high dimensional tolerances. Cost estimates are being developed for these processes with the idea of minimizing them through the use of CAD/CAM, supplying 3D CAD models where possible for rough machining, and minimizing any costly drawing process for these roughing steps. Final machining and material reduction amounts are also shown in figure 48, which reduce the rough machined volume by approximately 80% and 65% respectively. This process involves conventional CNC lathe machining as well as 5-axis milling. The 5- axis milling will be used for regions around the port extensions and for the water cooling grooves cut around the exterior cavity surface. The internal cavity geometry will also follow the technique of using 3D models to drive the cutting path on the surfaces, coupled with the use of a plunge EDM process to radius the internal edges of the ports where it is not practical to do so through conventional machining techniques.

A 3D CAD model, figure 49, provided the basis for generating the plunge EDM electrode shape, and it was furnished to an industrial vendor for fabrication. A prototype of an internal port radius for the HOM port configuration was produced by the plunge EDM process, and quantified for surface finish, geometry compliance and vacuum compatibility; it is shown in figure 50. The finished part has been tested and deemed acceptable from a vacuum compatibility standpoint. Developing the prototype has also proved to be beneficial in determining cutting times, electrode material choice, and identifying pre-shaping techniques to ameliorate electrode wear. This will help to minimize the time and expense required for repeated reshaping of the electrode.

After the surface geometry of both the lid and body are fully developed, cooling channels are machined in the outer surface using 5-axis CNC milling. The technique used is similar to that of the PEP-II approach; the 2 components are machined with multiple path cooling channels, to be covered by electroplating at a later stage of the construction.

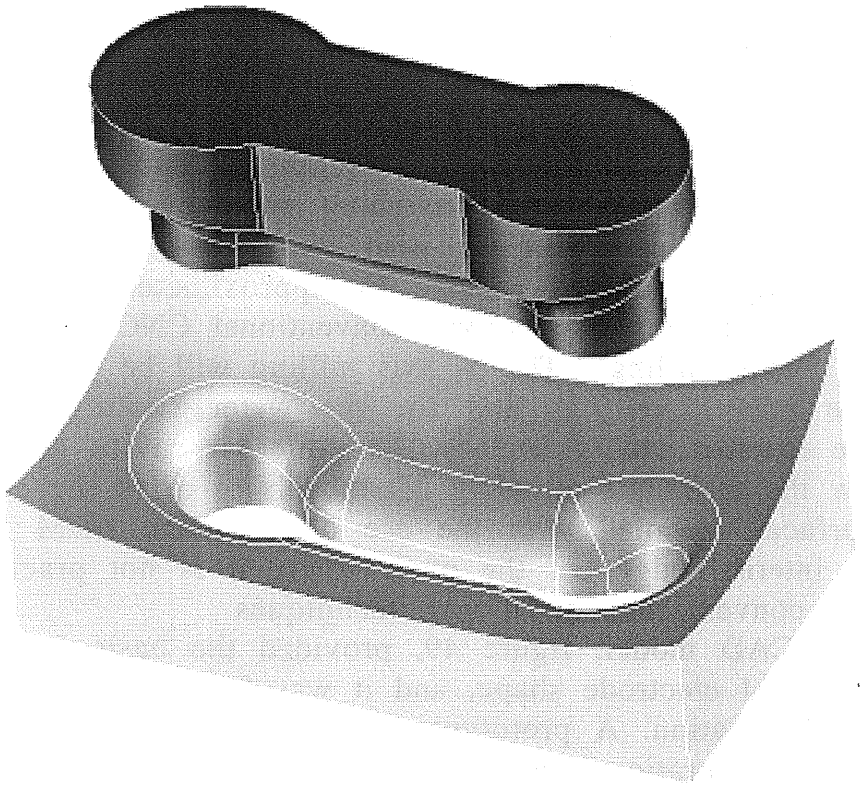

Figure 49. CAD model of EDM sample with graphite electrode.

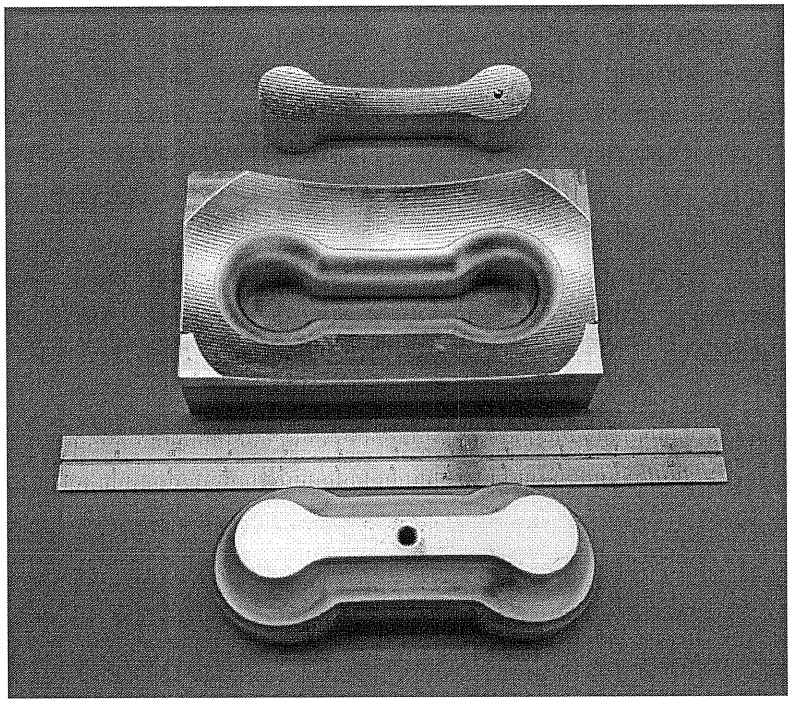

Figure 50. EDM sample with tellurium copper electrode (bottom) and wire burnout (top).

3.2 Assembly

The first assembly step is joining the cavity lid and body by electron beam welding to form one part; there is clear access for the welder on the outside of the cavity between the ports. The joint is finished with a wash weld on the inside through the opposite beam port opening, which leaves a smooth surface suitable for RF. Following the body assembly, the cooling grooves are filled with wax, and a covering coat of electroplated copper approximately 10 mm thick is applied to all the regions of the body where the cooling grooves are placed. After plating, the wax is flushed out of the cooling passages; proof pressure tests validate the plating adhesion. The port flanges are then attached to the port extensions. The flanges are selected to be commercial knife-edge-seal units, chosen as much as possible to be of similar size. Each flange will be supplied by a vendor with a brazed C10100 copper insert, and the insert will be subsequently machined to fit the port extension geometry. The port extensions will have machined registration surfaces to accept the flanges and be self-fixturing for welding. As an alternative to a brazed insert approach, an explosion bonded flange of similar geometry is being investigated. This approach has an advantage over brazed-insert flanges as there is no annealed copper in the flange; in fact, the copper is extensively cold worked through the bonding process and provides a weld interface at the port extension that is as hard as the cavity body, and more resistant to distortion from any bending moments that might be inadvertently applied during assembly.

Welds will be made with an electron beam weld at the sealing surface of each flange, a region for welding that creates no access problem for the electron beam. A detail of the flange assembly is shown in figure 51, showing the port extension, knife edge flange and braze insert.

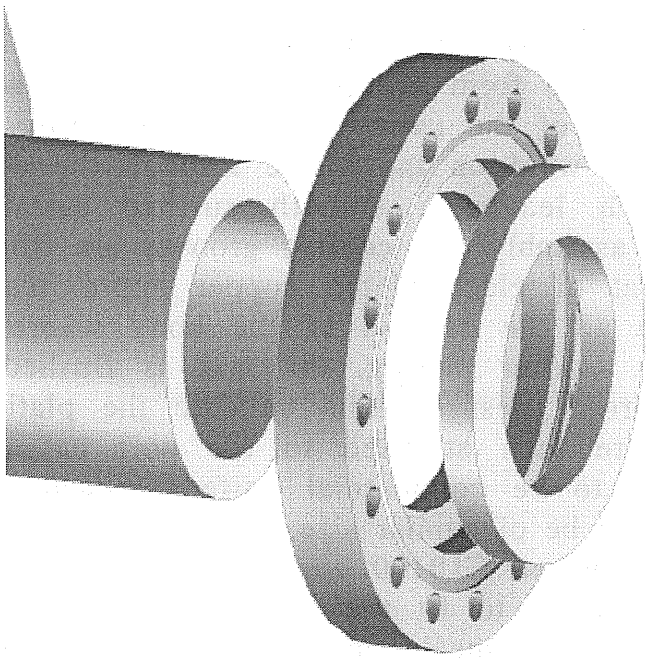

Figure 51. Flange assembly with insert.

3.3 Mounting and installation

The RF cavity geometry is shaped such that there are flat surfaces at each beam port end. These surfaces are ideal for mounting and installation, and the cavity assembly can be kinematically mounted without undue complexity, while allowing for thermal growth. Holes tapped into each end surface before electroplating may accept extension studs that are installed and captured during the electroplating process. These studs attach to spherical bearings that are incorporated into 2 support brackets, one being fully constrained with 2 support points, and the other having 1 support with 1 degree of freedom. The single support acts as a flexure to accommodate thermal growth along the beam axis. The spherical bearings isolate the cavity from any applied bending moments, and the extension studs are anchored in the body material and further supported by the electroplated copper surrounding them. Similar attachments would provide for lifting and handling during removal or installation. Figure 52 shows the complete assembly in an exploded view. Figure 53 shows a schematic mounting of the cavity.

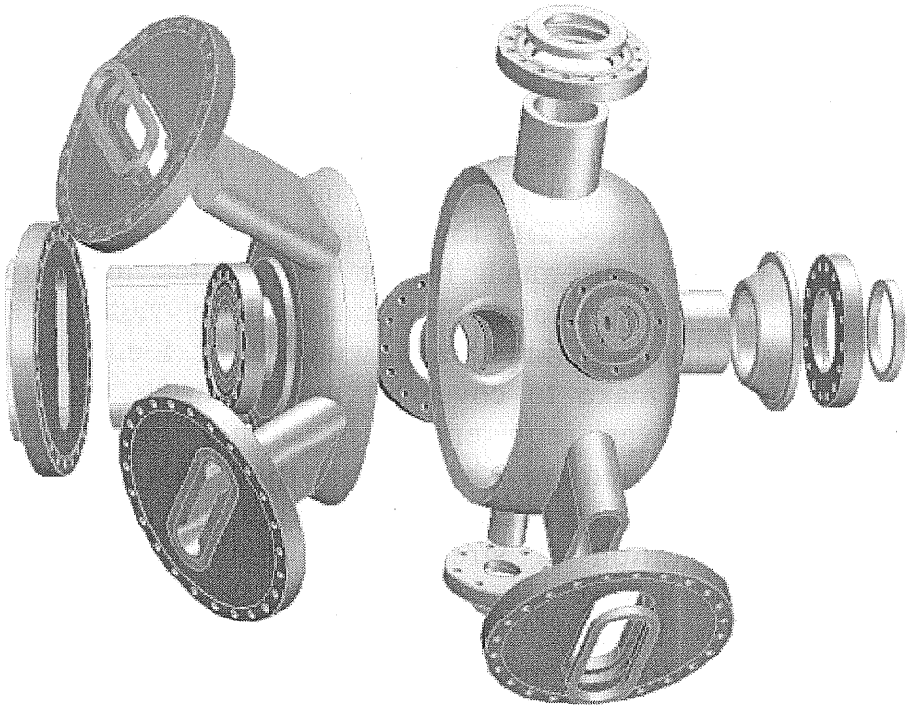

Figure 52. Cavity assembly, exploded view.

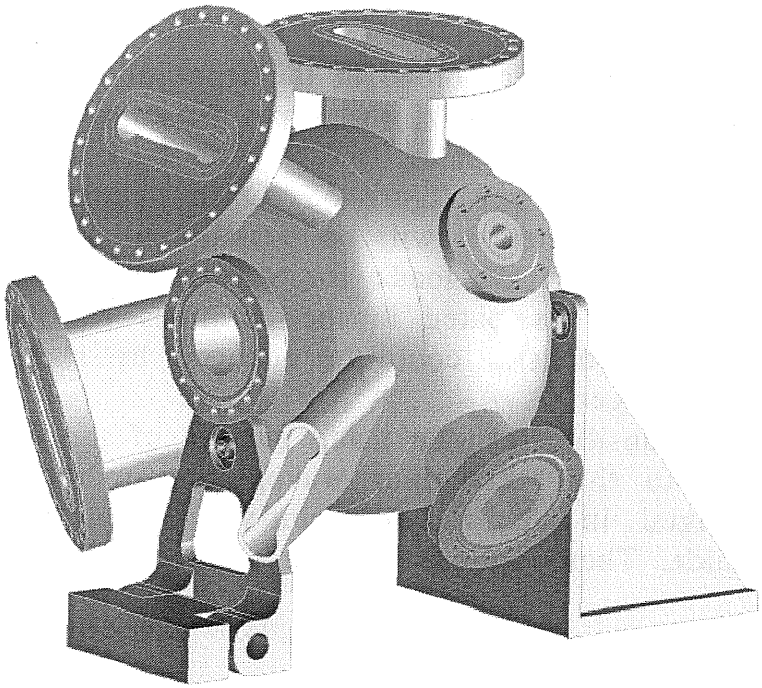

Figure 53. RF cavity mounting scheme

4. HOM waveguides and loads

It is proposed to use similar HOM loads to those used in PEP-II [17], though smaller. These consist of tapered arrays of RF absorbing ceramic blocks (SiC + 40% AlN), at the end of an evacuated waveguide, see figure 54. The waveguide cut-off frequency is about 900 MHz, sufficiently above the cavity fundamental to give good rejection in a reasonable length (<1m), and the tiles are arranged to give a good match (VSWR < 2:1) for all of the HOMs below cut off. The loads continue to work to much higher frequencies to absorb power above cut off. Having the absorbing material in vacuum eliminates the need for a high-power broadband window or feedthrough, which would be difficult to make to cover all modes up to the small beam pipe cutoff. The power requirement is highly dependent on the pattern of bunches filled in the rings; this will be investigated further. For PEP-II the tiles were brazed to an array of small copper posts to allow relaxation of stresses on cool down from brazing, which proved to be a very successful design (no tiles or loads were lost in almost 100 brazes). An active braze alloy was used that bonded to the AlN without metalization being necessary.

Figure 55 shows a simple MAFIA model of a scaled version of the PEP-II type load with tapered ceramic absorbers, which was used for preliminary studies. A more detailed model will be used for future investigations. Figure 56 shows a snapshot of the MAFIA simulation for an incoming wave at 1 GHz in the TE_{01} waveguide mode. The VSWR at this frequency is less than the 2:1 requirement and most of the energy is absorbed at the front of the load. Figure 57 shows the same view at 3 GHz; the wave penetrates further into the load and the energy is dissipated towards the back of the tapers but the VSWR is still good, see figure 58. Once detailed studies of the cavity modes are completed it will be possible to estimate the power spectrum reaching the HOM loads for various beam filling patterns and the power to be dissipated in the ceramics can be checked. If necessary the power density could be reduced by shaping the loads or making them longer.

A gradual transition can be made outside of the cavity from the dumbbell shape to the rectangular waveguide, or the load material could be arranged in the flat (capacitive) region of a dumbbell section waveguide. These options will be studied in more detail.

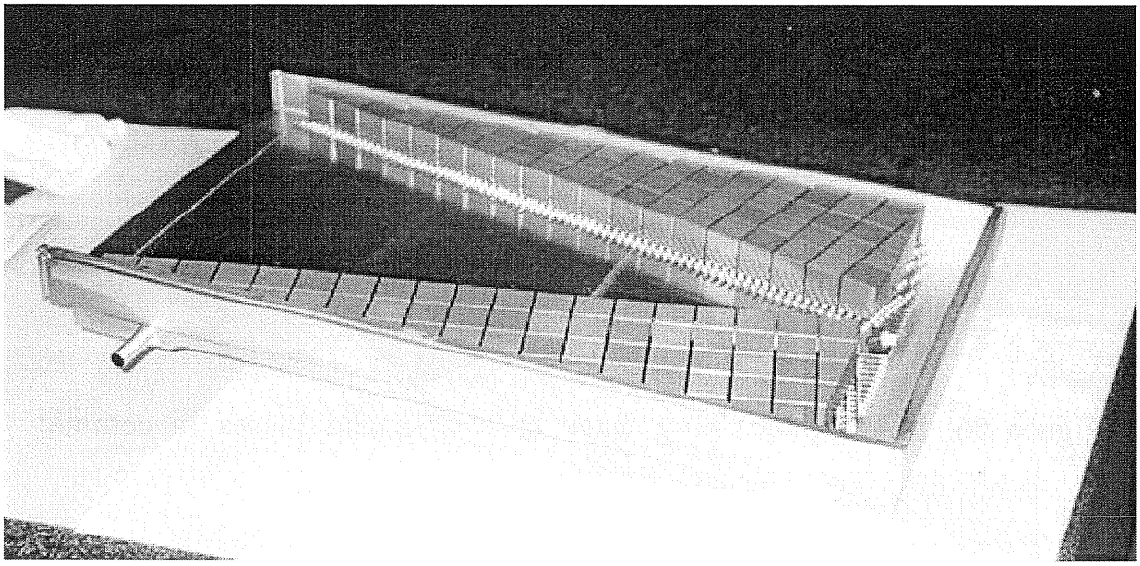

Figure 54. PEP-II HOM load absorbing tile array.

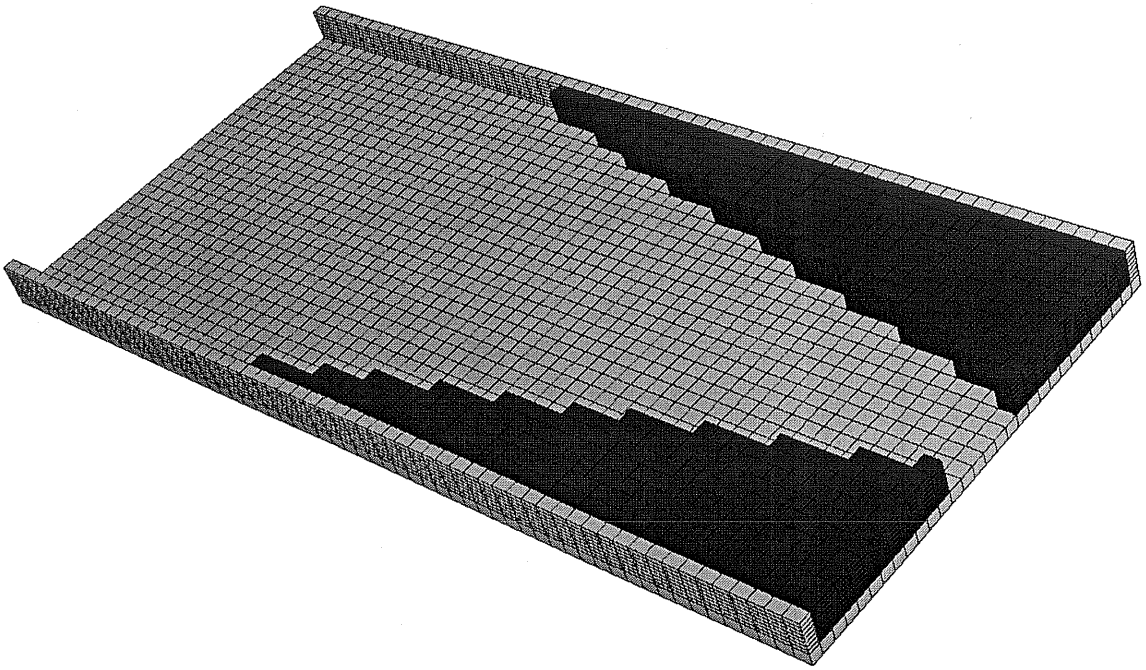

Figure 55. MAFIA model of scaled PEP-II type HOM load.

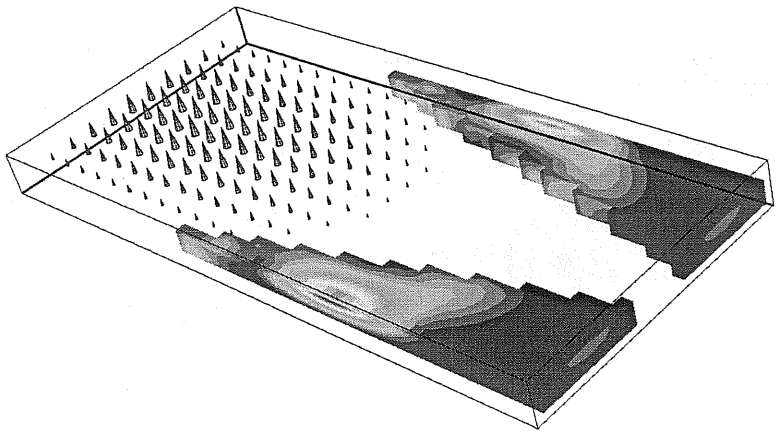

Figure 56. MAFIA incoming wave at 1 GHz and losses in ceramic.

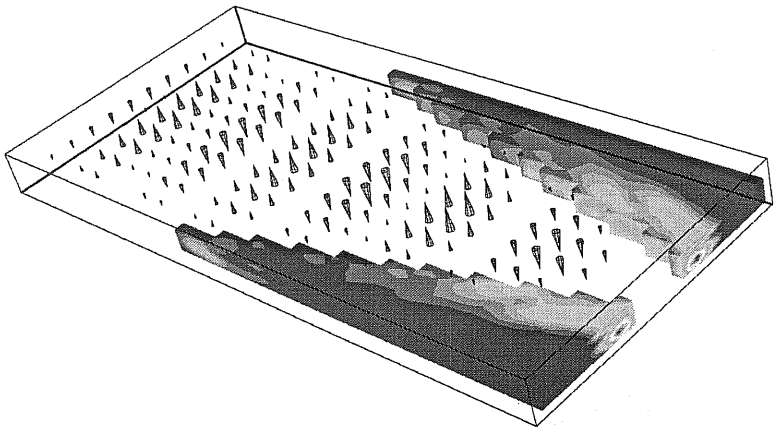

Figure 57. MAFIA incoming wave at 3 GHz and losses in ceramic.

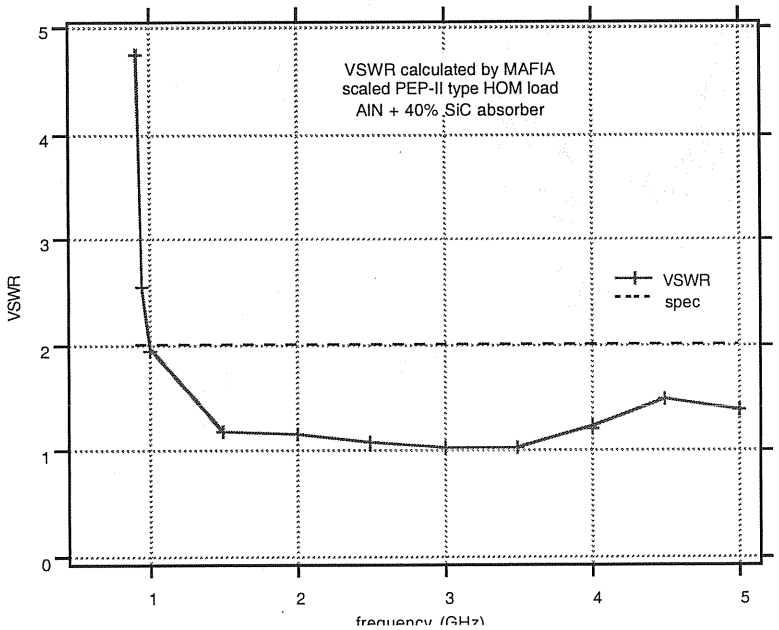

Figure 58. VSWR of scaled PEP-II type HOM load.

5. Window & coupler

The NLC damping rings will have high circulating beam current There will be a continual demand for RF power to compensate power loss to synchrotron radiation and HOMs in addition to the cavity losses. The RF windows and couplers must therefore be able to deliver very high power continuously, but also withstand large beam loading transients. The window must be broad-band to enable fast feedback systems to operate for reduction of gap transients, if required. It is proposed to use a scaled version of the PEP-II disk RF window [18], which is designed to be robust and withstand high power throughput continuously. It will be placed in a detuned-short position in the waveguide to minimize the effect of transient fields.

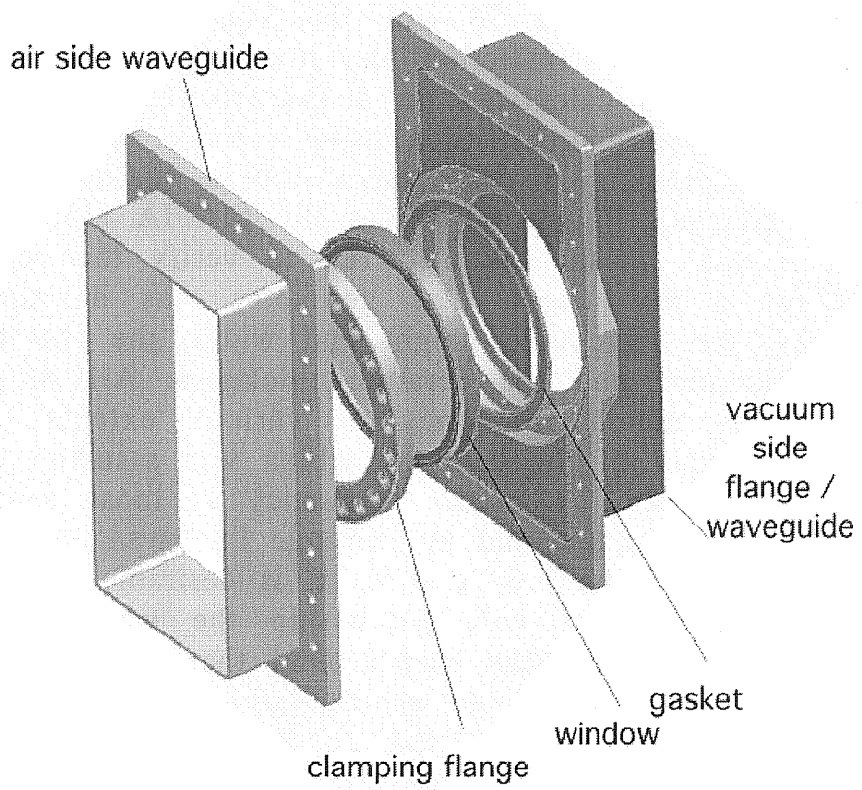

Figure 59. proposed waveguide window assembly.

The waveguide chosen for the damping ring RF system is WR1500. For simplicity it is proposed to use the same waveguide size

for both the air side and vacuum side of the window, which requires some adjustment of the dimensions.

The window fabrication will follow the same process developed for PEP-II, resulting in rugged design with the ceramic pre-stressed in compression by a strong stainless steel ring, which also contains the cooling channel. This pre-stress is designed to compensate the tensile stresses that would otherwise be induced in the ceramic due to heating by RF losses. The coupling beta needed for the damping rings (5.8) is higher than for PEP-II (~4) which will require adjustment of the cavity coupling port dimensions. The coupling box will also contain a load to absorb HOM power coming out through the coupling port above the drive frequency and prevent resonances building up between the coupling port and the window. Figure 59 shows the proposed window assembly.

5.1 Window analysis in MAFIA

The window design has been studied using MAFIA, employing the time domain module T3 with the S-parameter macro which can calculate steady state reflection and transmission coefficients, VSWR etc. These can be calculated on a frequency by frequency basis or with a broad-band approximation using a pulse excitation. Because of the inherent symmetry in the design only a quarter of the geometry need be modeled. Figure 60 shows the MAFIA model used for the studies. A finer mesh was also run to verify the accuracy of the results for a few cases. The geometry was defined by a few parameters; the waveguide height and width, the iris thickness, the window diameter and the ceramic thickness. All of these factors influence the match frequency to various extents, as does the dielectric constant of the ceramic, which was assumed to be 9.6 for these simulations. The match frequency is most sensitive to the diameter of the window and the ceramic thickness and less so to the iris thickness. For the lowest stress it is desirable to use the largest diameter window that will fit within the waveguide, while the dimensions of the stainless ring around the ceramic were scaled in proportion to keep the same aspect ratio as the successful PEP-II design. A size was chosen that neatly fits in the waveguide and allows a standard (10") circular "Conflat" knife edge geometry to be used. Once the diameter of the ceramic is chosen the frequency can be tuned by adjusting the thickness. This design has been chosen to allow the frequency to be set at 714 MHz for NLC, figure 61. The final ceramic thickness will be determined by measurements of actual ceramics in a cold-test fixture.

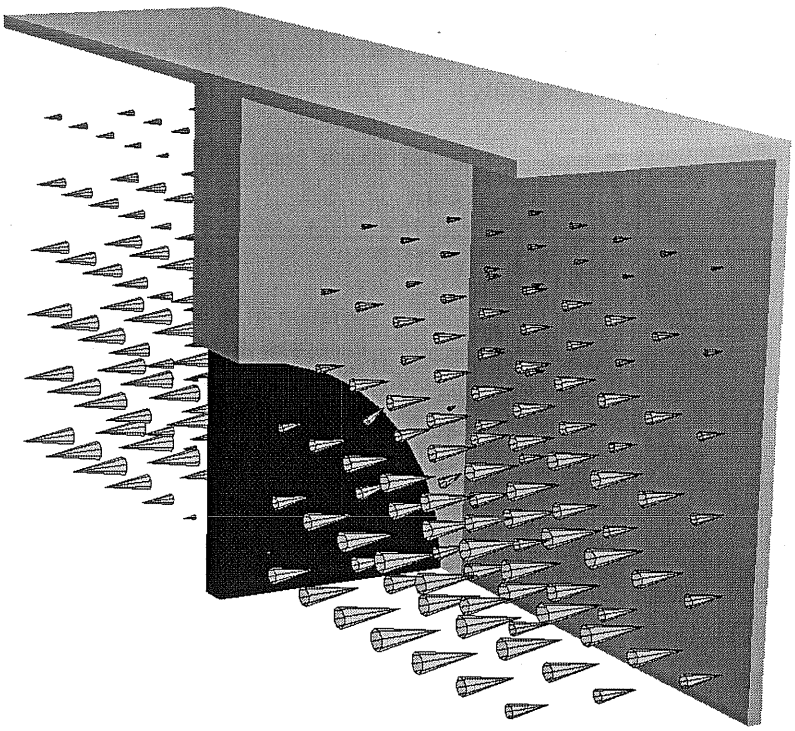

Figure 60 Window with normal TM_{01} waveguide mode propagating.

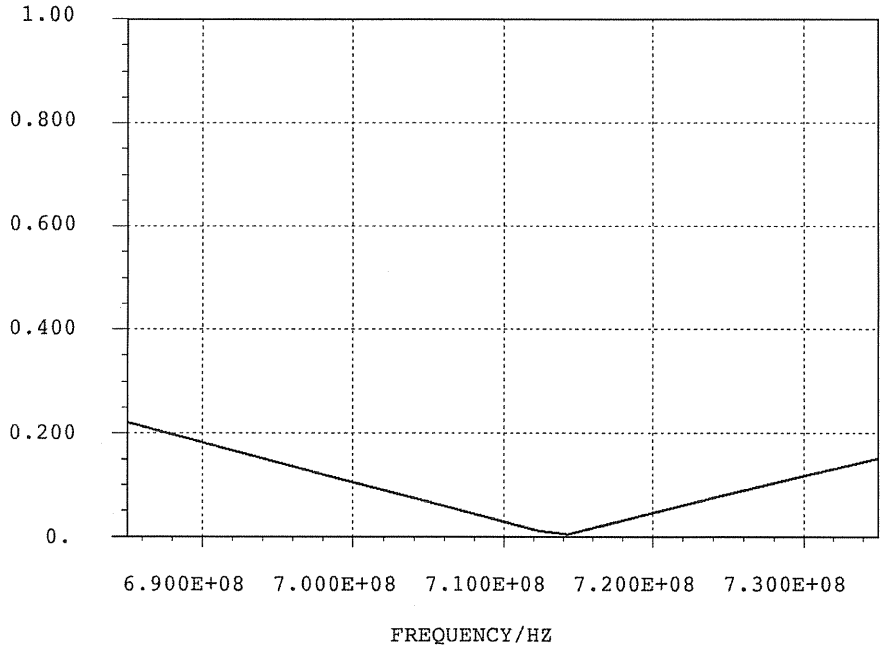

Figure 61. S_{11} of waveguide window.

Figure 62 shows how the frequency varies with ceramic thickness and iris length for the chosen geometry. To allow for manufacturing tolerances the window match frequency can be fine tuned by trimming the thickness of the flange when the knife edge is

cut, the last step of the manufacturing sequence. Brazed assemblies will be made slightly oversize on the flange thickness and will be cut to final size after the frequency is measured in the cold-test fixture.

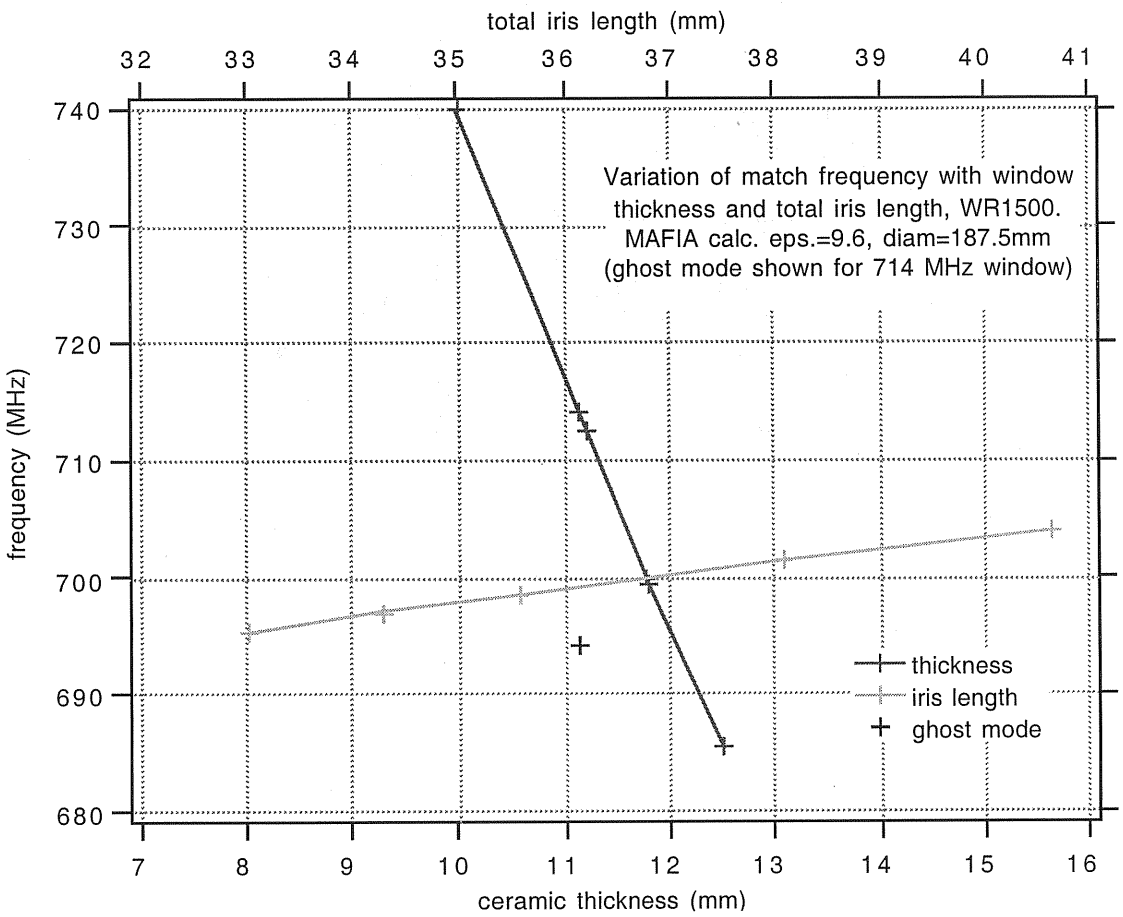

Figure 62. Tuning of window assembly.

The ceramic disk window in a waveguide can be thought of as a capacitively loaded iris in which the magnitude of the capacitive reactance equals that of the inductive part at the match frequency. This geometry can have other resonant modes, including the so-called "ghost mode" in which the electric and magnetic fields are orthogonal to the transmission mode and consequently are not able to propagate away in the waveguide. Figure 63 shows the electric field distribution of the ghost mode in the window calculated by a frequency domain simulation in MAFIA. It is important that the waveguides in the MAFIA model be long enough that the waveguide termination does not influence the ghost mode frequency, so the model was run with increasingly long waveguides until the resonant frequency did not change significantly (1m long waveguides proved sufficient). It is important to make sure that the ghost mode is

outside of the operating band of the RF system, otherwise power from the klystron or beam-induced power from the cavities could excite this mode causing heating of the ceramic. Figure 62 shows the ghost mode frequency for the 714 MHz geometry, which is safely outside of the operating band.

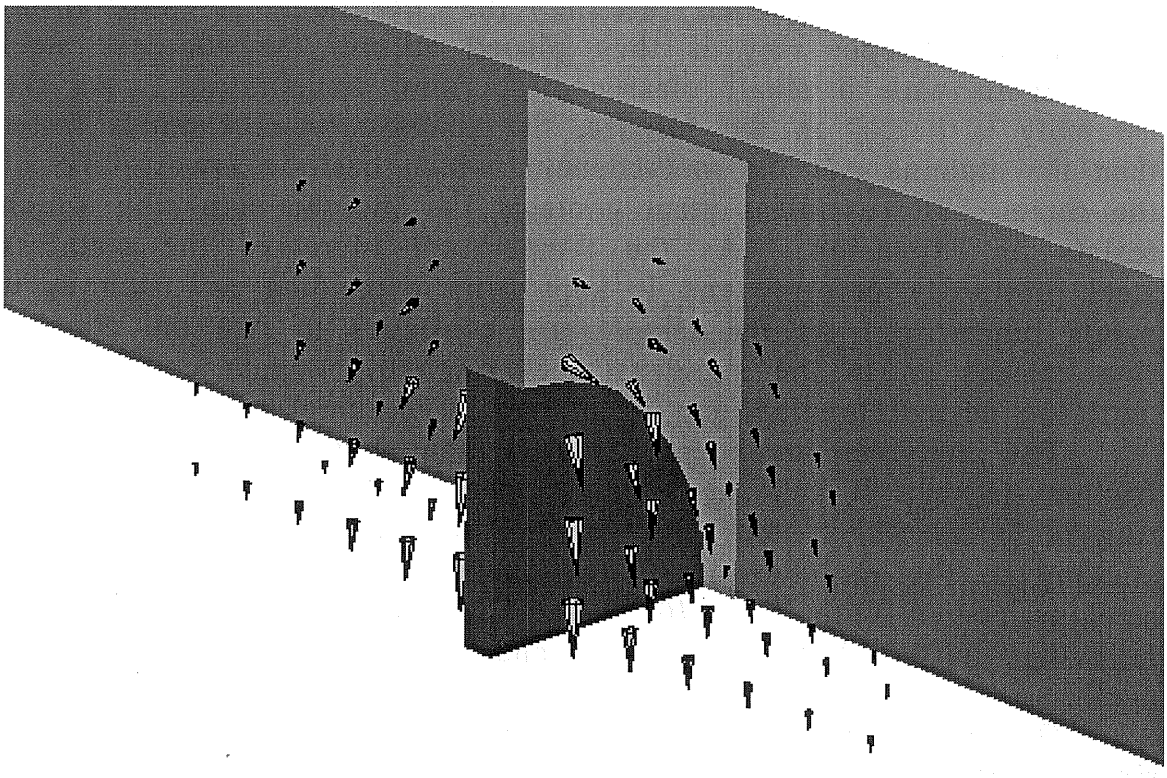

Figure 63. Electric field of ghost mode in window.

5.2 Window analysis in ANSYS

In service this window could see a temperature rise of up to 70°C due to RF losses in the ceramic and coating, multipactoring etc., which could cause the window to crack under thermal expansion. In order to solve this problem for the PEP-II B-Factory, a procedure was developed for creating a vacuum tight alumina window that is under compression under all operating conditions [19].

The method involves brazing the alumina window to a stainless steel cooling ring at high temperature. Since a small gap is required at the brazing temperature to promote braze flowing by capillary action, and the stainless steel has a higher coefficient of thermal expansion (CTE) than alumina, the stainless steel ring will contract more than the ceramic during cooling and place the alumina disk

under compression. Conventionally this same difference in CTE would necessitate starting with a stainless steel ring which is smaller than the alumina window at room temperature. This would make assembly in the brazing furnace difficult.

The solution is to begin with a stainless steel ring which is slightly larger than the alumina window at room temperature, and can therefore be placed around the ceramic. A substantial molybdenum keeper ring is then placed around the stainless steel ring, again with a small clearance at room temperature. As the assembly is heated in the furnace, the stainless steel expands faster than the alumina and the molybdenum, which has the lowest CTE of the three. The stainless steel contacts the molybdenum ring which resists its expansion. As the temperature increases the stainless steel plastically deforms and is kept from expanding as much as it would otherwise. As the temperature continues to rise the alumina ring catches up to the stainless steel ring/molybdenum combination, until the desired brazing gap is attained at brazing temperature.

The molybdenum keeper ring is coated with TiN to reduce friction between it and the stainless steel ring. The stainless steel ring is "greened" (coated with Cr_2O_3), in a furnace to keep it from sticking to the molybdenum. The inner diameter of the stainless steel is coated with a 0.040" layer of copper to act as a stress relieving "buffer" layer between it and the alumina on the cooling cycle.

On cool down from the braze temperature the stainless steel ring contracts more than the Alumina creating the desired compressive pre-stress in the ceramic.

The key to this operation is starting with the correct initial clearances and sizes of the stainless steel and molybdenum rings. The size of the alumina window is determined by the RF frequency and the waveguide dimensions. For the PEP-II window an ANSYS FEA model was used and numerous experiments were performed to find the correct clearances and sizes for the molybdenum and the stainless steel rings. The PEP-II window was approximately 1.3 times the diameter of that proposed for the NLC damping ring cavities, however the stainless steel ring size and the initial clearances do not scale exactly with the window and must be reevaluated.

In order to adapt the design for the NLC project, the alumina was sized appropriately for the RF requirements and the molybdenum keeper ring was roughly sized by scaling the PEP-II ring. Using these inputs another ANSYS model was generated and the correct initial size and clearances were determined. The ANSYS

model will be experimentally checked by running a stainless steel and molybdenum ring of the predicted size through a furnace cycle before the first window braze is attempted. Pending the results of this ring test the parameters of the ANSYS model will be fine tuned and the final dimensions for the rings and the room temperature clearances will be determined.

The first finite element model has been completed. Initially, room temperature clearances of 0.010" between the alumina and stainless steel and 0.015" between the stainless steel and molybdenum will be used. The ANSYS model was built using 2-D axisymmetric elements. Figure 64 shows a radial slice of the assembly with the alumina window, the copper layer, the stainless steel and the molybdenum.

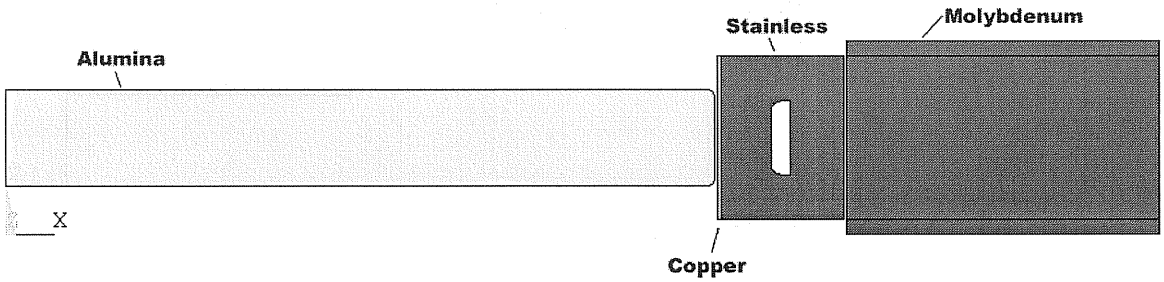

Figure 64. Material configuration for NLC window braze.

Figure 65 shows a close up of the stainless steel cross section at room temperature. The gaps between the alumina and stainless and the stainless and molybdenum can be seen clearly. Contact elements are used in the ANSYS model in the gap between the stainless and the molybdenum to model the friction and sliding between the rings. Figure 66 shows the assembly at the brazing temperature of 1050°C. The 0.003" brazing gap between the stainless steel ring and the alumina window is barely distinguishable at this resolution. Figure 67 shows the Von Mises stress state in the stainless steel ring at brazing temperature. Note the stresses shown (in MPa) are uniformly above 96.6 MPa, the yield point of 316 stainless steel at elevated temperature.

Once the braze is made the temperature is ramped down slowly and the stainless contracts around the ceramic. There is a long hold at constant temperature part way through the cool down which is to allow the copper buffer layer to creep, relieving some of the stresses caused by the axial differential contraction. On cooling to room temperature the stainless steel is in tension and the ceramic is pre-stressed in compression.

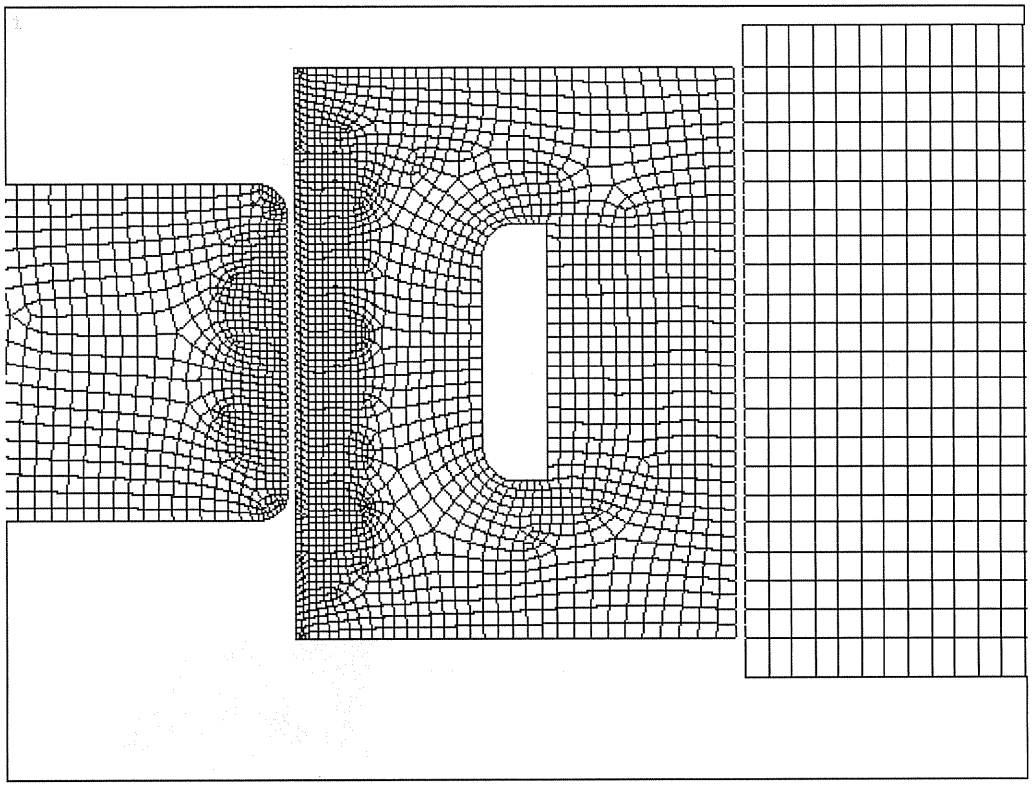

Figure 65. ANSYS model showing FE mesh and clearances between the materials at the start of the cycle.

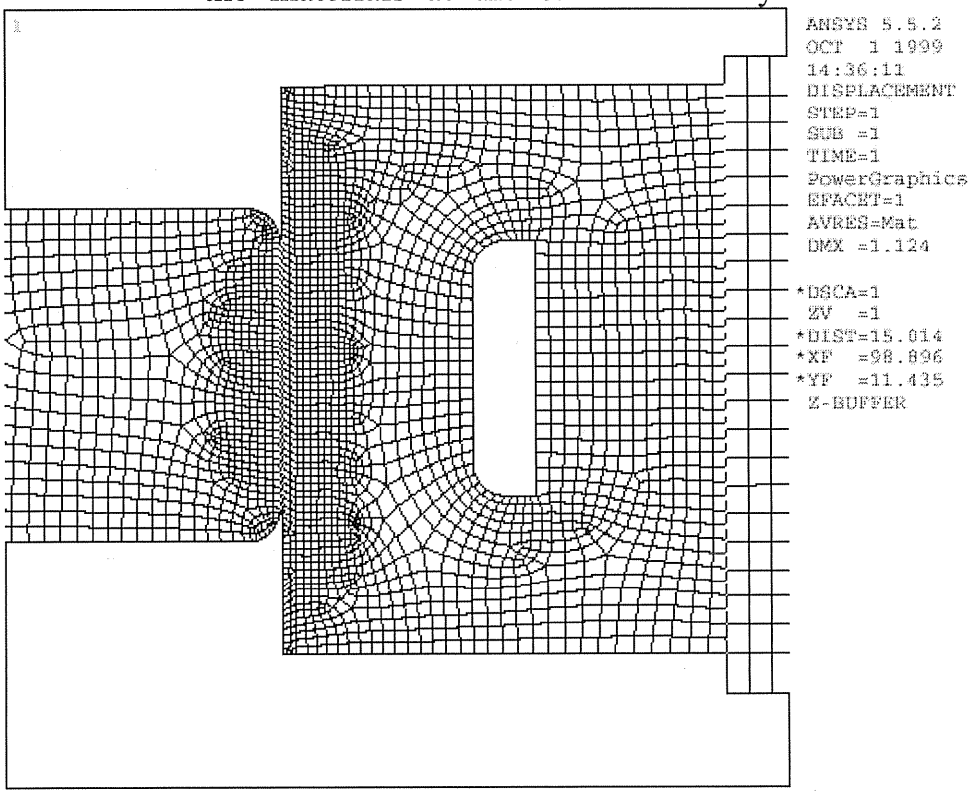

Figure 66. ANSYS model of the distorted geometry at braze temperature.

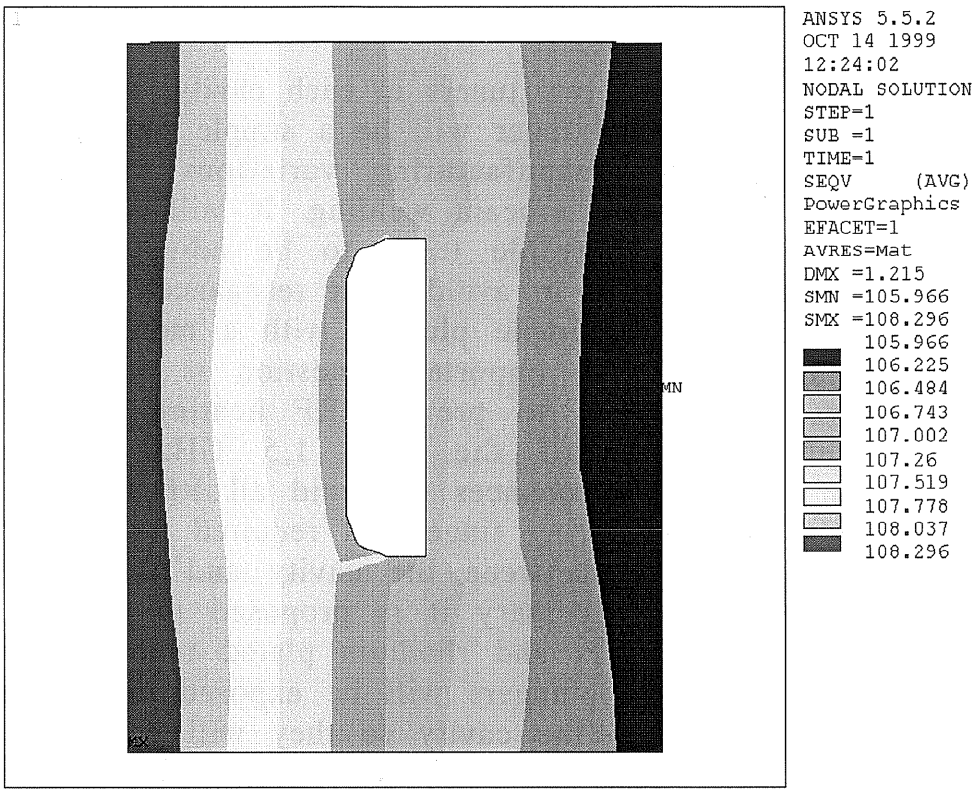

Figure 67. Von Mises stress in the stainless steel ring at brazing temperature.

6. Tuner

It is proposed to use two tuners in each cavity, with one fixed and one movable. The fixed tuner will be a simple plunger and will be used to correct for manufacturing variations such as weld shrinkage in the post-tuning e-beam welding. It will also allow the "home" position of the movable tuner to be adjusted if this is desirable for HOM tuning or to avoid tuner resonances. The movable tuner is proposed to be a simple plunger with a motorized bellows actuator, see figure 68. An important question is whether spring finger contacts are required to prevent RF heating of the tuner bellows. Careful analysis of the ALS 1.5 GHz cavities and arrangement of the tuner resonances to avoid all RF harmonics has allowed operation without spring fingers. If required fingers could be placed in the spacer ring between the cavity and the bellows. If fingers are found to be necessary it is proposed to use the same silver coated Glidcop fingers and rhodium plated tuner combination used in PEP-II. The tuner plungers will be exposed to high surface currents when inserted into the cavity so they will be well cooled. Figure 69 shows a view of the proposed NLC tuner in which the spiral cooling channel is visible.

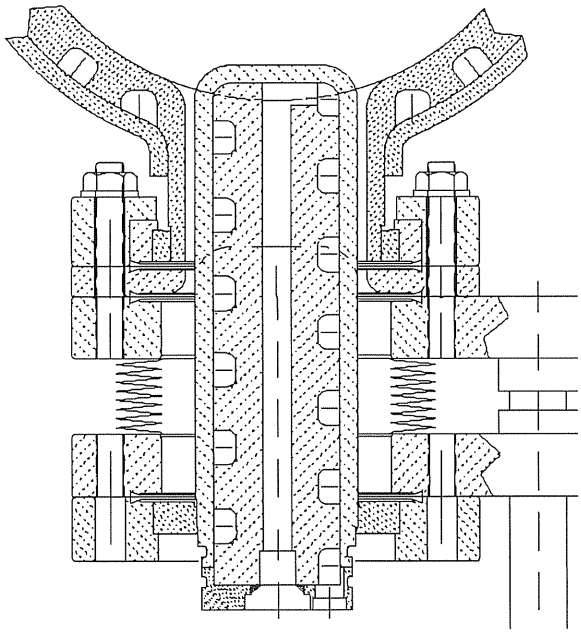

Figure 68. NLC tuner concept based on ALS design.

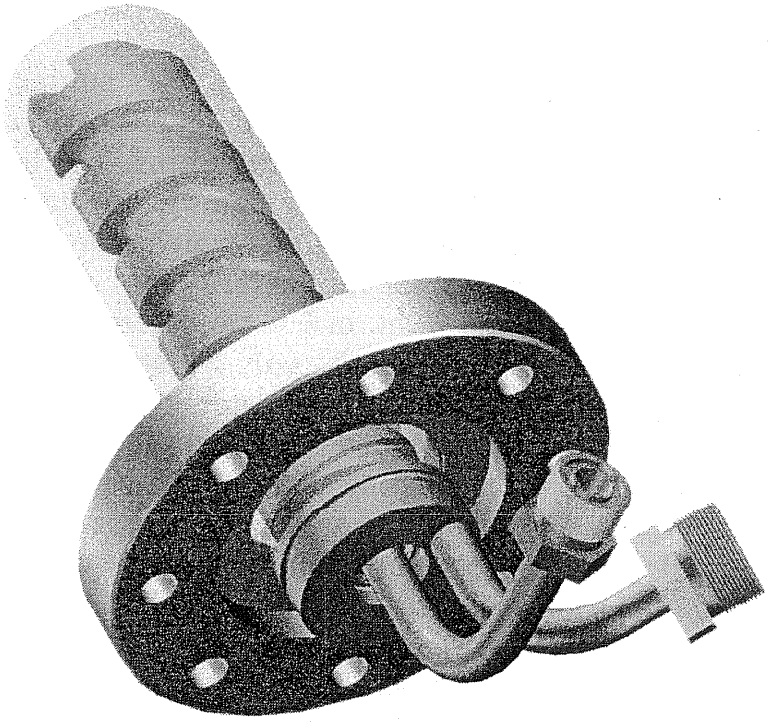

Figure 69. Tuner plunger with spiral cooling channel.

7 Low R/Q options and future work

The damping ring RF systems may be subjected to large transients in the beam loading because of gaps between the bunch trains or partial population of the bunch trains. Such loading will cause transients in the cavity voltage leading to variations in the synchronous phase along the bunch trains, which may in turn lead to problems when the extracted beam enters the subsequent bunch compressor. Work is continuing in order to determine the acceptable phase variation entering the bunch compressor. If the projected excursions in the extracted beam prove not to be acceptable it is possible that they may be reduced by fast feedback or adaptive feedforward systems in the damping rings. For this to be effective unusually wide band klystrons would be needed, possibly with bandwidths of 10 MHz or greater. Consultations with manufacturers are ongoing to determine if this is practically realizable. If the adaptive feedforward system can be implemented simulations show a significant reduction in the phase variation along the bunch trains, although the residual fluctuations are not as well correlated as before. Alternatively it may be possible to reduce the voltage transients in the cavities passively, by adopting a design with a lower R/Q. For times short compared to the cavity time constant the voltage induced by a step change in beam current is approximately proportional to time and the R/Q. For copper structures a lower R/Q will require some increase in the cavity power dissipation and, of course, different shapes will require reevaluation of the HOM damping.

7.1 Low R/Q copper cavities

Preliminary studies have been made of a variety of shapes with progressively lower R/Q, starting with the PEP-II and new NLC nosecone types, through the open "bell" shape, TM_{020} type, spherical shape and spherical shape with a large bore, see figure 70. Table 7 contains a summary of their properties. The PEP-II type and new NLC type have very similar properties. The bell shape is commonly used for superconducting cells because it has low surface fields and reduced tendency to support multipactoring. It is sometimes used for copper cavities when shunt impedance is not at a premium and its lower transverse loss parameter may be useful [20]. In this shape there is a reduction in the R/Q and an improvement in transient amplitude by a factor of 1.6 compared to the baseline PEP-II or NLC designs. The power per cell rises to 57.5 kW and the total power

including beam losses goes up to 761 kW, both of which are reasonable. Another possibility is to use a cavity operating in a higher mode such as the TM_{020} mode, see figure 70d. In this case there is a further reduction to a factor of 2.24 lower than PEP-II, and an increase in power to 66.5 kW. The size of this cell is much larger however, with a diameter more than twice that of the baseline design. The maximum surface power density is about the same as the other designs and is located at the base of the nose cone. HOM damping on this design would be more challenging because the fundamental mode would also need to be damped and multipactor may be a problem in the low-field regions of the cavity.

An even larger reduction can be achieved by using a simple spherical shape, see figure 70e, which has a much lower R/Q, in part because the interaction length is longer than $\lambda/2$ and the transit time factor reduces the effective impedance significantly. The improvement in transient amplitude is about a factor of 4.6 but the power per cell is very high and the total power is very close to the maximum output of a single klystron, leaving little or no margin for waveguide losses or headroom for feedback. In fact, the cavity shunt impedance has dropped to about 1 MΩ, which is really too low for the three cavity installation. If four cavities were used the power per cell would be more manageable at 71.3 kW and the total power would be well within the capability of a single tube at 874 kW. The improvement in transient amplitude is still a factor of 3.44, better than either the bell shape or TM_{020} design. Ultimately the R/Q can be reduced further by increasing the beam pipe radius (f) or lengthening the cavity towards an integer number of wavelengths. This would present engineering challenges in the cooling of the cavity and would require more than one klystron per ring, but a factor of 10 improvement in transient amplitude looks to be possible. Figures 71 through 74 show how the R/Q, Q, Rs and power vary with length of a simple pillbox cavity operating in the fundamental mode (TM_{010}), or higher TM_{020} mode.

Table 7. Parameters of various cavity shapes.

	PEP-II type (714a)	new NLC (714b)	bell (c)	TM_{020} (d)	sphere (e)	sphere (e)	sphere 12.5cm pipe	sphere 12.5cm pipe
number of cells	3	3	3	3	3	4	3	4
R/Q (Ω)	117	118	73.0	52.3	25.5	25.5	9.42	9.42
"improvement"	1.00	0.99	1.60	2.24	4.59	3.44	12.42	9.32
power/cell (kW)	41.4	41.4	57.5	66.5	126.8	71.3	312.5	175.8
approx. total power (kW)	713	713	761	788	969	874	1526	1292
max. Pw (2D) W/cm2	23.0	22.0	25.4	24.5	56.1	31.5	144.0	81.3

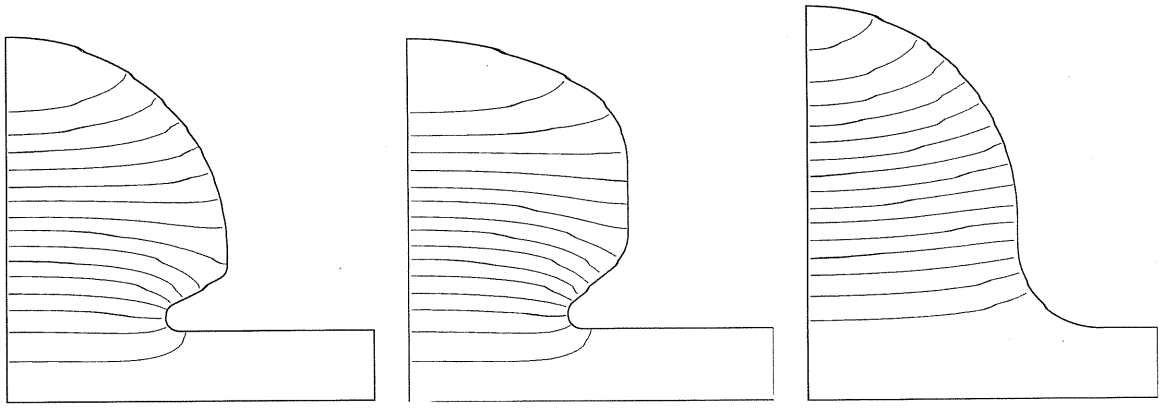

a) PEP-II type b) new NLC type c) "bell" shape

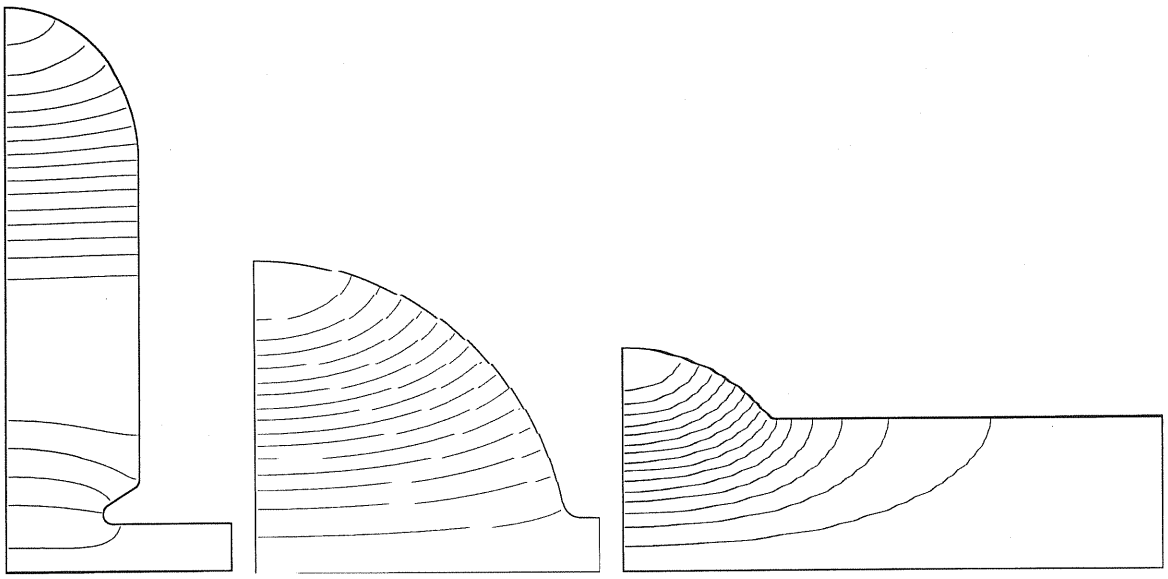

d) TM_{020} e) sphere f) sphere with large bore

Figure 70. Various cavity profiles.

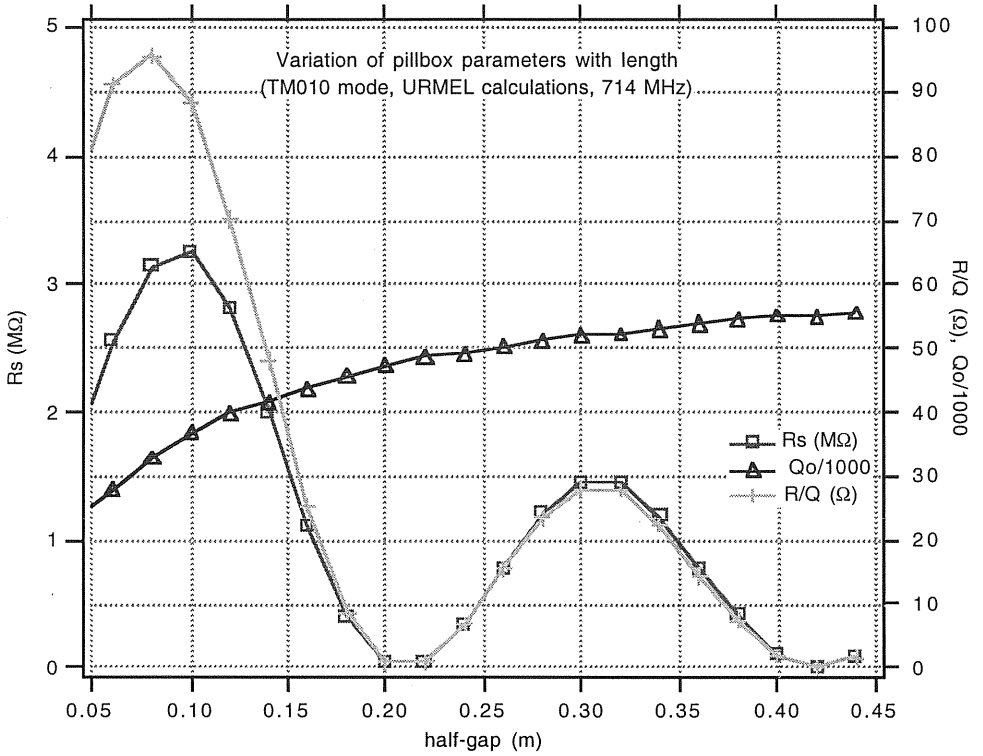

Figure 71. Parameters of TM_{010} mode in pillbox as a function of length.

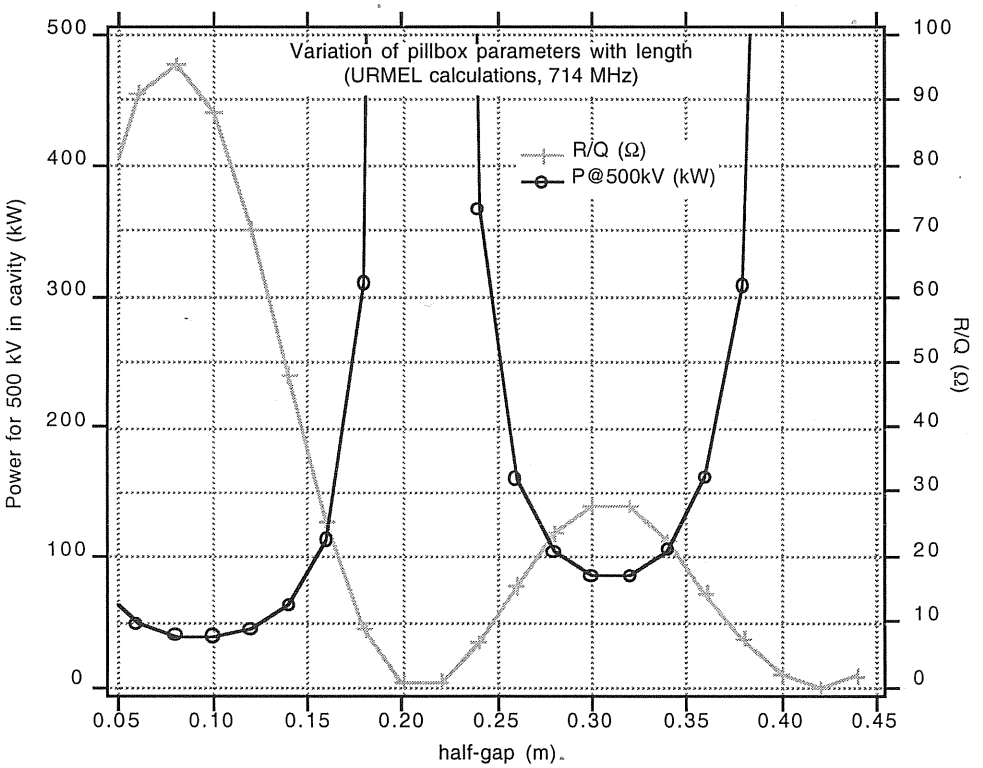

Figure 72. Power required to maintain 500 kV gap voltage as a function of length and R/Q.

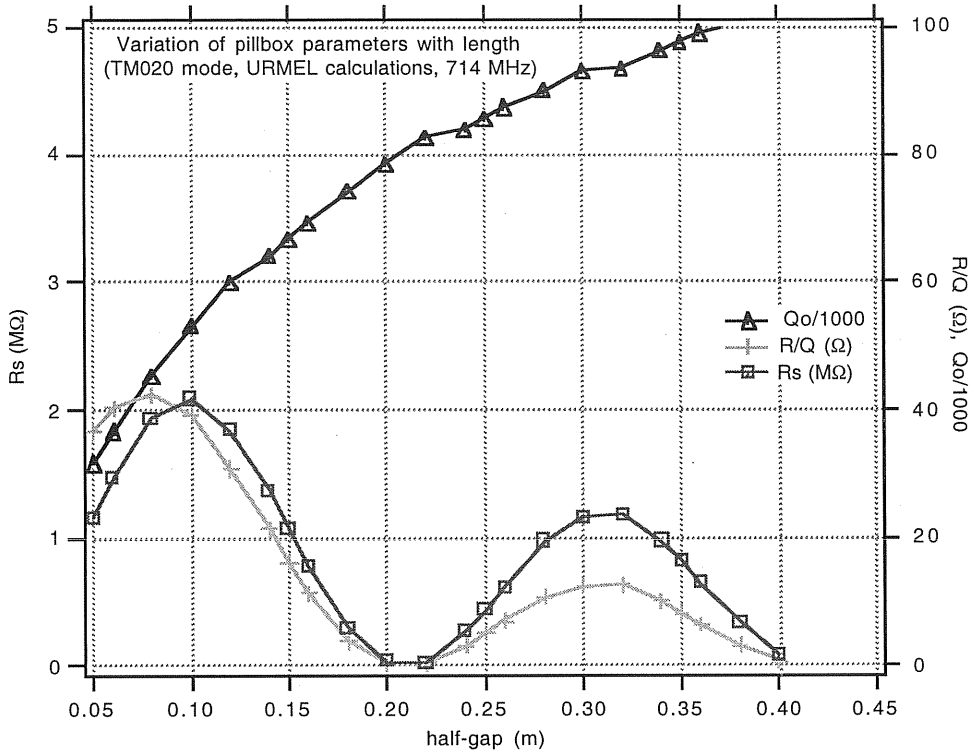

Figure 73. Parameters of TM_{020} mode in pillbox as a function of length .

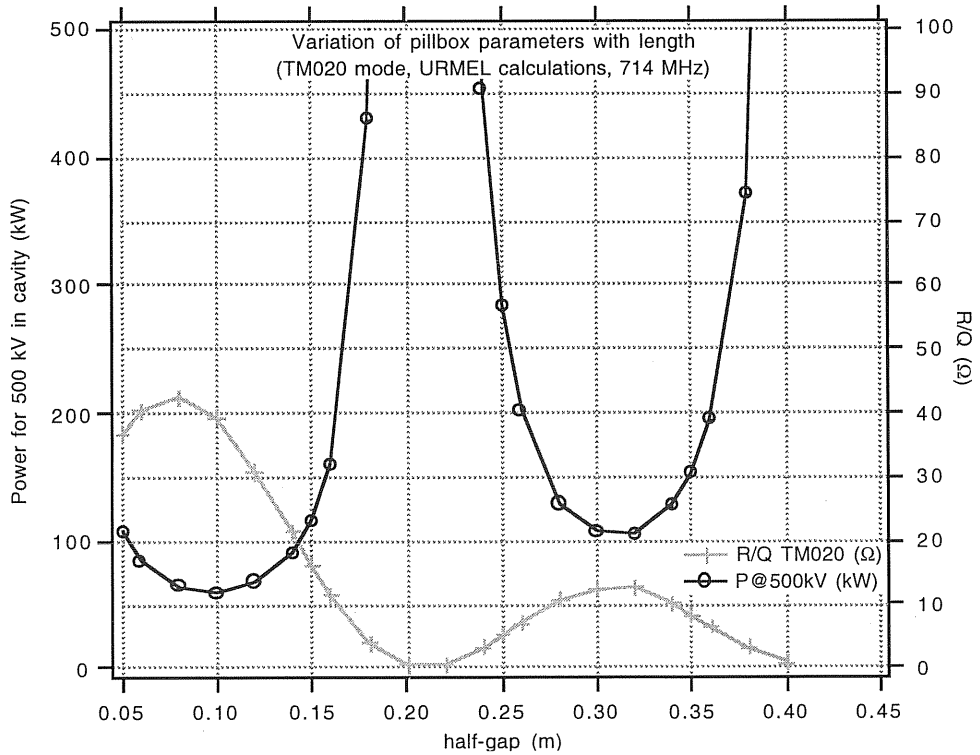

Figure 74. Power required to maintain 500 kV gap voltage as a function of length and R/Q.

7.2 Superconducting option

An obvious solution to the loss of efficiency of the low R/Q designs is to use superconducting cavities. Most superconducting cells have about half the R/Q of the copper nosecone type but a design could be made with elongated cells to operate close to the zero in the transit time factor. Under operating conditions typical cavities can have Q's of ~5 x 10^9 [21], which would allow the R/Q to be about 25 Ω, for 1 W dissipation per cell into the helium (500 kV gap voltage, Rs=1.25 x 10^{11}). This would give a similar improvement in transient voltage to the normal conducting sphere option but without the power penalty. The cryogenic efficiency is typically about a factor of 500 between the helium and room temperature [22], requiring a plant power of about 1.5 kW for three cells (neglecting other losses). Lower R/Q's might be used, at the expense of more powerful cryogenic systems, if the wall currents are acceptable. The cavity design could have a large bore and HOM loads outside the cryostat, similar to the designs used at CESR [23], figures 75 and 76, and KEK [24], figure 77, which would give very good HOM damping and low transverse wakes. The number of cells would probably remain at three because of the high window power that is still required for beam power; however, it may be possible to package more than one cavity in a common cryostat to minimize space requirements and thermal leaks. Estimation of construction and operating costs and reliability budget for such a design will require more investigation.

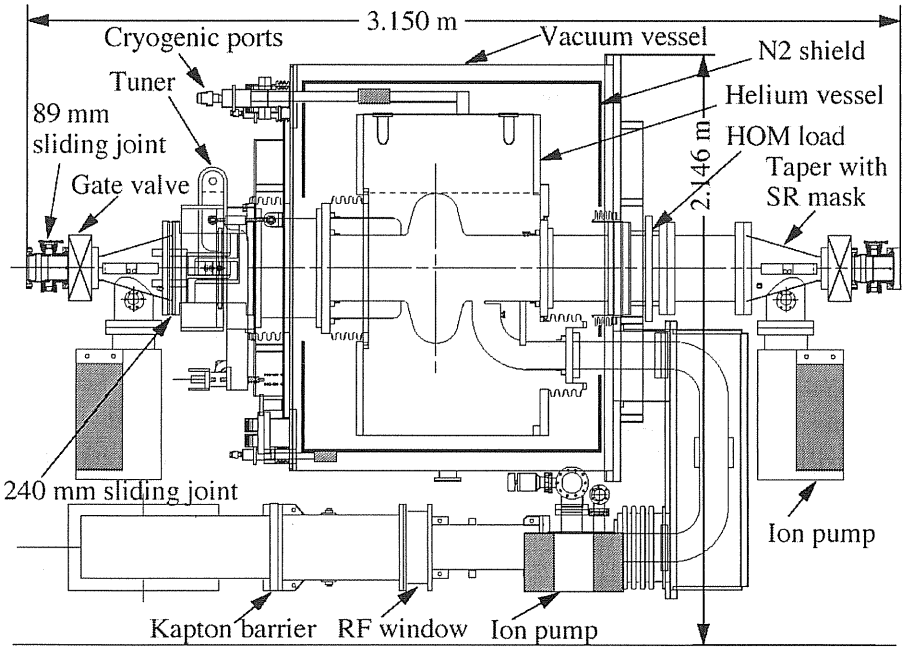

Figure 75. Cornell single cell superconducting cavity module.

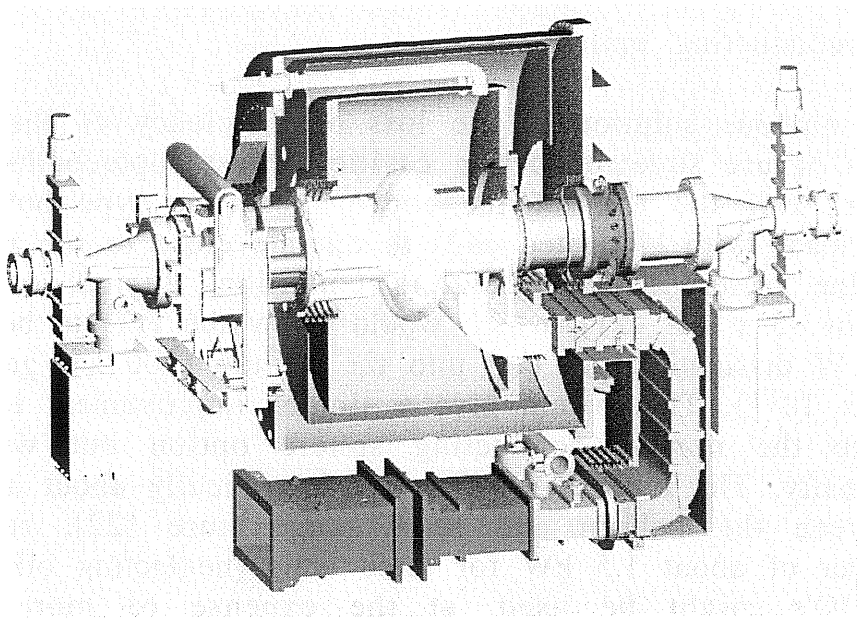

Figure 76. Cornell single cell superconducting cavity module.

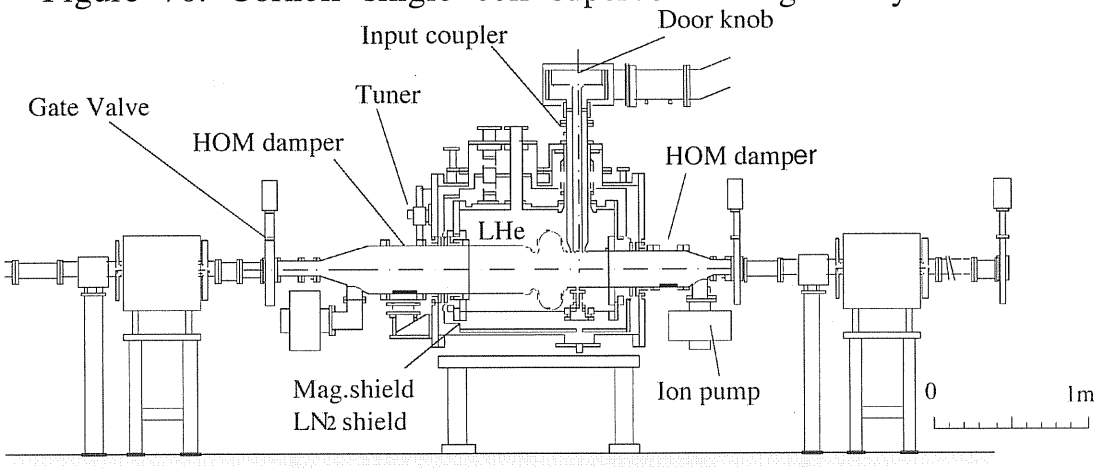

Figure 77. KEK single cell superconducting cavity installation.

7.3 Lower HOM options

As mentioned previously it may be desirable to further reduce the impedance of the remaining HOMs in the cavities, particularly for the pre-damping ring. As a preliminary step to see how this may be achieved several alternative cavity designs have been studied. Figure 78 shows a cavity based on the same body profile as the three waveguide model but having four waveguides, two on each side. One pair is oriented vertically, the other horizontally. This design has the advantage of being symmetrical about the mid plane of the cavity so far as the longitudinal modes are concerned, so there is less tendency for HOMs to re-orient themselves to escape the damping scheme. This gives better overall damping and also allows the offset slot

coupler to be replaced by a simpler circular coupler on the mid-plane. Another circular aperture oriented at 90° to the power coupler catches the last remaining dipole mode and overall the longitudinal and transverse spectra are very well damped. This design is well below the threshold impedance for longitudinal instabilities even in the pre-damping ring, as shown in figure 79. Figure 80 shows the transverse impedance with the thresholds. The impedance is quite low but a modest feedback system would still be required. This design could be fabricated from a spherical center section with integral ports that could be lathe turned (except for the cooling channels) and two lids containing the HOM ports that could be formed by the EDM process as described before.

Further reduction in the impedance might be achieved by enlarging the HOM ports (although eventually the persistent wakefield at the waveguide cut-off frequency becomes the limit), or perhaps by using three waveguides on each side. The low R/Q options discussed above, if required to minimize beam loading transients, might also lead to very low HOM impedances if appropriately damped. The beam-pipe damped superconducting single cell cavities also have very low HOM impedance.

These designs will be studied further as appropriate as the R&D phase progresses and the ring parameters evolve.

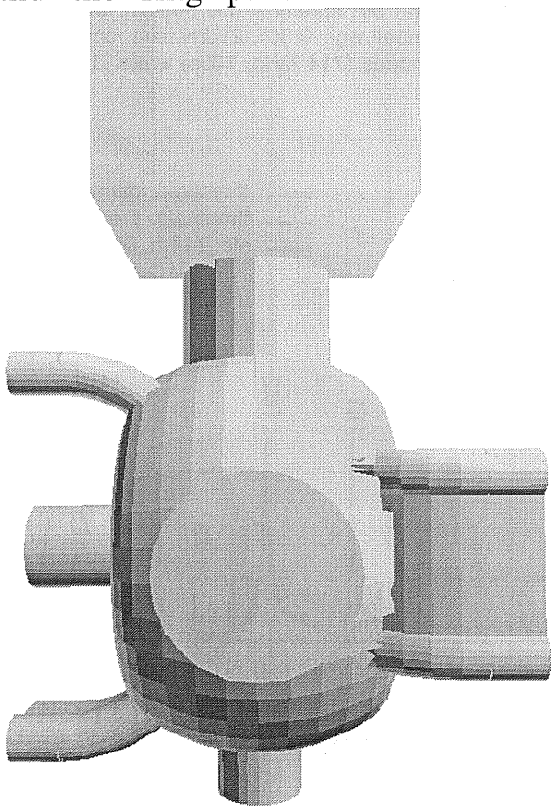

Figure 78. MAFIA model of four-waveguide design.

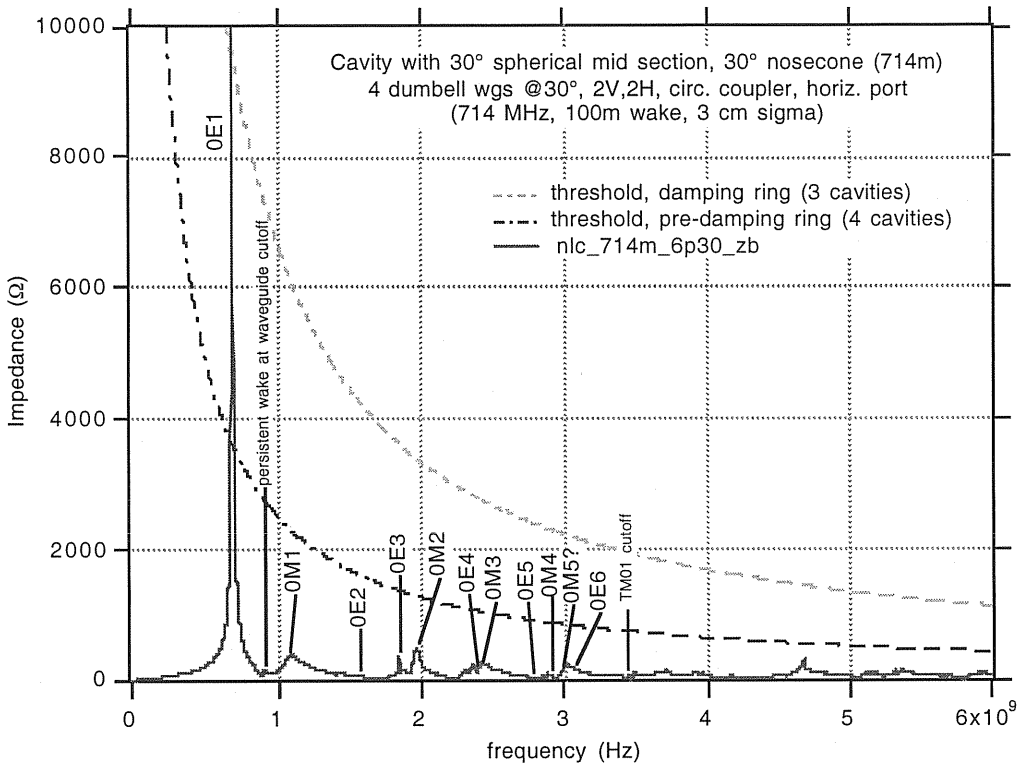

Figure 79. Longitudinal impedance of four-waveguide cavity.

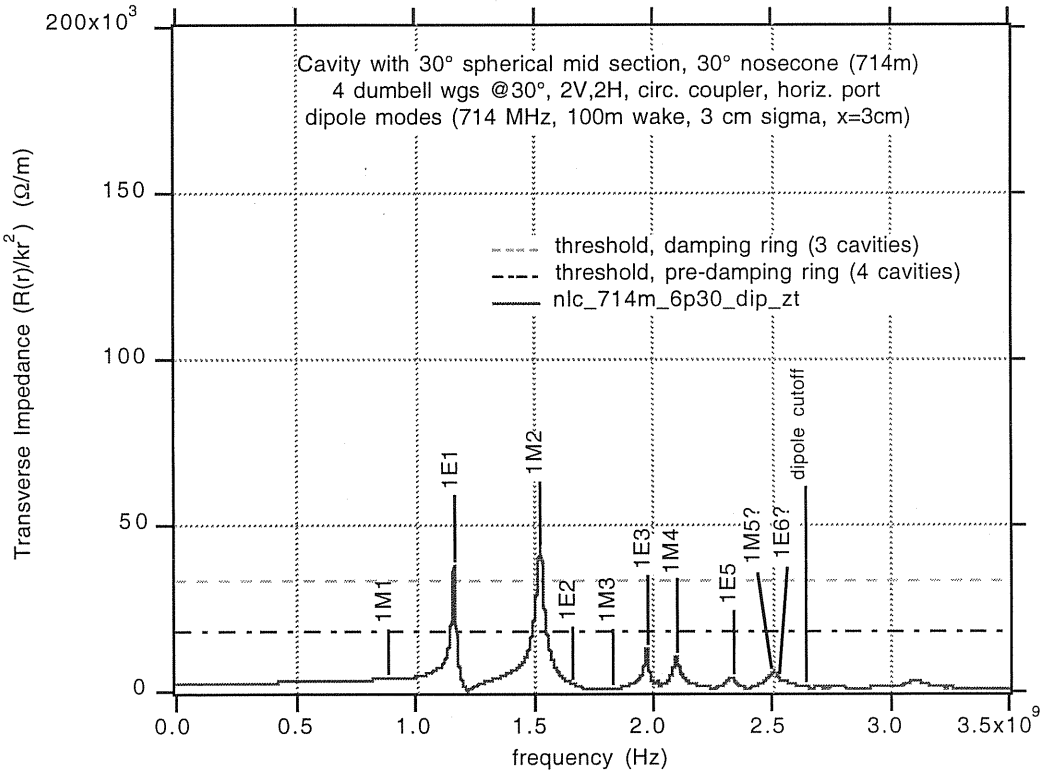

Figure 80. transverse impedance of four-waveguide cavity.

8. Cost estimating

A cost analysis is underway for an assembly based on the method described in section 3. Costs will be broken down by categories for raw materials and other procurements, labor for in-house operations, outsourced operations, and non recurring engineering costs such as process development, fixturing etc. Appendix A contains tables of the major components and operations in each of these categories. (Note that the estimates in these tables do not include contingency, this will be added later in proportion to the uncertainty or risk of individual items). Many of the items can be estimated reliably based upon previous experience with the PEP-II and ALS harmonic cavities. Others are straightforward procurements of standard or nearly standard components. Some processes such as the EDM of the port blends have already been prototyped. Others are based on known processes but require further testing, such as the plating, which may require tests to determine the optimum placement of electrodes. Wherever possible straightforward operations will be outsourced to reduce costs. Operations with high technical risk may be kept in house, or developed in house for the first cavity and then transferred outside for production models. Where budgetary estimates from outside vendors are available they will be used in the costing, otherwise estimates will be scaled from previous similar procurements or, for in house work, using time and materials and standard project-wide labor rates. Estimates will be made assuming a count of ten cavities, three for each damping ring and four for the positron pre-damping ring. Appropriate overage of materials will be included to anticipate possible production losses but no completed spares will be included in the estimates.

9. Conclusions

This study has begun the process of developing an RF cavity and ancillary equipment for the NLC Damping rings. The RF cavity is based on the successful PEP-II design but all aspects have been reexamined in an attempt to simplify the fabrication while maintaining or improving the HOM damping performance and lowering the operating stresses. All of these goals have been accomplished, the design has many fewer parts and operations, the HOM impedances are reduced compared to a scaled version of the PEP-II cavity and the thermal stresses around the HOM ports are significantly reduced by careful shaping of the waveguide cross section and the blend into the cavity walls. New computational tools

such as the broadband time domain analysis in MAFIA and the high frequency electromagnetic analysis in ANSYS have been very useful in this process.

Conceptual designs for the ancillary equipment including the RF window, HOM loads and tuners have been presented. The window and HOM loads are based closely on scaled versions of the PEP-II components, while the tuners follow the simpler ALS harmonic cavity approach. The mechanical design of these components will continue during the next fiscal year with the same goals of simplicity, reliability and lower cost in mind.

Other cavity options have been considered which may have advantages in terms of lowering the transient response of the RF system to gaps in the beam, or further reducing the residual HOM impedances. These options will be studied further as the overall damping ring requirements evolve.

The process of detailed cost estimating has begun and a preliminary estimate of tasks, resources, procurements and non recurring development effort has been compiled. This will be consolidated as the component and system engineering continues and the designs converge towards production.

10. References

[1] "Commissioning Results Of The KEKB And PEP-II B-Factories", J.T. Seeman, Proceedings of the 1999 Particle Accelerator Conference, New York, 1999.

[2] "DAΦNE Operating Experience", S. Guiducci, Proceedings of the 1999 Particle Accelerator Conference, New York, 1999.

[3] "A Third-Harmonic RF Cavity for the Advanced Light Source", R.A. Rimmer, EPAC98, Stockholm, Sweden.

[4] "Design Considerations for a Second Generation HOM-Damped RF Cavity", R. A. Rimmer, Proceedings of the 1999 Particle Accelerator Conference, New York, 1999.

[5] PEP-II RF cavity revisited, R.A. Rimmer et.al., CBP Tech Note 197, LCC-0032, Nov. 1999.

[6] "Zeroth-Order Design Report for the Next Linear Collider", LBNL-PUB-5424, SLAC report 474, UCRL-ID-124161.

[7] "Users Guide for ABCI Version 8.8 (Azimuthal Beam Cavity Interaction)", Y.H. Chin, Feb. 1994, LBL-35258, UC-414.

[8] "Higher Order Mode Damping in a Pillbox Cavity", F. Voelker et. al., Proc. 1991 PAC, San Francisco, pp 687-9.

[9] "RF system research and development for the PEP-II B factory", R.A. Rimmer, NIM B 99 (1995) 717-720.

[10] "Cavity RF Mode Analysis Using a Boundary-Integral Method", M.S. De Jong, F.P. Adams, Proc, 1993 PAC, Washington DC, pp 835-7.

[11] Ansys, Inc., 275 Technology Drive, Canonsburg, PA 15317 Tel: 724-746-3304, Fax: 724-514-9494, (http://www.ansys.com).

[12] HF 119, High Frequency Electromagnetic Tetrahedra, ANSYS Elements Manual Section 10.2

[13] "Omega3p: A Parallel Eigensolver of Modeling Large, Complex Cavities", Proc. ICAP 98, Monterey, CA.

[14] Parametric Technology Corporation, 128 Technology Drive, Waltham, MA 02453. Phone: 781-398-5000, Fax: 781-398-6000 (http://www.ptc.com).

[15] "High-Power RF Cavity R&D for the PEP-II B-Factory", R. Rimmer et. al., Proc. EPAC 94, London.

[16] "Low temperature mechanical properties of copper and selected copper alloys; a compilation from the literature", Richard P. Reed and Ritchie P. Mikesell, [Washington] U.S. Dept. of Commerce, National Bureau of Standards; for sale by the Supt. of Docs., U.S. Govt. Print. Off., 1967, p43.

[17] "PEP-II B-Factory Prototype Higher Order Mode Load Design", R. Pendleton et. al., Proc. PAC 95, Dallas, TX.

[18] "High-Power RF Window and Coupler Development for the PEP-II B Factory", M. Neubauer et. al., Proc. PAC 95, Dallas, TX, SLAC PUB 95-6894, LBNL-37250.

[19] "High-Power RF Window Design for the PEP-II B Factory", M. Neubauer et. al, Proc EPAC 94, SLAC PUB-6553, LBL-35920.

[20] "HOM-Free Cavities", R. Boni, proc. EPAC98, Stockholm, Sweden.

[21] "RF Superconductivity for Accelerators", Hasan Padamsee, Jens Knobloch, Tom Hayes, Wiley series in beam physics and accelerator technology, ISBN 0-471-15432-6, 1998, p282.

[22] "Handbook of Accelerator Physics and Engineering", [edited by] Alexander Chao and Maury Tigner, World Scientific, ISBN 9180238584, 1998, sec. 7.3.8, p526.

[23] "Review of Experience With HOM Damped Cavities", H. Padamsee, proc. EPAC98, Stockholm, Sweden.

[24] "A Prototype Module of a Superconducting Damped Cavity for KEKB", T.Furuya, et. al., Proc. EPAC 96, Barcelona, Spain.

Appendix A. Estimates of materials, fabrication, procurements and engineering

The following seven tables represent a preliminary estimate of the major components, operations and processes, based on the fabrication method outlined in section 3 and a total of 10 cavities. Production costs will vary depending upon the degree of difficulty of the operation and whether it can be outsourced or should be performed in house. The estimates therefore represent a first attempt to list all of the parts and processes involved and to quantify the hours required for each. The estimate is divided into separate sections for materials and procurements, lid and body machining (the two major components), integration and assembly, outsourced operations, and non-recurring costs. Note that these estimates do not include contingency; this will be evaluated later in proportion to the uncertainty or risk of individual items.

Table A8 shows a summary of approximate costs of PEP-II RF station equipment including cavity ancillary items such as windows, HOM loads and tuners. This equipment was constructed or purchased between 1994 and 1998 and costs are in "then-year" dollars. These costs, suitably adjusted, may be used as approximate guides for the NLC cavity ancillaries and RF station equipment until improved estimates are developed.

Table A1. Summary of preliminary estimates

	Estimate is based on 10 assembled cavities,	$	Hr.
	material is for 12 possible starts		
Table			
A2	**Materials, Procurement**	$193,252	
A3	**Lid Machining**	TBD	2048
A4	**Body Machining**	TBD	1944
A5	**Integration, Assembly**	TBD	1078
A6	**Outsourcing**	TBD	4615
A7	**NRE**	TBD	3912
	Total		13597

Table A2. Raw materials and procurements.

Raw Materials	$ Ea.	Req.	$ Total	Notes
lid forging	$3,086	12	$37,032	
body forging	$3,554	12	$42,648	
cold test model forgings, lid and body			$6,640	
blank off flange materials, 4 sets			$300	100lb @ $3
cavity support fixture materials			$900	300 lb @ $3
tooling and fixturing			$1,500	500 lb @ $3
tool cut path and prototyping materials			$1,500	500 lb @ $3
Procurement				
knife edge flanges w/brazed copper inserts				
10"	$600	4(12)=48	$28,800	
6"	$360	4(12)=48	$17,280	
4.5"	$300	4(12)=48	$14,400	
ofhc gaskets - 10"	$6	100	$600	
ofhc gaskets - 6"	$4	100	$350	
ofhc gaskets - 4.5"	$3	100	$250	
knife edge flange bolting materials, all flanges			$2,100	
spherical bearings	$19	48	$912	
316L stainless steel water fittings	$20	192	$3,840	
support fixture bolting			$300	
o-rings for blankoff flanges			$750	150 @ $5
knife edge blank off flanges, 2 transport sets			$4,660	rotatable & blank
viewport window		3(12)=36		
Consumables				
3/8" ball end mills - cooling grooves	$45	6(12)=72	$3,250	
2"x 6" diesinker-hom roughing, lid&body finish	$1,500	6	$9,000	2" dia, 3" loc, 1.5" shank, 10"oa
edm electrode material			$4,000	1 lot matl / 3 cavities, 4 lots @ $1000
edm wire, roll	$170	2(36)=72	$12,240	8hr 1st, 22.5hr 2nd=30.5hr, 16hr/roll

Total	$193,252

Table A3. Lid fabrication.

Lid - Rough Machining	Hr. Ea.	Hr. Total	Notes
face & turn forging to size	1.95		
turn material on outside of hom	5.2		
bore material on inside of hom	1.95		
mill between hom ports	7.8		
bore inside surfaces of lid	0.65		
create fiducial datums	2.6		
drill and bore beam pipe hole	1.3		
drill edm wire access holes	3.9		
set up, installation and handling	10.4		8 ops @ 1 hr
cmm inspection	7.8	43.6	
Lid - Finish Machining			
turn outer surfaces and beam pipe	2.6		
mill outer surfaces - 5 ax, 3d mod	5.2		
cut body surface water grooves- 5ax, 3d mod	5.2		
cut hom surface water grooves- 5ax, 3d mod	5.2		
bore beam pipe hole	1.3		
turn inside surfaces - 3d model	3.9		
wire edm hom openings - 3d model	78		actual cut time 120 hr, 50% charge
plunge edm hom radii - 3d model			see outsourcing
drill & tap lift/support mounting bosses	5.2		
step cut hom extensions for flange fit - 3d model	10.4		
machine lid mating face and groove, eb weld prep	5.2		
remove fiducial datums	2.6		
set up, installation and handling	28.6		11 ops @ 2 hr
cmm inspection - 3d model comparison	7.8	161.2	

Total	204.8	one unit

Table A4. Body fabrication.

Body - Rough Machining	Hr. Ea.	Total	
face & turn forging to size	1.95		
turn o.d. for port extensions	5.2		
turn face and beampipe weld prep	2.6		
create fiducial datums	2.6		
bore i.d. and beampipe hole	3.9		
mill between port extensions	7.8		
trepan around port extensions - 3d model	10.4		
drill and bore port extension holes	7.8		
fab beam pipe extension w/weld prep - body end only	5.2		
set up, installation and handling	11.7		9 ops @ 1 hr
cmm inspection	7.8	67	
Body - finish Machining			
turn outer surfaces and beampipe weld prep	5.2		
machine outer surfaces 5 axis, 3d model	20.8		
cut water passage grooves, 5 axis 3d model	20.8		
water fitting - location spotface, 5 axis 3d model	7.8		
bore extension port holes/slots	10.4		
step cut port extensions for flange fit - 3d model	10.4		
drill & tap support mounting bosses	5.2		
bore i.d. and beampipe hole - 3d model	7.8		
body mating face and groove, eb weld prep	5.2		
remove fiducial datums	2.6		
plunge edm all internal radii/slots			see outsourcing
set up, installation and handling	26		10 ops 2 hr
cmm inspection - 3d model comparison	5.2	127.4	

Total	194.4	one unit

Table A5. Integration and assembly.

	Hr. Ea.	Total	Notes
Blank Off Flanges			
fabricate flanges - vac check blankoff	1.56	37.4	2 sets of 12
fabricate flanges - plating blankoff	1.56	37.4	2 sets of 12
clean flanges, pack until use		20.8	
clean o-rings, pack until use		5.2	
Support Structure Fabrication			
fab support structure components		78	
modify spherical mounts as required	2.6	31.2	
fab attachment/lift point inserts	0.65	62.4	8/cavity = 96
clean inserts and package		5.2	
Knife Edge Flange Machining			
post-braze leak check and flatness inspection	0.65	85.8	11/cavity = 132
machine port ext. profile in brazed insert	0.975	107.3	10 sets = 110
clean flanges, pack until use		20.8	11/cavity = 132
Water Fitting Prep and Placement			
modify fittings to fit body/lid locations	0.39	74.9	16/cavity = 192
clean fitings - pre plating, pack until use		20.8	
Body / Lid Cleaning, Pre-Weld			
pre-weld polishing, blending as required	2.6	26	2hr/cavity to blend, polish,
assign flanges to port ext. locations, doc	2.6	26	
pre-weld cleaning	1.3	13	
package and crate for shipment	0.65	6.5	
Tuning cycle			
measure and cut nosecone to frequency	10	120	3 iter. cav1, 1 cut cav 2-10
Electron Beam Welding			see outsourcing
Post - Weld Processes			
mount weldment in temp support fixture	0.65	6.5	
inspection	1.3	13	
flange inspection and blankoff	2.6	26	
leak check	1.3	13	
remove blankoff	0.65	6.5	
remove support, package	1.3	13	
Pre - Electroplating			
install attachment point inserts	1.3	13	
install water fittings	1.3	13	
install blankoff flanges for electroplating	2.6	26	
package and crate for shipment	0.65	6.5	to electroplate vendor
Electroplating			see outsourcing
Post - Plating Processes			
remove electroplating blankoffs	1.3	13	
mount weldment in temp support fixture	0.65	6.5	
flow test each channel, orifice,document	5.2	52	
blow down water circuits, cap off	2.6	26	
remove temp support fixture	1.3	13	
clean, blankoff, package	5.2	52	
	Total	1077.7	

Table A6. Outsourced operations.

	Hr. ea.	hrs tot	
Plunge EDM Process			
radius - lid hom ports	26	780	20 hr, 30 ports
radius - body internal ports	5.2	312	4 hr, 60 ports
set up and handling, tool change	3.9	351	3 hr , 90 ports
fixturing and tooling			
Electron Beam Welding			
body - lid setup and assy	10.4	104	10 joints
body - lid weld, outside	10.4	104	10 joints
body - lid weld setup, inside	10.4	104	10 joints
blankoff and leak check lid/body weld	2.6	26	10 joints
body - lid weld, inside	10.4	104	10 joints
extension port setup and assy	5.2	572	11 joints / cavity, 110 joints
extension port weld	5.2	572	11 joints / cavity, 110 joints
beam pipe weld - body side, setup and assy	5.2	52	10 joints
beam pipe weld	5.2	52	10 joints
mount on support structure	0.65	6.5	10 bodies
blankoff /leak check all port extension joints	5.2	52	10 bodies
SLAC inspection, q/a	10.4	104	10 bodies
remove support structure	0.65	6.5	
package and crate for shipment	1.3	13	to LBL
Electroplating			
electroplating, all	130	1300	100hr ea. @ partial rate?

Total		4615

Table A7. Non-recurring costs, major items.

NRE	Est. Hr.	comments
prototyping		
cold test model - lid	260	
cold test model - body	260	
cold test support structure	52	
machine tool programing	260	
milling program - proof cutter path		
lid - hom geometry	31.2	
lid cut path - water grooves	31.2	
body - port extension geometry	31.2	
body - surface cut path	31.2	
body - water grooves	31.2	
cutter shaping, resharpening	104	
fab fixturing for eb welding		
body - lid fixtures	130	
port extension flange fixtures	130	
inter-vendor crating, packaging, shipping	0	
crating and packing materials	104	
r/t shipping to edm vendor	19.5	
r/t shipping to electroplater	104	
r/t shipping to SLAC	19.5	
100% inspection of all prototypes	130	
lid-tooling and fixturing	104	
body-tooling and fixturing	104	
lifting fixtures		
fabrication	52	
certification	20.8	
materials testing	0	
ndt - ultrasonic insp of forgings	156	24 forgings
prolongation coupons - lid	124.8	4 hr/coupon
prolongation coupons - body	124.8	4 hr/coupon
coupon testing	52	24 coupons
in-process documentation all prototypes	52	
supervision	123.5	2.5% of 3,806 fab hrs
vendor qualification, travel	104	
q/a inspection, documentation	130	10 hr/part
electroplating development		
fixturing	104	
prototyping	130	
plating analysis	52	
cold test model - plating	520	.001/hr,.400 thick
eb welding development		
proof weld path	124.8	16 hr/each joint size, 6 joints
fixturing devlopment	52	
weld prototyping	52	
weld analysis		
Total	3911.7	

Table A8. Approximate cost of PEP-II RF station equipment . (Note: these items were constructed or purchased between 1994 and 1998)

Item	approx. cost per item (then year k$)
Klystron (Phillips, 1.2 MW)	335
Cavity	150
HOM loads (3 per cavity)	16
Coupler box (1 per cavity)	26
500 kW Window (1 per cavity)	24
Fixed tuner (1 per cavity)	3
Variable tuner (1 per cavity)	9
Raft (1 per cavity)	14
Circulator (AFT)	155
Waveguide network (per 4-cavity station)	68
Low-level RF (per 4-cavity station)	85
HV power supply	375
Cooling system (per 4-cavity station)	40
Cables (per 4-cavity station)	35
Misc., installation etc. (per 4-cavity station)	60